

**Large area thermal neutron detectors for  
security applications**

**Edward James Marsden**

**Thesis submitted for the degree of Doctor of Philosophy  
University of Sheffield  
Department of Physics**

**2012**

## **IMAGING SERVICES NORTH**

Boston Spa, Wetherby

West Yorkshire, LS23 7BQ

[www.bl.uk](http://www.bl.uk)

**PAGE NUMBERS VERY  
FEINT/DIFFICULT TO READ**

**BEST COPY AVAILABLE.**

**VARIABLE PRINT QUALITY**

54

# Abstract

This report details the research and development of a novel class of large area thermal neutron detector, developed specifically for the application of cargo screening. Based broadly on a laminar scintillation device, developed by Barton et al, using ZnS and Li<sup>6</sup>F, the new detector achieves a comparable level of performance to standard <sup>3</sup>He tubes, but only employs readily available components and none isotopically enriched chemicals, thereby offering a low cost solution to the problem caused by restrictions in the supply of <sup>3</sup>He.

**Supervisor:** Prof. N.J.C. Spooner

# Authors contribution to the project

Although the focus of this project is very much a current concern, the background to the work stretches back over twenty or more years, both in terms of my contribution and that of the main co-contributor Dr. John McMillan. Working as an electronic research engineer at Tata Steel (formally Corus and British Steel), I have long been involved with the development of radiation detectors, initially for process control and more recently for the detection of rogue sources both in scrap and elsewhere. Much of the background work, justification, specification as well as the initial seed of the idea for this project (low cost thermal neutron detection) come from that time. The likely direction in which the development was to go (laminar scintillation detector) came from the earlier work carried out by Dr. McMillan and Dr. John Barton.

Developing a bench mark for the new detector, based on characterisation of the refurbished McMillan detector and  $^3\text{He}$  based proportional counter was my first main contribution to the project. I was also wholly responsible for Monte Carlo modelling, initially to verify and optimise performance of these existing detectors, and subsequently to aid the various phases in the design of the new detector.

Selection, acquisition, and evaluation of the scintillating, capture and binder compounds was carried out in close cooperation with John McMillan, although all the results presented here are my own.

All aspects of the design, development, manufacture and testing of the new rod based detector were undertaken by me, as was the development of the stand alone electronic signal processing module, along with the firmware and software to drive it. Development and optimisation of neutron discrimination algorithms for this detector, while initially based on work by Barton et al, was also realised by me, as was all laboratory and field testing of detectors reported here (unless otherwise stated).

# Acknowledgments

My first thanks must go to my employer Tata Steel RD&T, a rare organisation that still holds value in research, and the development of its staff, and specifically to Clive Lester, Rene Duursma and Andy Howe who not only provided funding for the six years of this project but gave advice, support and encouragement throughout.

My supervisor Neil Spooner I thank firstly for having the nerve to offer a steel works engineer a chance to join his research group, but also for valuable guidance where it was sought, space where it was appropriate and reassurance where it was needed.

John McMillan, without whom this project would never have happened, deserves unreserved credit, for a never ending stream of fresh ideas, a bottomless font of knowledge, a constantly challenging analytical eye, and above all his infectious energy and positive good humour throughout.

The British Home Office deserve thanks not only as sponsors of the project, but also as enthusiastic advocates for the work. In particular I'd like to thank Dick Lacey and John Gossling for recognising the value of this development and helping to give it a firm direction and purpose.

On a personal level I would like to thank Andrew Cole and Paul Thompson for good company, conversation and technical input, along with all members of the Particle Physics and Astronomy Group that I've come into contact with at Sheffield, a more friendly, welcoming environment in which to work would be hard to find, and this of course comes down to the people within it.

Last but far from least, are the love and thanks owed to my wife Jacqueline and boys Ben and Henry; for patience, encouragement and a healthy dose of reality after long days in the laboratory.

# Contents

<b>1. Background - Neutron detection for security applications</b> .....	<b>1</b>
1.1 Introduction .....	1
1.2 Radiation detection in scrap metal .....	2
1.3 Radiation detection for border security .....	4
1.4 Corus Redeem .....	8
1.5 Passive neutron detection .....	9
1.6 Active neutron interrogation .....	12
1.7 Requirements for large area thermal neutron detectors .....	15
1.8 Useful neutron interactions .....	18
1.9 Commercial implications and the $^3\text{He}$ problem .....	22
1.10 Target specification .....	24
1.11 Conclusions .....	25
<b>2. Benchmark thermal neutron detectors</b> .....	<b>26</b>
2.1 Introduction .....	26
2.2 Background to the design of the PNL $^6\text{LiF}$ detectors .....	26
2.3 Wavelength shifting light guides .....	31
2.4 Photomultiplier tube selection .....	34
2.5 Signal processing .....	36
2.6 Testing and evaluation of PNL detector .....	39
2.7 $^3\text{He}$ proportional counter - benchmark detector .....	42
2.8 Conclusions .....	46
<b>3. Monte Carlo analysis</b> .....	<b>47</b>
3.1 Introduction .....	47
3.2 MCNP .....	47
3.3 $^3\text{He}$ detector benchmarking .....	49
3.4 $^3\text{He}$ detector optimization .....	51

3.5 $^6\text{LiF}$ / $\text{ZnS}$ detector .....	54
3.6 BN detector .....	57
3.7 Sample testing assembly .....	59
3.8 Conclusions .....	60
<b>4. Material selection for <math>^{10}\text{B}</math> based detectors .....</b>	<b>61</b>
4.1 Introduction .....	61
4.2 Selection of neutron capture and scintillating compounds.....	62
4.3 Boron as a neutron capture agent .....	65
4.4 Performance of scintillating compounds.....	73
4.5 Performance of capture compounds.....	88
4.6 Wavelength shifting light guides.....	90
4.7 Light guide testing.....	93
4.8 Detector geometry .....	96
4.9 Conclusions .....	100
<b>5. Manufacture of BN based detectors.....</b>	<b>101</b>
5.1 Introduction .....	101
5.2 Selection of binders / solvents.....	101
5.3 Coating techniques .....	104
5.4 Design of the two new BN/ZnS based detectors.....	105
5.5 Optical coupling of light guides .....	108
5.6 Rod detector mechanical assembly .....	111
5.7 Conclusions .....	115
<b>6. Pulse discrimination techniques and implementation .....</b>	<b>116</b>
6.1 Introduction .....	116
6.2 Source of noise within the BN:ZnS detector.....	117
6.3 Neutron gamma discrimination techniques.....	124
6.4 Photon counting discrimination .....	127
6.5 Dynamic pulse counting discrimination circuit .....	128
6.6 Analysis software .....	135
6.7 Setup and optimization of photon counting discriminator .....	136

6.8 Dynamic photon counting algorithms .....	140
6.7 Conclusions .....	142
<b>7. Testing and evaluation of BN detectors.....</b>	<b>143</b>
7.1 Introduction .....	144
7.2 BN detector optimization .....	147
7.3 Laboratory evaluation of BN, <sup>6</sup> LiF and <sup>3</sup> He detectors.....	148
7.4 Field testing .....	149
7.5 Environmental testing .....	151
7.6 Conclusions .....	152
<b>8. Conclusions and Recommendations.....</b>	<b>153</b>

# List of figures

1.1: Orphaned $^{241}\text{Am}$ Source found on a British Steel site. ....	3
1.2: Corus Scrap Radiation System(Rotherham) .....	3
1.3: a,(Left) ASP systems undergoing test in Nevada USA, b,(Right) <i>Inside an ASP panel (<math>^3\text{He}</math> based detector on left, 4 NaI detectors on right).....</i>	7
1.4: Decay of $^{87}\text{Br}$ following neutron capture on $^{235}\text{Eu}$ [13] .....	13
1.5: Photograph of the CSIRO NITA cement analyzer[14] .....	14
1.6: Neutron capture cross section of the most effective detector isotopes[21] .....	20
1.7: Fission neutron spectra for $^{240}\text{Pu}$ (blue line) and $^{252}\text{Cf}$ (red line), approximated <i>by Watt distributions calculations [1.7] .....</i>	21
2.1: Cross section of PNL $^6\text{LiF ZnS}$ detector .....	27
2.2: Photograph of PNL $^6\text{LiF ZnS}$ detector .....	27
2.3: Simplified schematic of the PNL detector assembly .....	28
2.4: BBQ doped wavelength shifting light guide under UV illumination.....	32
2.5: BBQ absorption peak (dashed line) / emission peaks (squares[42], triangles[43]), <i>with normalised photomultiplier bialkali response (crosses).....</i>	32
2.6: Attenuation of BBQ Light Guide, measurements made with 450 nm pulsed LED; <i>the top line shows performance improvement with a reflecting coating applied     to the edge furthest from the PMT .....</i>	33
2.7: EMI 9791 Photomultiplier Testing – Single photon dark count <i>(note variability of plateaux count rate) .....</i>	35
2.8: EMI 9791 Photomultiplier Testing – Single photon count rate pulsed light source <i>(note variable role off voltage but consistent plateaux level).....</i>	35
2.9: Neutron signal pulse train produced by ZnS(Ag) on 400 mm light guide with $^{241}\text{Am}$ alpha source .....	36
2.10: (left)Flow chart of the photon counting pulse discrimination technique, (right) Signal path: Input – differentiated – digitized.....	37
2.11: Modified electronic circuit for pulse discrimination .....	38
2.12: Laboratory testing of a PNL detector (solid line) and $^3\text{He}$ detector (dashed) <i>with a <math>^{252}\text{Cf}</math> reference source, for bulk count rate with distance. ....</i>	40
2.13: Laboratory testing of a single $^6\text{LiF:ZnS}$ detector(solid line)and $^3\text{He}$ detector	

(dashed line) with a $^{252}\text{Cf}$ reference source ( $23 \text{ kBq} = 2,600 \text{ n.s}^{-1}$ ), for linearity of performance. Source 10 cm from the face of the detector. ....	40
2.14: $^3\text{He}$ Proportional Counters in a range of sizes .....	41
2.15: $^3\text{He}$ based detector used for bench mark testing.....	43
2.16: $^3\text{He}$ Pulse Height Plateau(50 mm tube at 1250 V bias) .....	45
3.1: MCNP / Sabrina output (only neutrons interacting with the ground are shown).....	50
3.2 – 3.5: MCNP $\text{He}^3$ detector optimisation; intrinsic efficiency calculated for key detector parameters .....	52
3.6: MCNP / Sabrina output $\text{He}^3$ detector (cross section extracted for analysis) .....	53
3.7: MCNP / Sabrina output $^6\text{LiF/ZnS}$ detector (cross sectioned removed for analysis) ...	54
3.8 a,b: MCNP $^6\text{LiF}$ detector optimisation; intrinsic efficiency calculated for key detector parameters (a-moderator thickness, b-LiF thickness) .....	55
3.9: MCNP $^6\text{LiF}$ detector optimisation; intrinsic efficiency contribution from individual layers of capture / scintillator.....	55
3.10: MCNP $^6\text{LiF}$ detector optimisation; efficiency variation with width for a constant flux neutron field. ....	56
3.11: Effect of boron capture layer thickness on intrinsic efficiency.....	58
3.12: Cutaway ray traces of rod based detector models .....	58
3.13: Cutaway ray traces of small light guide model.....	60
4.1: Hexagonal $\alpha$ -BN structure .....	67
4.2: Cubic $\beta$ –BN structure .....	67
4.3: Cubic BN (left), Hexagonal BN (Right)[64] .....	68
4.4 a,b: Grain size consideration in BN; a – left illustrates implications of capture particle size, b – right need for sufficient scintillating material.....	69
4.5: SRIM calculations for $^3\text{H}$ , $\alpha$ and Li ions in BN LiF and ZNS .....	72
4.6: Energy deposition of charged particles (Bragg curve) for single alpha particle in air [69] .....	72
4.7: Excitation(dotted) / emission spectrum for ZnS:Ag [Phosphor Technologies' grade GL47] .....	77
4.8: Excitation(dotted) / emission spectrum for ZnO:Ga [Phosphor Technologies' grade GK31] .....	79
4.9: Excitation / emission spectrum YAP .....	81
4.10: Schematic of test assembly housing wavelength shifting light guide and photomultiplier.....	85

4.11: <i>Photograph of light guide test assembly</i> .....	86
4.12 to 4.16: <i>Scintillation decay for ZnS:Ag, PTP, YSO, ZNO:Eu, YAP(pulse height in Volts plotted against time in ns). Averaged traces taken through BBQ wavelength shifting light guide</i> .....	87
4.17: <i>Attenuation of blue light by hexagonal BN/ZnS</i> .....	88
4.18: <i>Small sample testing; MCNP predicted count rate(dashed), measure rate for cubic (bottom line) and hexagonal (top line)BN/ZnS</i> .....	89
4.19: <i>(above)Commercial fluorescent acrylic</i> .....	91
4.20: <i>(right)Dip coating apparatus for 1meter rods</i> .....	91
4.21: <i>(below)Dip coated acrylic light guides bent to shape after coating</i> .....	91
4.22: <i>Performance small coated light guide(solid line – 100 mm from PMT, dashed 250 mm from PMT)</i> .....	93
4.23: <i>Performance of Plexiglas GS2025 light guide(solid line – no reflector, dashed line- foil reflector)</i> .....	93
4.24: <i>Attenuation of light in solid light guides (tested with 450 nm LED)</i> .....	94
4.25: <i>Attenuation of light in coated light guides (tested with 450 nm LED)</i> .....	95
4.26: <i>Attenuation of light in long coated light guides (tested with 450 nm LED)</i> .....	95
4.27: <i>Attenuation of light in shaped coated light guides (10mm diameter)</i> .....	96
4.28: <i>Incoming light (blue) captured by fluorescence (green) and total internal reflection, in a planer wavelength shifting light guide.</i> .....	97
4.29: <i>Plain fish tail (left), and twisted fish tail light guide, for coupling large rectangular light guide / scintillating plates to a photomultiplier</i> .....	98
4.30: <i>Light trapped by a cylindrical wavelength shifting light guide.</i> .....	99
5.1: <i>Vacuum bed and Doctor blade assembly, with coated sample institute</i> .....	104
5.2: <i>BN “paint” - coating thickness measured against Doctor blade setting (dashed line measurements taken with ultrasonic probe, solid line micrometer measurement)</i> .....	105
5.3: <i>Rod based detector during assembly (all 24 wavelength shifting light guides partially exposed)</i> .....	106
5.4: <i>Rod based detector during assembly (on the left the ends of the light guides can be seen illuminated by ambient light, on the right foil backed BN:ZnS tubes have been inserted over several of the rods)</i> .....	107
5.5: <i>Optical coupling tests between light guide and photomultiplier</i> .....	108
5.6: <i>Size miss-match between laminar light guides and photomultiplier</i> .....	110

5.7: <i>Bent coated light guide rods.</i> .....	110
5.8: <i>Relative position of the light guides, in the moderator matrix (black), and</i> .....	111
<i>at the photocathode (red), arranged to required only 4 different formers.</i>	
5.9: <i>Schematic design of the front end of the rod based BN/ZnS detector (cut-away)</i> .....	112
5.10: <i>HDPE slabs machined for the rod based detector</i> .....	113
5.11: <i>HDPE slabs stacked together, and light guide coupling plate</i> .....	113
5.12: <i>Photomultiplier housing, end plate (with light guide coupling dish),</i>	
<i>75mm photomultiplier with voltage divider circuit attached</i> .....	114
5.13: <i>End view of completed rod detector assembly</i> .....	114
6.1: <i>Alpha (dashed) and gamma (solid) induced pulses in ZnS(Ag), measured on a</i>	
<i>thin film scintillation detector close coupled to a photomultiplier. Gamma trace</i>	
<i>scaled up by a factor of 10</i> .....	120
6.2: <i>Background pulse height distributions for four photomultipliers at 20°C. The</i>	
<i>lower trace has a quartz window and is free from radioactive contaminant but</i>	
<i>shows a well resolved cosmic ray peak at 80 photoelectrons equivalent [118]</i> .....	122
6.3: <i>The time dependence of scintillation pulses in stilbene when excited by</i>	
<i>radiations of different types [136]</i> .....	124
6.4: <i>Signal pulse train produced by ZnS(Ag) on 400 mm light guide with <sup>241</sup>Am</i>	
<i>α source</i> .....	125
6.5: <i>Neutron signal pulse train produced by large BN:ZnS(Ag) detector</i>	
<i>irradiated by a <sup>252</sup>Cf reference source</i> .....	126
6.6: <i>Simplified schematic, and neutron signal pulse train as found in LiF:ZnS detector</i> ...	127
6.7: <i>Analogue signal block diagram for the new discriminator circuit</i> .....	129
6.8: <i>Analogue / digital circuit diagram for discriminator development</i> .....	130
6.9: <i>Photon counting logic - flow chart</i> .....	131
6.10: <i>PSPICE output trace for typical neutron signal; input signal(pink), amplified</i>	
<i>(light blue), differentiated (black), integrated pulse count (yellow)</i> .....	132
6.11: <i>Prototype discriminator circuit board</i> .....	133
6.12: <i>Discriminator circuit; Microcontroller functions and interfaces</i> .....	134
6.13: <i>Main discriminator PCB; analogue circuit inside screening can on right</i>	
<i>(lid removed), microcontroller and digital circuitry centre, power</i>	
<i>supplies left, prototyping area bottom right</i> .....	134
6.14: <i>Discriminator electronic assembly</i> .....	135
6.15: <i>Neutron detector interface software – live screen dump.</i> .....	136

6.16: Photomultiplier bias selection for EMI 9821 tube fitted to rod detector; dark count (no scintillator present)– solid line, Foreground (scintillator + $^{252}\text{Cf}$ ) – dashed line .....	138
6.17: Rod based detector photon counting threshold optimisation; $^{252}\text{Cf}$ source .....	138
6.18: Rod based detector, photon counting optimisation $^{60}\text{Co}$ source; 10 count threshold (diamonds), 12 count threshold (squares), 14 count threshold (triangles) .....	139
6.19: Rod based detector, photon counting optimisation $^{252}\text{Cf}$ source; 10 count threshold (diamonds), 12 count threshold (squares), 14 count threshold (triangles) .....	139
6.20: Rod based detector, dead time optimisation $^{252}\text{Cf}$ source at 100 mm .....	140
6.21: Photomultiplier mounted discriminator module .....	142
7.1: BN Rod detector with simple photon counting discrimination; $^{252}\text{Cf}$ source (squares), $^{137}\text{Cs}$ (triangles), Background (diamonds) .....	145
7.2: BN Rod detector with photon counting discrimination + pulse height threshold; $^{252}\text{Cf}$ source (squares), $^{137}\text{Cs}$ (triangles), Background (diamonds) .....	145
7.3: BN Rod detector with combined dynamic photon counting discrimination; $^{252}\text{Cf}$ source (squares), $^{137}\text{Cs}$ (triangles), Background (diamonds) .....	146
7.4: BN Rod detector with dynamic photon counting discrimination (solid) and pulse height threshold (dashed), for $^{252}\text{Cf}$ source at 100 mm (background subtracted) .....	146
7.5: Detector neutron sensitivity $^{252}\text{Cf}$ source; $^3\text{He}$ (dashed), BN rod (triangles), $^6\text{LiF}$ (squares) .....	147
7.6: MCNP model of $^3\text{He}$ detector / $^{252}\text{Cf}$ source in laboratory environment, showing heavy scattering of neutrons in the floor walls and benches (thermalized neutrons – red) .....	148
7.7: Detector positional sensitivity $^{252}\text{Cf}$ source at 100 mm; $^3\text{He}$ (fine dashed), BN rod (dashed), $^6\text{LiF}$ (solid) .....	149

# List of tables

1.1 Incidents involving radioactive material entering the steel making process[2], * - found in a scrap container at Genoa port .....	2
1.2 Common industrial isotopes .....	4
1.3 The commonest materials which contribute to false triggering of portal systems [6]..	6
1.4: Medical sources triggering detection systems [7, 8] .....	7
1.5 Gamma sensitivity to SNM for large NaI portal detectors- Note while all naked sources have a reasonable detectable signal (above background), only the contaminated source maintains this with shielding present .....	10
1.6: Neutron flux from Fissile materials [10]. * "Weapons plutonium" is relatively pure; typically 94% <sup>239</sup> Pu with 6% <sup>240</sup> Pu, while dirty plutonium, from spent fuel, has higher proportions of the more radioactive isotopes <sup>238</sup> Pu and <sup>240</sup> Pu .....	11
1.7: Induced neutrons produce in fissile isotopes[15] .....	15
1.8: Comparative sensitivity of commercial neutron detectors * Figures enhanced due to multiple detectors around source .....	17
1.9: Properties of most important neutron interacting isotopes[21] .....	19
2.1: Properties of neutron sensitive, scintillating materials [21,22] .....	29
2.2: Laboratory testing of benchmark detectors, count rate (s <sup>-1</sup> ) averaged over 300 s .....	41
2.3: Sensitivity measurement (counts per s) for 1 m x 50 mm <sup>3</sup> He based detectors in field testing on open air test site (figures with source present have background subtracted) .....	44
3.1: Comparison of MCNP data with lab results <sup>252</sup> Cf source – 5,200 n.s <sup>-1</sup> .....	49
3.2: Comparison of MCNP data with results from Redeem test site <sup>252</sup> Cf source ~13700 neutrons per second .....	51
3.3: Relative efficiency of alternative detector geometries .....	59
4.1: Silver activation reactions[21] .....	64
4.2: Prompt neutron reactions emitting energetic charged particles .....	65
4.3: Physical properties of boron nitride[63, 64] .....	67
4.4: Properties of inorganic scintillators .....	77
4.5: Properties of commercial grade ZnS [85] .....	78

4.6: <i>Ratio of fast and slow scintillation components in anthracene [22]</i> .....	81
4.7: <i>Properties of common organic scintillators</i> .....	81
4.8: <i>Comparative performance of powdered scintillators under a radiation (measured using EMI98210 PMT at 1750V)</i> .....	84
4.9: <i>Performance of powdered scintillators coupled by wavelength shifting light guide when exposed to <sup>241</sup>Am a source</i> .....	86
5.1: <i>Properties of binder agents (data taken from manufacturer data sheets)</i> .....	102
5.2: <i>Optical coupling losses between light guide and photomultiplier</i> .....	109
6.1: <i>Gamma attenuation coefficients at 500 keV for ZnS. Data taken from NIST tables[116]</i> .....	119
6.2: <i>Key analogue components of the photon counting discriminator circuit</i> .....	130
6.3: <i>Key logic components to the photon counting discriminator circuit</i> .....	131
6.4: <i>Reference sources used for setup and evaluation</i> .....	137
6.5: <i>Optimum setup parameters for rod based BN:ZnS detector</i> .....	140
7.1: <i>Count rates for laboratory background, an adjacent 119 kBq <sup>60</sup>Co source and a 30 kBq <sup>252</sup>Cf source at 2m, with the source naked and moderated by 44 mm polypropylene</i> .....	147
7.2: <i>Initial test results from Nevada DNDO testing using 333 kBq <sup>137</sup>Cs source and a 65,000 n.s<sup>-1</sup> <sup>252</sup>Cf source at 4m distance, with sources and detector 1.5 m from the ground</i> .....	150

# **Chapter 1**

## **Background: Neutron detection for security applications**

### **1.1 Introduction**

Although for many years the hazards associated with the use of radioactive sources has been well known [1], until fairly recently little has been done to prevent either the inadvertent or intentional transport and distribution of highly radioactive, and potentially very harmful, materials. In the 1980s a number of high profile incidents, involving stray or orphaned radioactive sources, which in several cases resulted in fatalities, brought this problem to light; Table 1.1. As many of these incidents involved the accidental melting of sources in steel works furnaces, initial efforts were directed at detection and prevention of materials entering the steel making process. However, the terrorist threat which has emerged in the past ten years has re-focussed attention on to the prevention of the movement of radioactive materials, ultimately including fissile material, which could be used as weapons. Neutron detection forms an integral part of this screening process, however in terms of cost and sensitivity the equipment employed for this application is no longer fit for purpose.

## 1.2 Radiation detection in scrap metal

Large radioactive sources have been widely and safely used in industry and medicine for many years, as they will undoubtedly continue to be. However the care given to installation and use of such equipment has not always been shown when it comes to decommissioning and disposal. As the sources (often measuring >100Gqbq) are generally housed in large metal containers, for screening purposes, they can easily find their way into scrap destined for recycling, of which vast quantities are consumed by the steel industry (in excess of 300 million tonnes per-annum world wide [2]).

Year	Country	Isotope	Act. (GBq)	Year	Country	Isotope	Act. (GBq)
1982	Taiwan	<sup>60</sup> Co	770	1993	USA	<sup>137</sup> Cs	unknown
1983	USA	<sup>60</sup> Co	930	1993	S.Africa	<sup>137</sup> Cs	<600 Bq/g
1983	Mexico	<sup>60</sup> Co	15000	1994	Bulgaria	<sup>60</sup> Co	3.7
1985	USA	<sup>137</sup> Cs	56	1995	Canada	<sup>137</sup> Cs	0.2-0.7
1989	USA	<sup>137</sup> Cs	19	1995	CzechR.	<sup>60</sup> Co	unknown
1989	USA	Th	unknown	1995	Italy	<sup>137</sup> Cs	unknown
1989	Italy	<sup>137</sup> Cs	1000	1997	USA	<sup>60</sup> Co	0.9
1990	Ireland	<sup>137</sup> Cs	3.7	1997	Italy	<sup>137</sup> Cs <sup>60</sup> Co	200/37
1991	India	<sup>60</sup> Co	7.4-20	1997	Greece	<sup>137</sup> Cs	11 Bq/g
1992	USA	<sup>137</sup> Cs	12	1997	USA	<sup>137</sup> Cs <sup>241</sup> Am	7 Bq/g
1992	USA	<sup>137</sup> Cs	4.6-7.4	1998	Spain	<sup>137</sup> Cs	> 37
1992	Russia	<sup>226</sup> Ra	unknown	1998	Slovenia	unknown	unknown
1993	USA	<sup>137</sup> Cs	37	1998	Sweden	<sup>192</sup> Ir	8
1993	USA	<sup>137</sup> Cs	7.4	2000	Sweden	<sup>252</sup> Cf	unknown
1993	USA	<sup>137</sup> Cs	unknown	2000	UK	<sup>238</sup> U	1g
1993	Kazakhstan	<sup>60</sup> Co	0.3	2010	Italy*	<sup>60</sup> Co	>370

Table 1.1: Incidents involving radioactive material entering the steel making process[2],

\* - found in a scrap container at Genoa port

With each furnace charge weighing tens of tonnes, and without sophisticated detection equipment, it is easy to see how a relatively small source housing, such as the one shown in Fig.1.1, can be overlooked. The majority of orphaned sources are predominantly either alpha or gamma emitters (the commonest isotopes are shown in Table 1.2). While most of these isotopes can in theory be detected to some degree by their gamma emissions, the large mass of steel potentially attenuating emitted gamma radiation, and the relatively high and fluctuating level of gamma background, pose significant problems in detecting even very large sources entering the steelworks.

To combat this problem, high sensitivity gamma portals, generally employing two or more large plastic, or inorganic scintillators, were developed and installed at steel works around the world throughout the 1990s and onwards; one such system is shown photographed in Fig.1.2. Corus RD&T were at the forefront of this work, developing patented techniques employing energy analysis to reduce the effect of background fluctuations, caused by the mass of scrap passing the detection system.



Fig. 1.1: Orphaned  $^{241}\text{Am}$  Source  
found on a British Steel site.

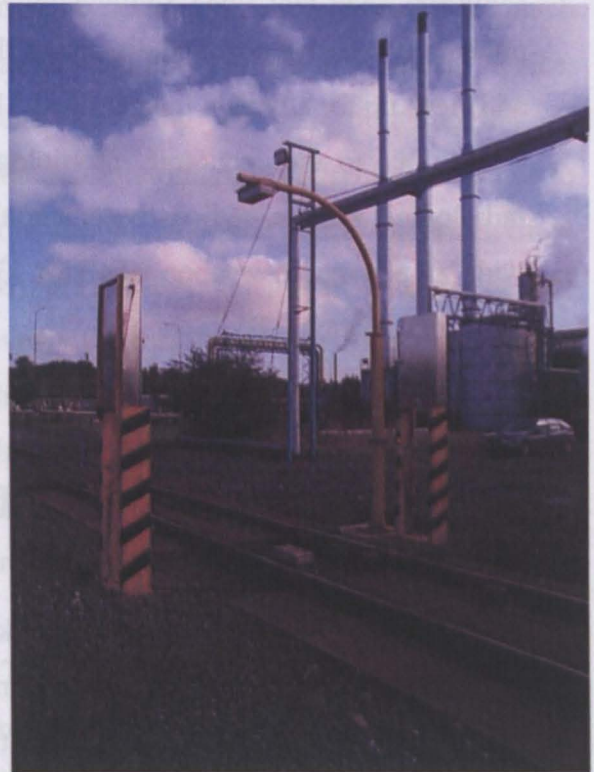


Fig. 1.2: Corus Scrap Radiation  
System(Rotherham)

Isotope	Common industrial uses	Radiation emitted
<sup>241</sup> Am	Oil drilling, moisture gauges	Alpha / Gamma / Neutron
<sup>252</sup> Cf	Oil industry	Neutron
<sup>137</sup> Cs	Industrial gauges	Gamma
<sup>60</sup> Co	Industrial gauges, NDT	Gamma
<sup>192</sup> Ir	Medicine, NDT	Gamma
<sup>238</sup> Pu	Power supplies	Gamma / Neutron
<sup>226</sup> Ra	Medicine, gauging	Alpha
<sup>90</sup> Sr	Power supplies	Beta

Table 1.2: *Common industrial isotopes*

As a result of detector installations and awareness campaigns the number of incidents of sources entering the steel making route has fallen dramatically in recent years. However studies of the effects of these radioactive releases sponsored by the European Coal and Steel Confederation (ECSC) [2] has led to an appreciation of the potentially massive cost and disruption that they can cause; a value put on lost production and clean up for a typical incident was \$10 million.

Due to the economic, physiological and even psychological implications of a radiological release, radioactive material has been identified by security agencies world wide as a possible weapon of terror [3], and the focus for detection has shifted from industry to national borders.

### 1.3 Radiation detection for border security

Following the notorious terrorist attacks in the USA on 11<sup>th</sup> of September 2001, and subsequent incidents in Madrid and London, an extraordinary amount of effort has been spent reducing the possibility of radioactive material being used as a terrorist weapon. The most immediate radiological threat is believed to be a Radiation Dispersal Device (RDD). This can be produced when a quantity of radioactive material is combined with an explosive charge. Although the implications for injury and loss of life posed by an RDD are not great, the resulting social disturbance and economic impact would be significant

[4]. The scale of this problem has been examined in some detail and is being addressed by authorities including the International Atomic Energy Authority (IAEA) [5]:

1. In 1996 Chechen rebels tried but failed to detonate a large  $^{137}\text{Cs}$  source in Moscow [5].
2. IAEA reported that orphaned sources are widespread in the Newly Independent States of the former Soviet Union. In Georgia alone 287 sources have been recovered since 1997 [5].
3. The United States Nuclear Regulatory Commission reports that U.S. companies have lost track of nearly 1,500 radioactive sources within the country since 1996, and more than half were never recovered [4].
4. A European Union (EU) study [3] estimated 70 sources a year are lost from regulatory control, and approximately 30,000 disused sources held in local storage in the EU are at risk of being lost from regulatory control.

However over and above the problem of industrial type sources, is the potential for much graver consequences presented by fissile material - suitable for use in a nuclear device. Since 1990 there have been several incidents involving the theft or smuggling of significant quantities of weapons grade Uranium and Plutonium [3] (Uranium enriched to 20 percent or higher  $^{235}\text{U}$  is considered weapons-usable material). Fissile materials, often known as Special Nuclear Materials (or SNM), are however much harder to detect than industrial gamma sources due to their low levels of gamma emissions (at low energies), which are relatively easy to shield. For Plutonium and in some cases Uranium this problem can be overcome through the use of large area thermal neutron detectors (Section 1.4), however this is by no means a trivial task.

In response to the security threat, over the past few years radiation detectors have been installed at UK ports and airports to screen vehicles and passengers for illegal radioactive substances on entry to the UK. The mobile and fixed detector systems are being deployed by HM Revenue and Customs and the Home Office as part of program Cyclamen costing approximately £100m. A similar program in the United States has seen the installation of over 1000 detectors at 126 points of entry [5]. In both cases the equipment used is based heavily on the portals developed for screening steel scrap, and employs large plastic scintillation detectors. However, a significant addition to the systems used at borders are arrays of thermal neutron detectors, in the form of large  $^3\text{He}$

tubes (typically 8 tubes per system measuring 1.5m long x 50mm diameter filled to 4atms pressure).

While large plastic detectors are well matched to the steelworks application; i.e. very large gamma sources embedded in passive homogeneous bulk material, they are not necessarily ideal for border security: Plastic scintillators offer little energy information and can therefore easily be falsely triggered by medical isotopes and Naturally Occurring Radioactive Materials (NORM), see Table 1.3. Furthermore the neutron sensitivity achieved by  $^3\text{He}$  detectors is limited by the high cost of this technology.

Substance	Composition / Activity (Bq/kg)				Alarms
	$^{40}\text{K}$	$^{226}\text{Ra}$	$^{238}\text{U}$	$^{232}\text{Th}$	
Kitty litter	200 – 300		21 – 140	18 – 43	34%
Abrasives	600 – 10k	30 – 500	30 – 500	40 – 70	8%
Refractory	2k – 4k	40 – 100	40 – 100	70 – 200	8%
Scouring pads	210		350	310	6%
Mica	-				5%
Potassium/Potash	40 – 8k	20 – 1k	230 – 2k	20 – 30	5%
Granite slabs	600 – 10k	30 – 500	30 – 500	40 – 70	4%
Tiles / ceramics	40 – 1k	70	70	70	4%
Trucks and cars	-				2%
<b>Medical -</b>	<b>Average Administered Activity (MBq), Half life</b>				<b>16%</b>
$^{111}\text{In}$	119 MBq 67 hr				
$^{131}\text{I}$	1547 MBq 8 days				
$^{99}\text{Tc}$	626 MBq 6 hr				

Table 1.3: *The commonest materials which contribute to false triggering of portal systems [6]*

The widespread use of medical sources poses a significant problem to security screening. There are about 10,000 patients receiving radioiodine therapy and around 600,000 diagnostic imaging procedures per year in the UK [7]. These patients can trigger radiation portal detectors with potentially distressing consequences and delays. Table 1.4 below shows anecdotal and documented reports of patients activating alarms.

Radiopharmaceutical	Activity (MBq)	Time after Treatment	Location
$^{99}\text{Tc}$	350	3 days	Ferry Port
$^{111}\text{In}$	20	2 weeks	UK
$^{201}\text{Tl}$	80	2 days	UK/Moscow
$^{201}\text{Tl}$	-	9 days	Bank vault
$^{201}\text{Tl}$	-	4 days	The Whitehouse
$^{131}\text{I}$	7000	8 weeks	UK/Bulgaria
$^{131}\text{I}$	148	3½ weeks	Vienna airport
$^{131}\text{I}$	400	6 weeks	Orlando airport

Table 1.4: Medical sources triggering detection systems [7, 8]

A model developed by Zuckier [8] based on US homeland security detectors predicts that a radioiodine patient could trigger a detector after 95 days and a bone scan patient after 3 days. False alarms of this nature are so common in existing portal installations that systems handling high volumes of traffic have to be significantly desensitized to prevent unreasonable delays occurring. As a remedy to these problems attempts have been made, particularly in the USA, to develop a new generation of equipment. Known as Advanced Spectroscopic Portals (ASP) [9], these systems combine spectroscopic gamma detection and higher neutron sensitivity. Images from the ASP test site are shown in Fig 1.3.

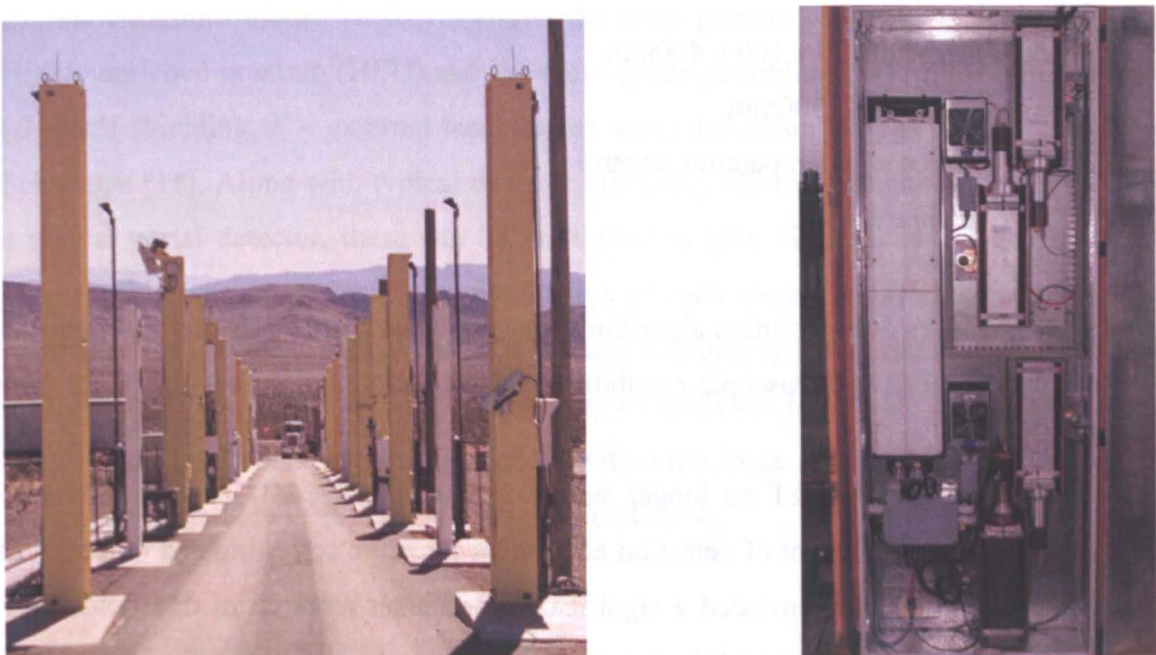


Fig. 1.3: a,(Left) ASP systems undergoing test in Nevada USA, b,(Right) Inside an ASP panel ( $^3\text{He}$  based detector on left, 4 NaI detectors on right).

It has recently been reported [10] that, due to spiraling costs and unsatisfactory performance, roll out of the ASP program has been halted (a typical ASP costs \$822,000, including deployment, versus \$308,000 for the legacy, plastic scintillator, portal monitors). It seems that this failure is most likely due to a lack of emphasis on cost, the highest proportion of which is attributable to the detectors themselves.

## 1.4 Corus Redeem

The steel maker Tata (formerly Corus) has been involved in radiation detection for steel works and border security for almost 20 years. Over 60 Corus designed systems have been installed at steel works and scrap yards. In the past few years through its Redeem brand Tata has been involved in the development of the next generation of portal monitors, both in the UK and the US. This has included participation in ASP trials at the US department of energy nuclear test site in Nevada. A typical detector panel developed for this project is shown in Fig. 1.3b. This panel, of which 4 are deployed in a standard system, contains;

- 4 NaI(Tl) detectors 50 x 100 x 400mm
- 2  $^3\text{He}$  detectors 50 x 1500mm
- 2 Peltier coolers with temperature control
- 4  $^{152}\text{Eu}$  reference sources

The system uses deconvolution algorithms, developed by Corus's partner Symetrica ltd to provide enhanced spectroscopic capability, and was relatively successful in the Nevada trials.

While Tata RD&T no longer supply systems for security portals, they are still active in the development of detection equipment for scrap screening and other industrial applications, and have invested a significant amount on research in this field. Several portals, based in part on the ASP work, have recently been installed at Tata plants in south Wales and Scunthorpe.

## 1.5 Passive neutron detection

Passive gamma and neutron systems rely on the detection of radiation emitted during normal spontaneous decay. Alarms are triggered when the number of particles detected in a fixed period exceeds a threshold based on background radiation levels. This threshold is calculated to give an acceptable false alarm rate, and is typically 1:10,000 false positives (i.e. alarms occurring with no source present), and 1:1,000 false negatives (i.e. no alarm occurring with a source present). As the background is a relatively low number of discreet events a Poisson distribution is used to determine an appropriate threshold level, at 3 to 4 standard deviations ( $\sigma$ ) above the mean background ( $\mu$ ). This threshold is constantly recalculated as background levels change throughout the day.

Within such systems high sensitivity gamma detectors offer excellent sensitivity to most radio isotopes, however as previously discussed they are susceptible to false alarms. Even when spectroscopic detectors are used, for many sources the characteristic gamma signature can be completely lost, due to shielding by a surrounding layer of high density cargo. Fissile materials in particular can be very difficult to detect reliably from their gamma emissions alone. Table 1.5 shows the main gamma peaks for typical SNM; i.e. Highly enriched uranium (HEU) and Weapons grade plutonium (WPu). Shielding factors ( $G$  – self shielding,  $F$  – external lead shield), and attenuation lengths ( $I$ ) are taken from Schweppe [11]. Along with typical detector efficiency ( $E$ ) and attenuation factor ( $D$ ), for a typical portal detector, these can be multiplied to give the detectable signal for each source, at the most significant emission energy of each source. This value can readily be compared to the typical background rate at these energies (given in the final row of Table 1.5). Although for unshielded sources this may be sufficient to activate an alarm threshold ( at  $\mu + 4\sigma$  ) in a realistic screening period, with a moderate amount of shielding present, any gamma signature is easily lost in background noise.

	<b>12 kg HEU (clean, 7% <math>^{238}\text{U}</math>)</b>	<b>12 kg HEU (contaminated, 0.0001ppm <math>^{232}\text{U}</math>)</b>	<b>4 kg WPu (93% <math>^{239}\text{Pu}</math>)</b>
Gamma radiation [9]	84 ks <sup>-1</sup> at 1 MeV	321 ks <sup>-1</sup> at 2.6 MeV	937 ks <sup>-1</sup> at 0.77MeV
Self-shielding of source [9]	$G = 0.10$ for $l = 1.41 \text{ cm}^{-1}$	$G = 0.16$ for $l = 0.87 \text{ cm}^{-1}$	$G = 0.10$ for $l = 2.08 \text{ cm}^{-1}$
External shielding (5 cm of lead) [9]	$F = 0.02$ for $l = 0.77 \text{ cm}^{-1}$	$F = 0.08$ for $l = 0.50 \text{ cm}^{-1}$	$F = 0.0064$ for $l = 1.01 \text{ cm}^{-1}$
Detectable fraction (1 m <sup>2</sup> detector at 1 m)	$D = 0.08$	$D = 0.08$	$D = 0.08$
Efficiency of NaI detector	$E = 0.40$	$E = 0.10$	$E = 0.65$
Detectable signal without lead shield	269 s <sup>-1</sup>	411 s <sup>-1</sup>	4870 s <sup>-1</sup>
Detectable signal with lead shield	5.4 s <sup>-1</sup>	33 s <sup>-1</sup>	31 s <sup>-1</sup>
Background	17 s <sup>-1</sup>	3 s <sup>-1</sup>	73 s <sup>-1</sup>

Table 1.5: *Gamma sensitivity to SNM for large NaI portal detectors- Note while all naked sources have a reasonable detectable signal (above background), only the contaminated source maintains this with shielding present*

As there are few neutron emitting NORM, or medical isotopes, and the neutron background is low, neutron false alarms are rare. They are mostly caused by random variation in background count rate, which can be set at an acceptable level by statistically analysis. Neutrons are also more penetrating than most gamma radiation and therefore more easily detected from within large cargoes. Furthermore neutron sources are also potentially the most serious security threat [12], be they fissile material or large industrial sources (e.g. Am:Be). The benefits of good neutron detectors are therefore clear. However due to cost and space constraints the limited sensitivity of the neutron detectors currently deployed means only relatively large masses of some fissile materials can be detected.

The efficiency and size of the detectors, and their sensitivity to background are the factors which determine the minimum detectable neutron source. In order to maximise sensitivity, data is collected over as long a period as possible as a vehicle passes through the system. Counts produced in several adjacent detectors can be combined, however this

must be done with care as it increases background count rate, and can in some circumstances lower overall sensitivity. A detailed set of empirical calculations used to determine threshold settings for a typical portal system is given in Appendix A.

A summary of calculation of the minimum detectable fissile materials is given in Table 1.6. Included in the table is a  $1\mu\text{g}$   $^{252}\text{Cf}$  source (185kBq), commonly used as a surrogate source for sensitivity testing (more readily available than 1kg of weapons grade plutonium).

Nuclide	Neutron Emitted ( $\text{n.s}^{-1}$ )	Neutron Flux at 1 meter, $\text{n.cm}^{-2}\text{s}^{-1}$
$^{236}\text{Pu}$ , 1kg	$3.6 \times 10^6$	28
$^{238}\text{Pu}$ , 1kg	$2.7 \times 10^6$	21
$^{240}\text{Pu}$ , 1kg	$1.0 \times 10^6$	8.1
$^{242}\text{Pu}$ , 1kg	$1.8 \times 10^6$	14
$^{244}\text{Pu}$ , 1kg	$1.9 \times 10^6$	15
$^{252}\text{Cf}$ , 1ug	$2.3 \times 10^6$	18
$^{241}\text{Am}$ , 1g	1.2	$9.5 \times 10^{-5}$
WGPu Oxide, 1kg	$\sim 1 \times 10^5$	$\sim 0.8$
WGPu Metal, 1kg	$\sim 7 \times 10^4$	$\sim 0.6$
"Dirty" Plutonium*	$\sim 2 \times 10^5$	$\sim 1.6$
HEU 90% $^{235}\text{U}$ 50kg	$\sim 100$	$8.0 \times 10^{-4}$

Table 1.6: Neutron flux from Fissile materials [10]. \* "Weapons plutonium" is relatively pure; typically 94%  $^{239}\text{Pu}$  with 6%  $^{240}\text{Pu}$ , while dirty plutonium, from spent fuel, has higher proportions of the more radioactive isotopes  $^{238}\text{Pu}$  and  $^{240}\text{Pu}$

Although many of these materials can be readily detected in modest amounts, when unshielded, the presence of neutron shielding significantly degrades this performance. It is therefore essential to maximise the overall detector sensitivity, either through improved nominal detector efficiency or through the deployment of the maximum practical effective detector area. To date this requirement has been severely hampered by the high cost of neutron detectors, and as such performance has been compromised.

Furthermore Highly Enriched Uranium (HEU) containing predominantly  $^{235}\text{U}$  spontaneously emits only low energy gamma radiation and very few neutrons; as such it is almost impossible to detect by passive means (neutron flux from HEU at a typical detector can be as low as  $8.0 \times 10^{-4} \text{ n.s}^{-1}$ , Table 1.6).

## 1.6 Active neutron interrogation

Neutron Activation Analysis (NAA) employs a neutron source, either isotopic or discharge tube, to irradiate a target object under inspection. Gamma rays and or neutrons subsequently emitted by the activated object are detected and analysed to determine composition. As well offering the possibility of detecting materials such as contraband and explosives, NAA can provide greatly enhanced sensitivity to fissile materials. NAA techniques can be sub classified as follows:

### 1.6.1 Delayed gamma

The classic technique for NAA is to position a sample in a very high thermal or epithermal neutron flux within a reactor, typically  $10^{12} \text{ neutrons cm}^{-2} \text{ s}^{-1}$  until the sample has absorbed a sufficient neutron flux through non-elastic collision. The sample is then removed from the neutron flux, and gamma radiation emitted by the material is monitored for several hours using a high resolution detector. The resultant gamma spectrum can be used to determine the elemental composition of the sample to an accuracy of parts per billion [13]. As this technique is slow and expensive and requires extremely large equipment it is not applicable to security applications

### 1.6.2 Prompt gamma

Prompt gamma neutron activation analysis (PGNAA) is similar to the above with the exception that the gamma emissions are monitored whilst, or immediately after, the

neutron flux is present. Prompt gammas typically occur between 10ns to 10 $\mu$ s after excitation, and can be the result of either radiative thermal neutron capture, or inelastic scattering, for fast neutron sources. Fig 1.4 shows a typical decay chain resulting in identifiable gamma emissions.

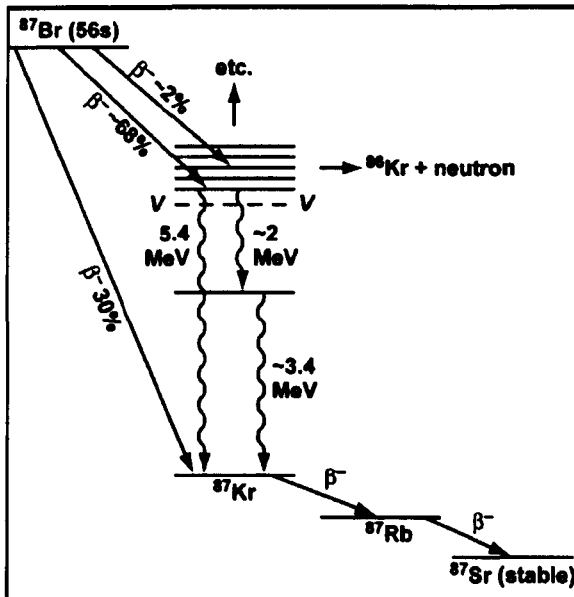


Fig. 1.4: Decay of  $^{87}\text{Br}$  following neutron capture on  $^{235}\text{Eu}$ [13]

As it generally involves the use of significantly smaller neutron sources this technique results in a less accurate analysis of elemental composition. It is also most suited to the detection of highly interacting elements including H, N, U, Pu. Sensitivity to nitrogen in particular makes it of interest in detecting explosives.

However in order to inspect a large volume in a relatively short time (several minutes) a relatively high neutron flux is needed, either in the form of an isotopic source, or neutron accelerator. This requires a significant amount of screening and requires rigorous monitoring. Fig 1.5 shows a typical installation for online analysis of raw material. Arrays of large expensive spectroscopic gamma detectors are also necessary to collect sufficient gamma data to meet target false alarm rates. With presently available technology these constraints are slowing down the introduction of this technique for security screening.

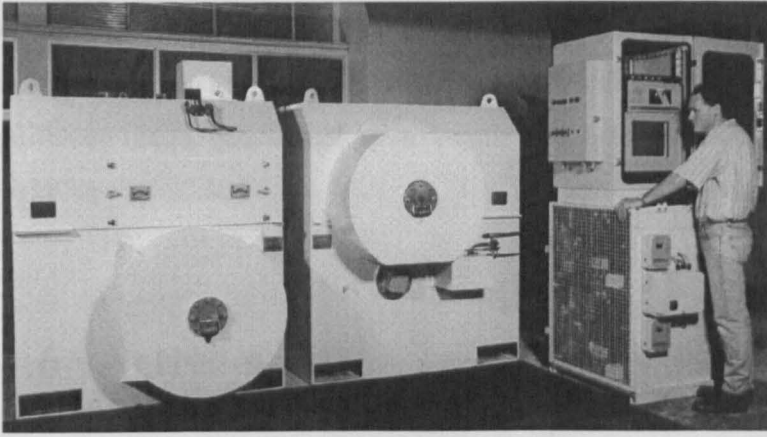
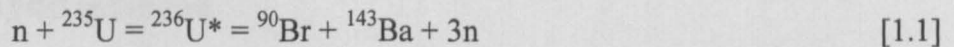


Fig. 1.5: Photograph of the CSIRO NITA cement analyzer[14]

### 1.6.3 Neutron emission

This method requires the use of pulsed neutron sources to induce nuclear reactions in fissile materials in the target. Thermal-neutron induced fission produces two fission fragments and zero to many neutrons. For example:



Decay of the fission fragments frequently leaves the daughter nucleus in an excited state which can lead to further emission of neutrons and gamma rays with energy between 3 to 7 MeV.

Detection of the fission neutrons can be gated to eliminate neutrons from the excitation pulse, therefore resulting in a good signal to noise level. Typical fission yield for nuclear isotopes is given in Table 1.7. This shows that although the neutron yield is an order of magnitude lower than gamma ray yield, the neutrons produced are highly penetrating and potentially easier to detect than high energy gammas. For uranium in particular (with low spontaneous emissions) this could provide an important, identifiable signal.

<b>Yield /fission</b>	<b><sup>235</sup>U Thermal fission</b>	<b><sup>239</sup>Pu Thermal fission</b>	<b><sup>238</sup>U Fast fission</b>
<b>Delayed neutrons</b>	0.015	0.0061	0.044
<b><math>\gamma</math> rays &gt; 3 MeV</b>	0.127	0.065	0.11
<b><math>\gamma</math> rays &gt; 4 MeV</b>	0.046	0.017	0.03

Table 1.7: *Induced neutrons from fissile isotopes[15]*

However this method requires large area, gamma immune neutron detectors, which are currently expensive to produce. It is believed that the development of low cost, high efficiency detectors could be a key enabling factor in the application of this technology.

## 1.7 Requirements for large area thermal neutron detectors

Both passive and, to some extent, active neutron applications require thermal neutron detectors with broadly similar performance characteristics;

- Large detection area
- High efficiency
- Insensitivity to gamma radiation
- Robustness and reliability
- Low cost

Other factors are advantageous for some applications, such as compactness (hand held and transportable devices) and fast response (neutron activation), however it is important that these parameters are not pursued at the expense of the core requirements.

In order to compare the performance of different detection technologies, and to optimize designs, it is necessary to quantify the above characteristics, and particularly

detector efficiency. In the simplest form this is often quoted as percentage efficiency for a given source at a given distance. This Absolute Efficiency is calculated:

$$\frac{\text{Neutrons Detected}}{\text{Total Neutrons Emitted by Source}} \times 100 \quad [1.2]$$

A more general figure for Intrinsic Efficiency is taken as the proportion of neutrons detected against those incident on the detector:

$$\frac{\text{Neutrons Detected}}{\text{Neutrons Incident on Detector}} \times 100 \quad [1.3]$$

To a first approximation, ignoring ground scattering etc., incident neutrons can be calculated as:

$$\frac{\text{Total Neutrons Emitted} \times \text{Detector Cross Sectional Area}}{\text{Distance}^2 \times 4 \pi} \quad [1.4]$$

While the Intrinsic efficiency can usefully be used to compare detectors of different size, where size is not a major constraint, this figure does not give the whole picture, and can prove to be a distraction from the overall goal of the project; which is not only to develop a detector of reasonable efficiency, but also to minimise cost. A more worthwhile target is therefore to optimize performance against manufacturing cost per m<sup>2</sup> of sensitive area, e.g.:

$$\frac{\text{Intrinsic Efficiency}}{\text{Cost} / \text{m}^2} = \% \text{ m}^2 \text{ \$}^{-1} \quad [1.5]$$

The price of prototype / breakthrough developments is however not generally readily available. Even the cost of the raw materials is often difficult to come by; e.g. <sup>3</sup>He supplies are severely restricted, and <sup>6</sup>Li with potential nuclear weapons applications is classed as a controlled substance. Furthermore, the price of these isotopically enriched materials (where available) is far from stable; e.g. in the past twenty years the price of <sup>3</sup>He has risen from \$100 per litre to over \$2000 per litre (at atmospheric pressure)[16].

Taking the more widely available efficiency figures, comparative performance of some large area neutron detectors is shown in Table 1.8. The quoted performance for <sup>6</sup>Li

loaded glass fibres exceeds the rather modest performance of all the  $^3\text{He}$  detectors, but in only relatively small detector size (due to light attenuation in the fibres), and at the expense of interference caused by unwanted gamma sensitivity, and high cost. The PNL detector, developed by Barton et al [17] offers good sensitivity and a reasonable cross sectional area. However in common with all the other systems it employs expensive highly enriched isotopes, in this case  $^6\text{Li}$ .

Detector System	Number of $^3\text{He}$ tubes etc.	Active Size ( $\text{cm}^2$ )	Weight (kg)	Efficiency $^{252}\text{Cf}$ at 1m	Cross section Effic. $\% \text{m}^{-2}$	Gamma rejection
Berthold <sup>[18]</sup>	1 x $^3\text{He}$	558	3.35	0.02%	4.5%	$10^{-5}$
INF <sup>[19]</sup>	12 x $^3\text{He}$	720	18	0.033%	5.8%	$10^{-5}$
ONDAC <sup>[19]</sup>	9 x $^3\text{He}$	4000	58	0.05%	15.7%	$10^{-5}$
Nucsafes <sup>[20]</sup>	( $^6\text{Li}$ loaded fibers)	500	8	0.08%	20.1%	$10^{-2}$
PNL <sup>[17]</sup>	( $^6\text{LiF-ZnS}$ )	1120	12	0.4%	44.9%*	good

Table 1.8: Comparative sensitivity of commercial neutron detectors

\* Figures enhanced due to multiple detectors around source

For comparison the above detectors can be grouped as follows;

- Gaseous – ionisation
- Inorganic scintillation
- Solid organic scintillation
- Liquid organic scintillation

The strengths and weaknesses of these technologies are discussed in some depth by Knoll [21] and Burk [22]. Based on instruments currently available, none meet all the target requirements of sensitivity, cost, robustness etc. However, in general terms gaseous detectors offer better gamma rejection than scintillation detectors, at the expense of robustness and cost. The ultimate sensitivity limit of a detector is determined by the choice of isotope used to capture neutrons and the amount of this material that can effectively be employed within the detector.

## 1.8 Useful neutron interactions

Although neutrons have no charge and therefore have no direct ionizing effect, they do interact with matter due to residual strong nuclear force in the atomic nucleus. As this force has a range little more than the size of the nucleus, for most atoms its effect is small, and therefore neutrons can penetrate tens of centimeters of material. When interactions do occur between a neutron and an atomic nucleus they can fall into three categories;

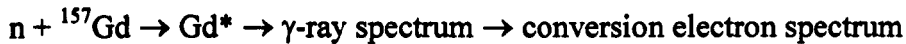
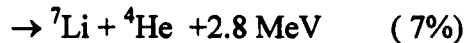
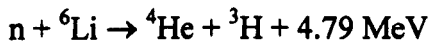
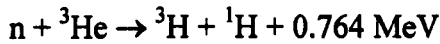
- Elastic scattering
- Inelastic scattering
- Capture

In the first two cases the neutron recoils from a collision, losing a proportion of its energy (through an exchange of momentum). This slowing down (or moderating) of the neutron is most effective with atoms having a low mass (similar to that of the neutron) e.g. Hydrogen. While a proportion of the energy passed to the recoiling nucleus can be detected (through ionization) this is dependent on the energy of the incoming neutron, and at high energy the probability of interactions (cross section) is low. During inelastic collisions a proportion of the energy exchanged to the nucleus is lost as gamma radiation. Again this can be detected, but interactions are rare.

Capture reactions on the other hand are potentially much more useful. In this case neutrons are absorbed into the nearby nucleus. For a handful of isotopes this capture reaction has a reasonable probability of occurring, and results in emission of readily detectable ionizing charged particles. The most significant of these interactions are shown below and summarized in Table 1.9.

	Abundance	Stable Compounds	Cross Section (0.025 eV) barns	Reaction Products	Reaction Energy MeV	Cost £/gm
<sup>3</sup> He	0.000137%	He gas	5330	<sup>3</sup> H + p	0.764	1000+
<sup>6</sup> Li	7.4%	LiF Li Glass	940	<sup>3</sup> H + <sup>4</sup> He	4.78	50
<sup>10</sup> B	19.8%	BF <sub>3</sub> gas BN, B <sub>2</sub> O <sub>3</sub>	3840	<sup>7</sup> Li + <sup>4</sup> He	2.31 / 2.78	5.5
<sup>157</sup> Gd	15.7%	Liquid Scintillator	259,000	γ + e	>72 keV	2 (natural)

Table 1.9: *Properties of most important neutron interacting isotopes[21]*



Although the capture reaction is much more prevalent at low neutron energies (i.e. thermal neutrons <0.025 eV), as shown in Fig. 1.6, the energy of the particles emitted is independent of incoming energy. While this necessarily means all neutron energy information is lost during the reaction, the high energy reaction products are readily detected either in an ionising chamber or scintillation detector. And the higher the energy of these particles the easier it is to discriminate above gamma interference and other sources of background noise. For this reason gadolinium, producing only low energy gamma rays, is of limited benefit as a capture agent. While isotopes of other elements such as cadmium also have high thermal neutron cross section (<sup>113</sup>Cd – 2x10<sup>4</sup> b [23]), like gadolinium these captures reactions result in gamma emissions only. Furthermore the high toxicity of cadmium make it impractical to handle in powder form.

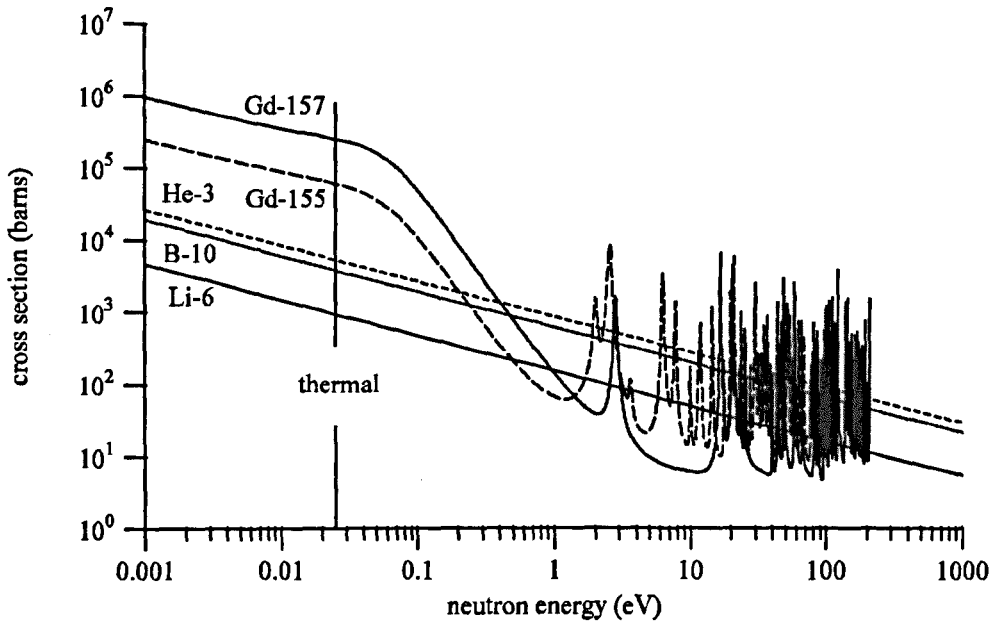


Fig. 1.6: Neutron capture cross section of the most effective detector isotopes[21]

In the selection of an appropriate detection technique for any application, it is necessary to consider the energy of neutrons to be detected. For security applications this is not a trivial question, as neutron spectra from fission sources covers a wide energy range, see Fig 1.7. Furthermore the degree to which neutrons emitted by a target source are moderated can be highly variable, especially for large freight containers containing a wide variety of cargo [24].

If screening is ignored in the first instance, it can be assumed that the energy distribution of the neutrons produced is given by the Watt distribution, with a peak at around 1 MeV. The formula for this [25], can be expressed as a function of energy  $E$ , where  $C(sf)$  is the probability of spontaneous fission neutrons and  $a$  and  $b$  are constants:

$$f(E) = C(sf) \cdot e^{\left(\frac{-E}{a}\right)} \cdot \sinh(\sqrt{bE}) \quad [1.7]$$

For spontaneous fission of  $^{240}\text{Pu}$  and  $^{252}\text{Cf}$  the Watt distribution constants are [18]:

$$^{240}\text{Pu}; a = 0.799 \text{ MeV}, b = 4.903 \text{ MeV}$$

$$^{252}\text{Cf}; a = 1.025 \text{ MeV}, b = 2.926 \text{ MeV}$$

The graphs produced using this formula are shown in Fig. 1.7. Neutron spectra for other fissile materials are given in [18], and it is found that they are all similarly broad. While this energy distribution is further extended down to thermal energies by moderation, in potential cargos and the surrounding environment, a relatively high proportion of incoming energy is many orders of magnitude above the very low thermal energy (0.025 eV) preferred for capture reactions.

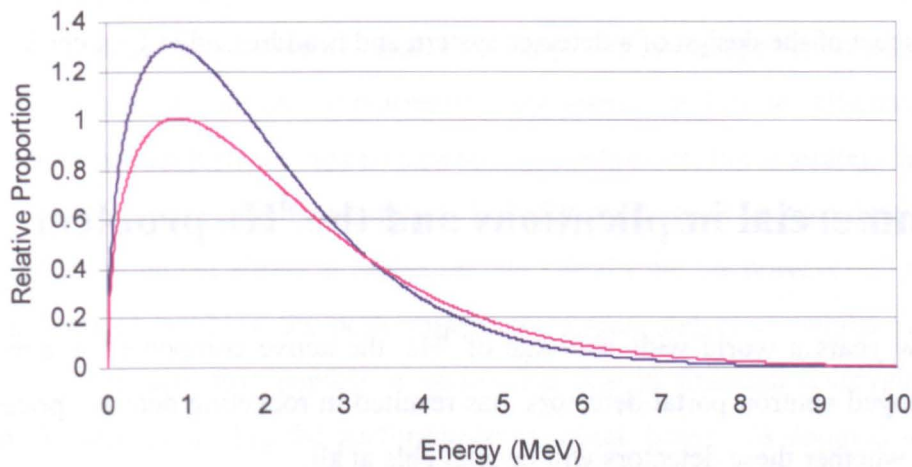


Fig. 1.7: Fission neutron spectra for  $^{240}\text{Pu}$  (blue line) and  $^{252}\text{Cf}$  (red line), approximated by Watt distributions calculations [1.7].

It is also important to consider this ‘Foreground’ signal in the context of the ever present (if somewhat fluctuating) ‘Background’ noise. The neutron background is primarily composed of neutrons created as a result of spallation, of atmospheric nitrogen and oxygen nuclei as well as heavy nuclei in the earth, by cosmic ray particles. Experimental work and modelling carried out by Florek[27], Frank[28], Forman[29] and others, suggests the neutron background has a peak at lower energy than the fission spectrum (< 1 MeV) and a significant downward direction (with a strong boundary effect at ground level). While less than conclusive, this suggests the directionality and energy composition of the neutron background could be differentiated from fission sources. However the moderation resulting from moisture and organic material in the earth, as well as cargo etc, would make any system attempting to exploit these differences fraught with difficulty. Furthermore fast neutron detectors are inherently inefficient, and as a result the very large detectors required would be impractical to deploy.

Thermal detectors while having no energy information, and little or no directionality, are far more efficient, but require some form of moderator to detect the intermediate and fast neutrons emitted by SNM. As efficiency is by far the most important consideration **for this application only thermal neutron detectors will be considered.** The amount and distribution of the moderator material within the detector is however fundamental to the sensitivity achieved by the system, and must be closely matched to the target energy of the incoming neutron flux. For applications where the neutron energy spectrum is broad, choice of moderator and optimization of its geometry is far from trivial. This aspect of the design of a detector system and is addressed in Chapter 3.

## 1.9 Commercial implications and the $^3\text{He}$ problem

In the last few years a world wide shortage of  $^3\text{He}$ , the active component in almost all currently deployed neutron portal detectors, has resulted in rocketing detector prices, and worries about whether these detectors will be available at all.

With the exception of Gadolinium, which only produces low energy gamma rays which are difficult to readily discriminate, the isotope with the highest useful cross section is  $^3\text{He}$ . Furthermore Helium is stable, and can be pressurised to several atmospheres.  $^3\text{He}$  detectors are insensitive to gamma radiation, and deposits sufficient energy into a charged particle to generate a neutron signal which is relatively immune to noise. As a result gas filled proportional detectors can be manufactured from  $^3\text{He}$  which have a very high effective sensitivity to thermal neutrons (up to 77% for a 4 atms tube [12]). When combined with a suitable thickness of moderator (typically 20 – 50mm), a very useful detector can be constructed.

$^3\text{He}$  tubes are therefore the most common commercial neutron detector, and are included as standard in most security portals. However  $^3\text{He}$  is very expensive, currently in excess of \$1000 /gm (based on discussions with manufactures of  $^3\text{He}$  detectors) . It occurs naturally in very small quantities, from which it cannot be economically extracted. The only current means by which it is produced, in any quantity, is as a by product of the nuclear weapons industry, where it is extracted from Tritium during reprocessing. Tritium decays to  $^3\text{He}$  with a half life of 12.32 years [1.8], and as such has to be reprocessed on a fairly regular basis.



As a result of this,  ${}^3\text{He}$  has been stock piled for some time by the US government. However due to recent increases in its use these stock piles are now being rapidly depleted, to such an extent that it has been reported, by Kouzes [30], that in the near future no more  $\text{He}^3$  will be released for use in detectors. The remaining reserves are being held for other applications, such as cryogenics <1K, for which there is currently no alternative technology.

For security systems, and for many industrial applications, sensitive thermal neutron detectors are an irreplaceable component. Finding an alternative to  ${}^3\text{He}$  based detectors is therefore not only commercially worthwhile, but is strategically important.

There are currently a number of alternative thermal neutron detection technologies under development aimed at replacing  ${}^3\text{He}$  [21,30]. So far however all these systems fall well short of reaching the performance of existing detectors, whilst exceeding them in price. If this situation persists it seems that due to financial constraints the chance of significantly enhancing the performance of portal systems is doomed to failure. Kouzes [31] describes the issue well, particularly with regard to the weak gamma and neutron emissions from HEU. He concludes that very large area detectors could provide a solution to this problem. However such systems would require a fall in detector costs of at least an order of magnitude. Current developments focussed on replacing  ${}^3\text{He}$  are not attempting to achieve this.

Selection of the ideal capture agent is however not simply a decision that can be made on technical merit, as commercial and strategic availability of materials must also be considered. A fundamental part of the cost of currently available detectors is in raw materials, and particularly the isotopically enriched capture agent. To achieve a detector that is not only low cost, but at a stable cost it is essential to use readily available materials and chemicals. In the first instance the preference must therefore be to use non-isotopically enriched materials.

## 1.10 Target specification

While a degree of flexibility is undoubtedly necessary during a development of this sort, it is important to have some form of specification against which to work, in order to judge the success of the project.

Over the past ten years various standards have been produced for portal systems, by the IEA [32], British Standards (BS IEC 62244:2006) [33] and most recently by the US Department of Homeland Security (Performance Specification - Advance Spectroscopic Portal ASP [34]). All of these documents quote performance requirements for complete systems, in terms of probability of detection and false alarms e.g.;

- 95% probability of detecting  $^{252}\text{Cf}$  source emitting  $1 \times 10^4$  neutron/s
- False alarm rate (in the absence of a source) 0.1%

These sensitivity figures are typically to be achieved with an exposed source passing the detection system at 2m distance and at a fixed speed of 8 km/hr.

Numerous other requirements include; vertical coverage, timing accuracy, robustness, reliability etc, and importantly a figure for rejection of gamma interference; for the ASP program this requires that less than 0.0001% of incident gamma rays be falsely identified as neutrons.

While many of these parameters can be tested on an individual detector (e.g. gamma rejection), the sensitivity requirements, by definition, require something close to an entire portal system. The numerous detectors and associated infrastructure needed for this is felt to be outside the scope of this project. However existing installations which do meet these performance targets can be used to provide a benchmark. These systems are invariably comprised of  $^3\text{He}$  tubes, which in general achieve the following sensitivity;

- Intrinsic thermal neutron efficiency (4 atms tube) = 77% [14]
- Fission neutrons efficiency (with appropriate moderator) < 16% [19]

In order to calculate sensitivity required by the ASP specification it is necessary to take into account the background count rate, count period etc. Using Poisson distributions and making assumptions about background rate it can be calculated that a single panel must

achieve an average count rate of  $>10\text{cps}$  (see Appendix A). This equates to an overall sensitivity of  $3\text{cps}$  for  $1\text{ng } ^{252}\text{Cf}$  ( $2.3 \times 10^3 \text{ n/s}$ ) at  $2\text{m}$ . As this figure can be tested with readily available sources it represents a good target for the development.

## **1.11 Conclusions**

This project will focus on the development of a large thermal neutron detector, optimised for cost and efficiency, with specific application to security screening.

In order to achieve this aim, readily available, commercial components and cheap bulk materials must be used. Manufacturing techniques must be simple, with low component count and opportunities for process automation. While the finished detector must be robust, reliable and readily integrated, with minimal operating overheads, such as cooling systems. Sensitivity and rejection of background interference, particularly from gamma radiation, are the key parameters for optimisation. Developing and characterising this new class of detector is the challenge of this project.

# Chapter 2

## Benchmark thermal neutron detectors

### 2.1 Introduction

A novel thermal neutron detection system, based on a laminar combination of scintillators and light guides, was demonstrated by Barton et al. [17] at the Polytechnic of North London (PNL) in 1985. Work has been done to refurbish one such detector moth-balled from the project, in order to demonstrate the suitability of this type of instrument for security application.

A large  $^3\text{He}$  based detector developed previously by the author, for use on security portals, has also been refurbished and evaluated. Both these systems represent benchmarks for thermal neutron detection against which the performance of newly developed techniques can be compared.

### 2.2 Background to the design of the PNL $^6\text{LiF}$ detectors

These detectors, originally designed for use in low background multiplicity measurements, are constructed from a linear arrangement of panels, comprising alternate layers of: moderator, scintillator / capture mixture and light guides. These are housed in a light tight assembly, with two 135 mm diameter photomultiplier tubes (PMT) mounted at each end, as shown in Fig. 2.1 & Fig. 2.2.

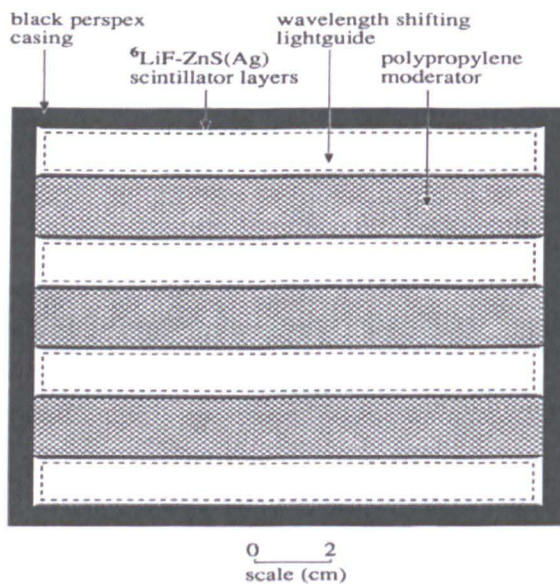


Fig. 2.1: Cross section of PNL  $^6\text{LiF ZnS}$  detector

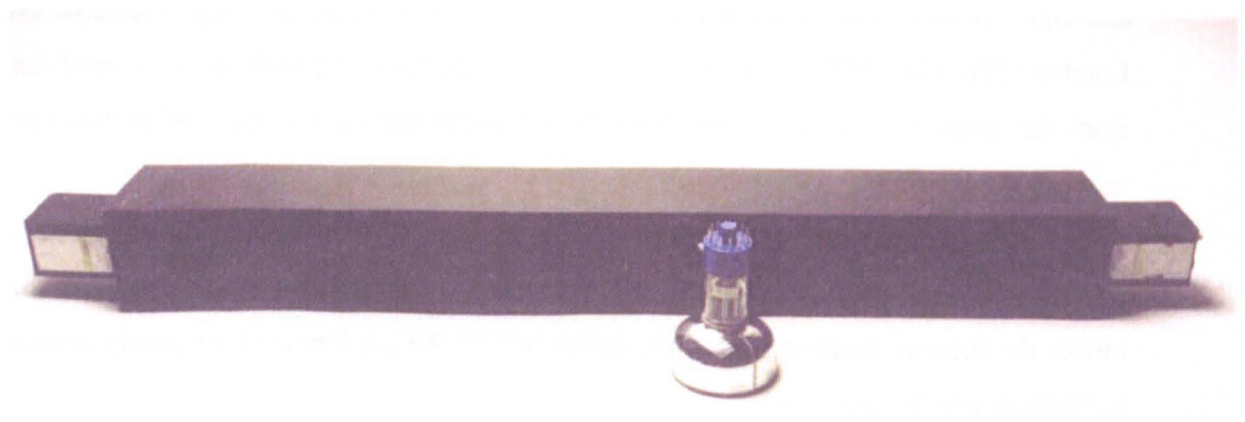


Fig. 2.2: Photograph of PNL  $^6\text{LiF ZnS}$  detector

The scintillator sheets are formed from eight  $100\ \mu\text{m}$  layers of  $^6\text{LiF:ZnS:silicone}$  elastomer, coated onto aluminized polymer film. These sheets are bonded onto both sides of three polypropylene moderator slabs and two internal faces of the enclosure. Wavelength shifting light guides are interleaved between these layers, leaving an air gap between the surface of the scintillator and the light guide (thus allowing total internal reflection in the light guide). The light guides are doped with a fluorescent compound, which absorbs and re-emits scintillated light at a shifted wavelength. A proportion of this isotropic emitted light is captured in the light guide and transmitted to the PMT to

generate a measurable electrical impulse. A simplified version of the assembly is shown in Fig. 2.3.

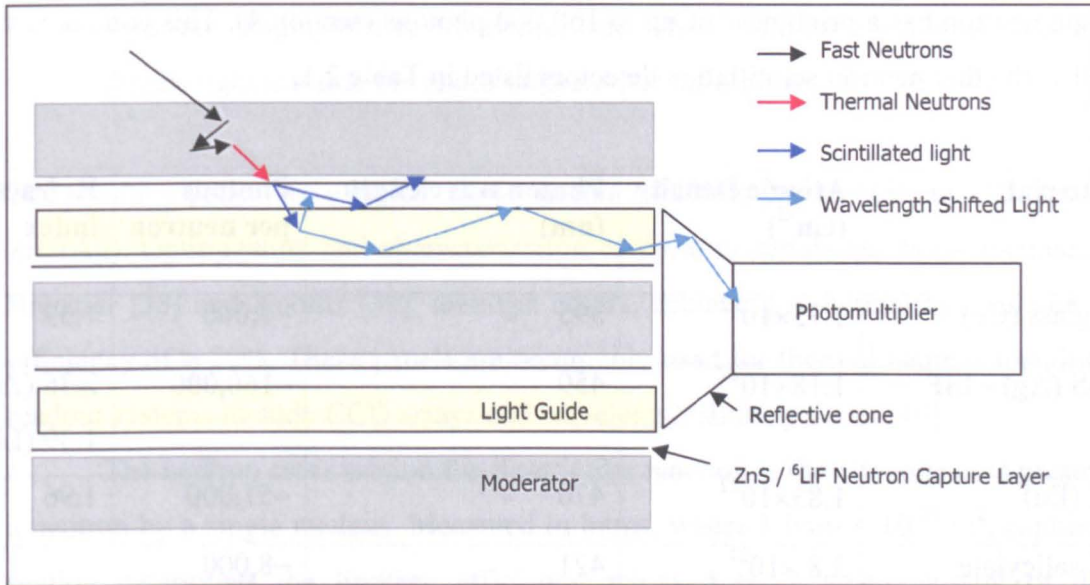


Fig. 2.3: Simplified schematic of the PNL detector assembly

With an active volume of 90 x 15 x 15 cm, an efficiency of 37% for  $^{252}\text{Cf}$  fission neutrons (8 detectors surrounding source), and inherent insensitivity to gamma radiation, this design seems an ideal candidate for the next generation of portal detectors. However the cost of enriched Lithium has spiralled in recent years. Furthermore, as  $^6\text{Li}$  has applications in the nuclear weapons industry (in the form of  $^6\text{Li}$  deuteride [143]), it is a controlled substance, and simply acquiring it for evaluation purposes has proved extremely difficult. Nevertheless several of the PNL detectors, salvaged by John McMillan (co-author to the original work), were available to the University of Sheffield, and as such provided an ideal starting point for this development.

Of all the useful neutron absorbers, the  $^6\text{Li}$ , n reaction releases the most energy to its reaction products. These heavy charged particles ( $\alpha$  and triton) are ideally suited to readily transfer their energy to a nearby scintillating compound, resulting in the brightest possible scintillation event.



In the form of lithium fluoride it is available as a highly stable, fine white powder. Although transparent in crystal form, from UV to infrared [35], as a powder it is relatively

opaque and as such its optical properties are not ideal. It is however quite adequate for use in thin films.

Combined with the very efficient scintillator, ZnS(Ag) the scintillation event for a single neutron has a brightness of up to 160,000 photons (section 4). This compares very well with other neutron scintillation detectors listed in Table 2.1.

Material	Atomic Density (cm <sup>-3</sup> )	Photon wavelength (nm)	Photons per neutron	Refractive index
Li glass (Ce)	1.75×10 <sup>22</sup>	395	~7,000	1.59
ZnS (Ag) - LiF	1.18×10 <sup>22</sup>	450	~160,000	2.36 (ZnS) 1.39 (LiF)
LiI (Eu)	1.83×10 <sup>22</sup>	470	~51,000	1.96
<sup>6</sup> Li salicylate	3.8 ×10 <sup>21</sup>	421	~8,000	
<sup>10</sup> B - Plastic	3.0×10 <sup>21</sup>	425	~10,000	1.58
BN (natural B)	6.0×10 <sup>22</sup>	~400	~3,500	1.6 – 2.2
B - ZnS	~1×10 <sup>22</sup>	450	~80,000	~2.2

Table 2.1: *Properties of neutron sensitive, scintillating materials [21,22]*

This combination of <sup>6</sup>LiF:ZnS(Ag) is by no means unique to this detector. Neutron sensitive screens (commercially available from Applied Scintillation Technologies [36] amongst others) commonly employ this mixture. The recipe for manufacturing these screens is determined by the properties of the materials involved as follows:

- <sup>6</sup>Li reaction products have a short transmission range, therefore particle sizes must be small <10 μm.
- Opacity of ZnS and LiF limits optical transmission length, therefore thickness < 200 μm.
- In order to capture the reaction products in the ZnS, <sup>6</sup>LiF particles must be well surrounded, the optimum mass ratio of <sup>6</sup>LiF:ZnS(Ag) is generally 1:3 to 1:4 [37].

- Both compounds are inert powders and can therefore be readily combined with a clear binder such as silicone or epoxy compounds.
- As the thin layers produced are not mechanically self supporting they require a substrate. Highly reflective aluminized Mylar film is a suitable backing as it directs light towards the photo-collector, or light guide.

The resulting panels have typical concentration of 40 mg/cm<sup>2</sup> of <sup>6</sup>LiF and 120 mg/cm<sup>2</sup> of ZnS(Ag). Optimization and characterization of these materials has been documented by Brenzier [38] and Koontz [39], amongst others, achieving a thermal neutron conversion efficiency of > 20%. These panels are commonly used for thermal neutron imaging, with readout systems include CCD arrays and wavelength shifting fibers [40].

The neutron cross section for a particular reaction is the effective area presented to a neutron by a single nucleus. Measured in barns, where 1 barn = 10<sup>-28</sup> m<sup>2</sup>, capture cross section determines the limiting efficiency achieved by a given amount of detector material, although ultimately sensitivity is also significantly affected by the microscopic and macroscopic geometry of the detector. i.e. the size and shape of the detector, and how the charged particles produced are subsequently detected.

In the first instance an approximation of the amount of material required can be made by converting microscopic cross section ( $\sigma$ ) into macroscopic attenuation coefficient ( $\Sigma$ ), by multiplying  $\sigma$  by the number of atoms present in a given volume.

$$\Sigma = \frac{\sigma \times L \times d}{W} \quad [2.1]$$

Where  $L$  = Avogadro's constant,  $W$  = molecular weight, and  $d$  = density. For <sup>6</sup>LiF;  $W$  = 25,  $d$  = 2.64 g/cm<sup>3</sup> and thermal neutron microscopic cross section for <sup>6</sup>Li  $\sigma$  = 940 b (or 940 x 10<sup>-24</sup> cm<sup>2</sup>) [134].

$$\begin{aligned} \Sigma &= (6.022 \times 10^{23}) \times (940 \times 10^{-24}) \times 2.64 / 25 \\ \Sigma &= 59.75 \text{ cm}^{-1} \end{aligned} \quad [2.2]$$

The proportion of neutrons captured is calculated as 1 - e<sup>-59.75 x thickness</sup>

Therefore the thickness of  ${}^6\text{LiF}$  required to capture say 30% thermal neutrons =  $\ln(1-0.3) / -59.75 = 60 \mu\text{m}$ . At a density of  $2.64 \text{ g cm}^{-3}$  for LiF this equates to a coating mass of  $158 \text{ gm}^{-2}$ .

Due to restrictions on the sale of  ${}^6\text{Li}$  no price was available for  ${}^6\text{LiF}$  in reasonable quantities. However a budget price of  $\$40 \text{ g}^{-1}$  for  ${}^6\text{Li}$  metal was supplied by Cambridge Isotope Laboratories (November 2011). As  ${}^6\text{LiF}$  contains 27%  ${}^6\text{Li}$  by mass the cost of  ${}^6\text{LiF}$  can be estimated to exceed  $\$11 \text{ g}^{-1}$ . A  $1\text{m}^2$  detector having eight layers at  $158 \text{ g}$  of  ${}^6\text{LiF}$  [2.2] therefore equates to a minimum cost of  $\$13,904$ .

## 2.3 Wavelength shifting light guides

The PNL detector employs four rectangular wavelength shifting light guides to collect light from the scintillating sheets. These 10mm thick, parallel sided plates form a critical component of the system. Manufactured by Rohm & Haas, from clear acrylic (otherwise known as Perspex, or Plexiglas) dyed with fluorescent BBQ (Benzimidazo-benzisochinolin-7-on), they were specifically marketed for scientific applications, e.g. large calorimeters use in high energy physics experiments [41]. The light guides have the following characteristics:

- Sufficient fluorescent dye to absorb a significant proportion of the light produced by the scintillator.
- Isotropic emission of light, at a wavelength shifted sufficiently to prevent re-absorption, yet short enough to be within the photomultiplier sensitivity range.
- Transmitted light must be delivered to photomultiplier with minimum re-absorption or surface losses (cast sheets with polished edges)

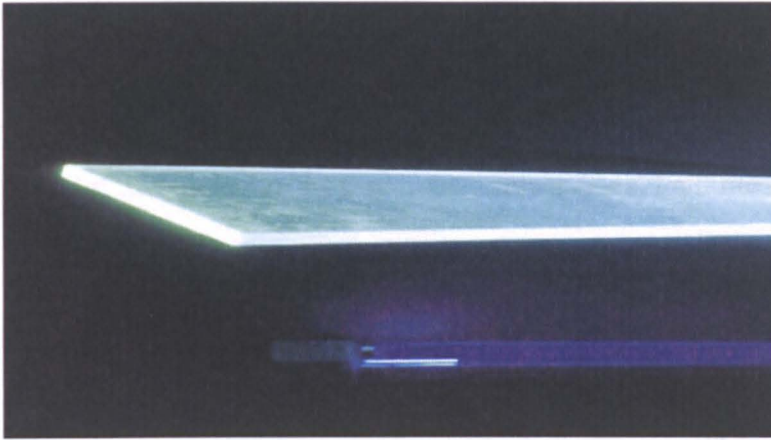


Fig. 2.4: *BBQ* doped wavelength shifting light guide under UV illumination

BBQ is close to an ideal dye for this application, as it is readily soluble in many solvents (e.g. toluene, xylene, white spirit), matches the emission peak of ZnS(Ag) at 450 nm, and re-emits with a small Stokes shift (<560 nm), although reports of this are contradictory [42, 43]. Though the green light it produces has a longer wavelength than the ideal 320 – 450 nm peak of a bialkali PMT, it is as close as is realistically practicable (given that re-absorption must be avoided), and still below the 600nm cut off.

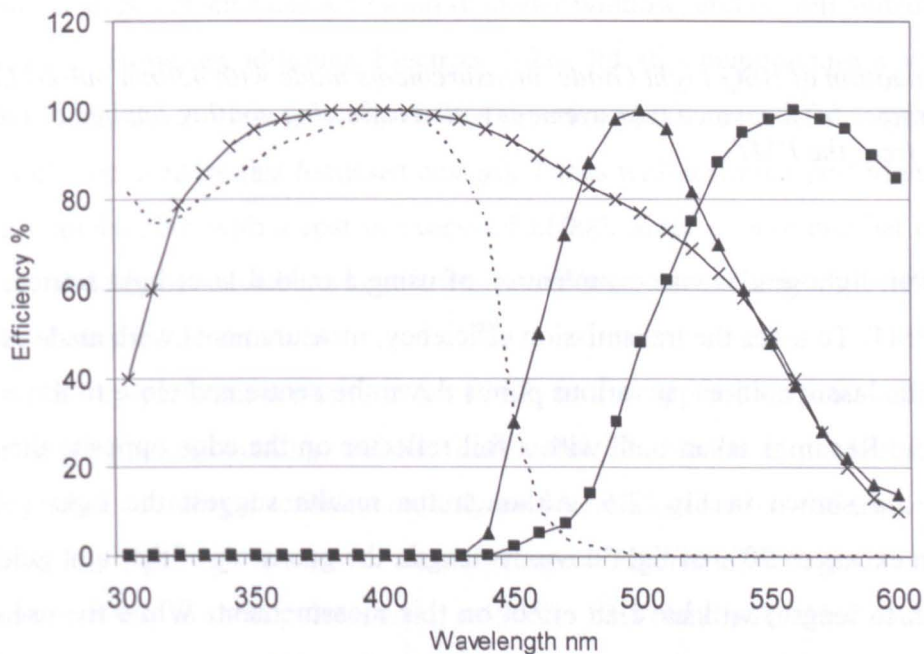


Fig. 2.5: *BBQ* absorption peak (dashed line) / emission peaks (squares[42], triangles[43]), with normalised photomultiplier bialkali response (crosses). Note, typical absolute bialkali efficiency is 30%.

The amount of light transmitted to the PMT directly affects the maximum size and sensitivity of the detector, and its performance at discriminating gamma interference and other sources of noise. It is believed that optimisation of the light guides and their coupling can be improved from the PNL detector.

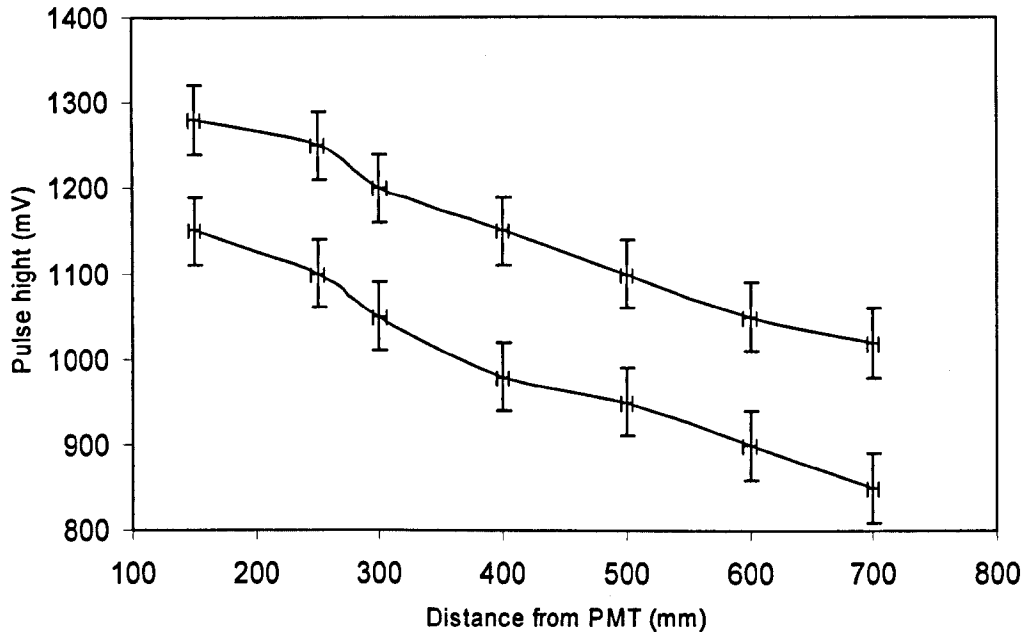


Fig. 2.6: Attenuation of BBQ Light Guide, measurements made with 450nm pulsed LED. The top line shows performance improvement with a reflecting coating applied to the edge furthest from the PMT

One of the PNL light guides was examination of using a pulsed laser light source, and a standard 5" PMT. To assess the transmission efficiency, measurements were made of pulse height, with the laser positions at various points down the centre and close to the edge of the light guide. Readings taken both with a foil reflector on the edge opposite the PMT, and without are shown in Fig. 2.6. Although the results suggest the light guide is attenuating in excess of 20% of light down its length, the geometry of the light guide (i.e. ratio of width to length) will have an effect on this measurement. While the use of the reflector does not improve results as much as could be hoped (in theory a perfect reflector would increase performance by close to 100% near to the coated end), it offers an avenue of investigation worth pursuing in the development of the next detector.

Refurbishment of the PNL detector would ideally include removal and cleaning of light guides, to improve light transmission and ensuring an adequate air gap was maintained between the scintillator. However in these units the casing around the main body of the detector was permanently bonded together, preventing access to internal components.

The light guides are air coupled to the PMTs. The air coupling gap is approximately 30 mm. A cone formed from reflective foil, along with foil coating on the ends of the moderator slabs, are used to improve coupling efficiency. Although the housing of this detector precludes improvements to this geometry, future designs could incorporate a more sophisticated light guide such as the compound parabolic concentrator (Winston Cone), described by Leverington [45].

## 2.4 Photomultiplier tube selection

The photomultiplier tubes (PMTs) used in the PNL detectors were EMI type 9791 KB. This 10 stage detector has a 125mm diameter window, and is well suited to single photon counting. However, although Electron Tubes Ltd still manufacture a wide range of the EMI tubes, the 9791 is now obsolete (“Venetian blind” tubes of this type have now been entirely replaced by fast focussed design). Tubes with a similar performance specification are available, but with a cost in excess of £1000. Since a large number of tubes from the original detectors have been kept it was possible to test and select the best tubes for use in the refurbished detector.

The key performance criteria for PMTs in this application are: sufficiently high gain for single photon counting, and low dark noise. Dark noise in particular is a problem for the photon counting discriminator, and can potentially lead to false triggering. Tubes were tested in a light tight box, over the full range of operating voltages, both for dark count, and sensitivity to short pulses, using a 450 nm IBH Nano pulsed led source, attenuated by a 0.1% neutral density filter. Some of the results from these tests are shown in Fig. 2.7. It was found that dark count in particular varied widely across the sample, from rates below  $100 \text{ c.s}^{-1}$  to over  $1000 \text{ c.s}^{-1}$ . It is interesting to note that despite wide differences in dark counts produced by each tube, they all reach a similar plateau when exposed to a pulsed light source (Fig 2.8). This suggests some proportion of the dark counts only occur when

the PMT is inactive. A discussion of the sources of PMT noise, and their contribution to false counting, is made in section 6.

From the photomultipliers tested, the two selected, based on low dark noise and stable count rate across a wide operating voltage, were; Serial Numbers – 6720 and 6769.

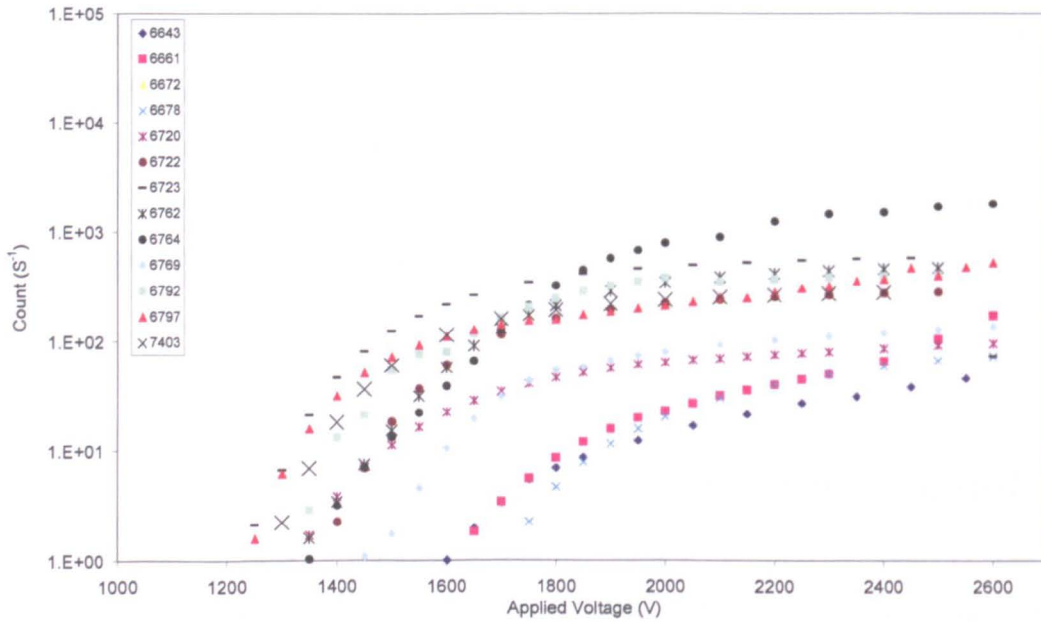


Fig. 2.7: EMI 9791 Photomultiplier Testing – Single photon dark count (note variability of plateaux count rate)

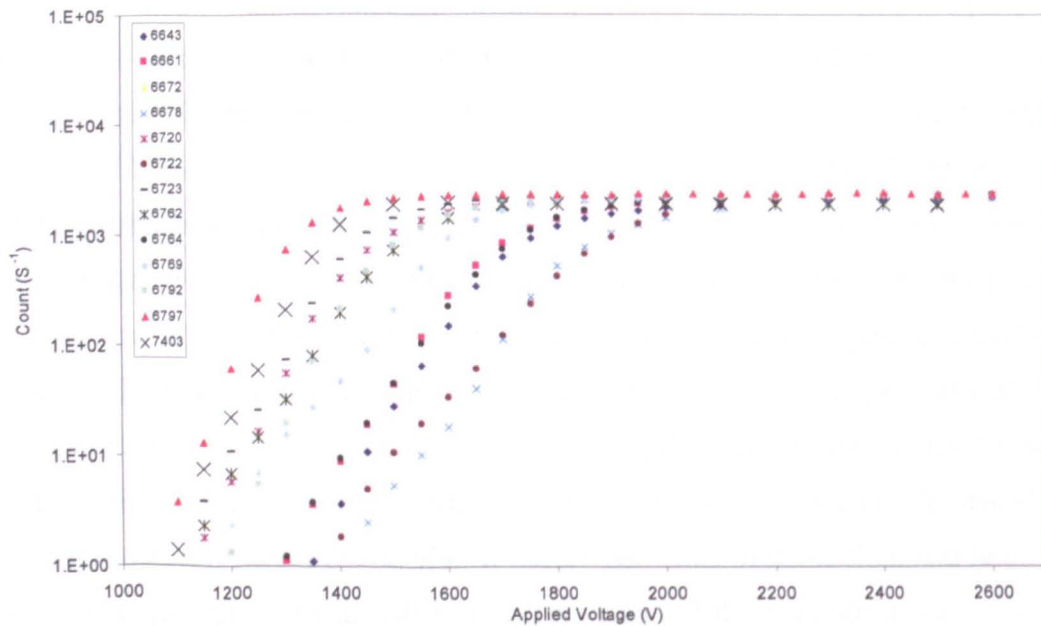


Fig. 2.8: EMI 9791 Photomultiplier Testing – Single photon count rate pulsed light source (note variable roll off voltage but consistent plateaux level)

## 2.5 Signal processing

Although ZnS is a very efficient scintillator, self absorption in the scintillating layer and inefficiencies in coupling and transmission of light to the PMTs result in a very small signal generated by the PMT. Added to this the fluorescence of ZnS has a long and complex decay with components running into several tens of  $\mu\text{s}$  [39]. As a result the signal generated by a single neutron is not so much a single smoothly decaying impulse as a staggered train of pulses, see Fig. 2.9. Differentiating these pulses from those caused by photomultiplier noise and gamma interference requires careful consideration.

Pulse discrimination based on techniques employing pulse shape, for use with ZnS(Ag), has been described by Wright [46]. This method exploits the significant difference in decay time between scintillation events caused by gamma, or electron, excitation ( $<9\text{ ns}$ ) and those caused by charged ions, i.e. alpha / tritons from the neutron  ${}^6\text{Li}$  reaction, ( $>300\text{ ns}$ ). While on the face of it this difference can readily be detected, this is only the case if sufficient light is present, i.e. a clean large signal from the PMT. However with the PNL detector this is not the case, as shown in Fig. 2.9.

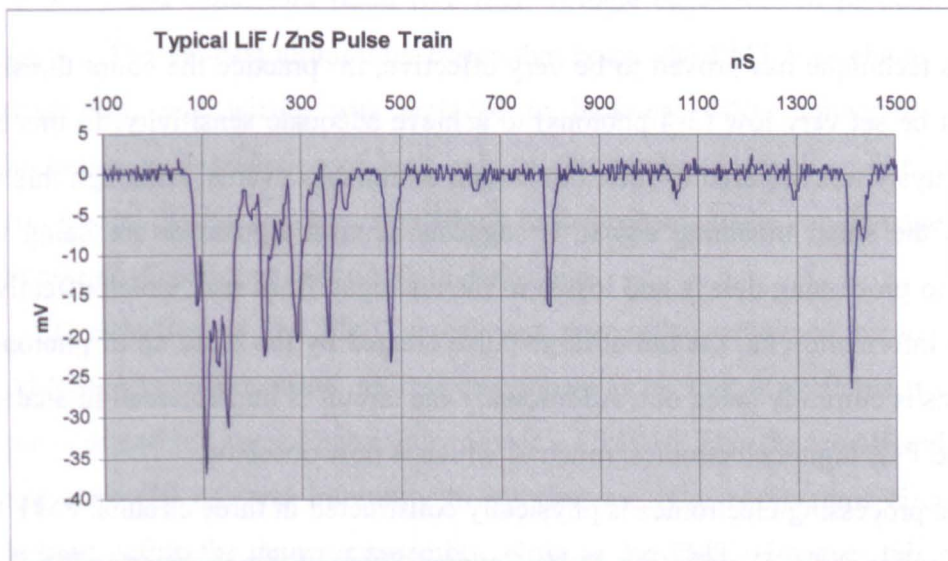


Fig. 2.9: Neutron signal pulse train produced by ZnS(Ag) on 400mm light guide with  ${}^{241}\text{Am}$   $\alpha$  source

An alternative approach developed by Davidson [47] based on Photon Counting has therefore been employed. This uses differentiation to produce a train of pulses, which can be readily counted. Two PMTs are used in coincidence to trigger a timer. Counts recorded above a preset level in a fixed time period are then identified as neutrons. An additional timer is used to introduce a dead time after the count period to prevent re-triggering.

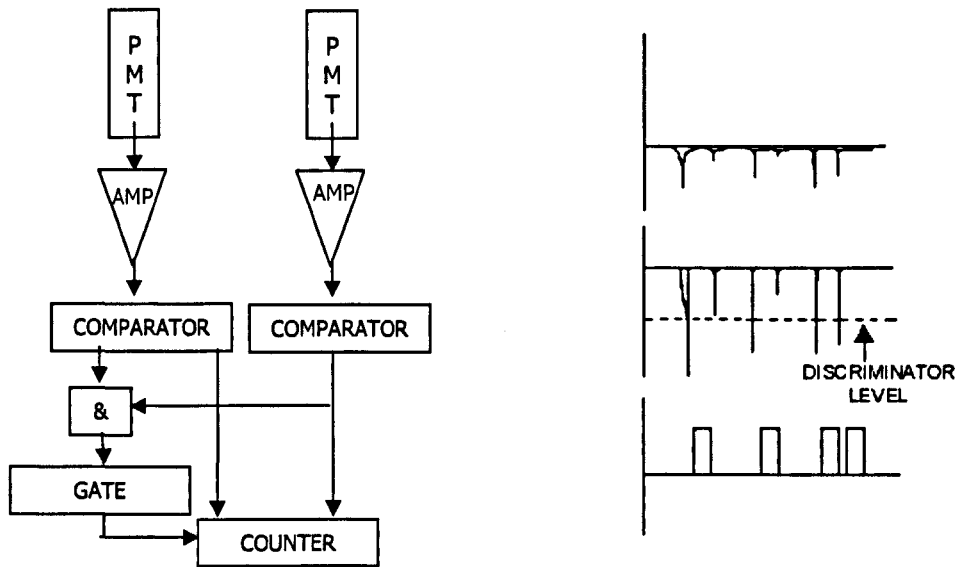


Fig. 2.10: (left) *Flow chart of the photon counting pulse discrimination technique*, (right) *Signal path: Input – differentiated – digitized*

Although this technique has proved to be very effective, in practice the count threshold required must be set very low (3-4 photons) to achieve adequate sensitivity. In this case some post analysis was required to filter out certain extraneous events. Although this was partly due to the small incoming signal, it suggests neutron signatures are being lost, possibly due to processing delays and losses in the analogue front end, which effectively discard some information i.e. the initial large pulse created by the build up of photons in the first 100 ns is currently gated out. Additionally the circuit is implemented in analogue and solid state TTL digital electronics, much of which is now obsolete.

The signal processing electronics is physically constructed in three circuits: PMT bias resistors / capacitor chain, Digitization, Pulse Counter. Some of this is shown in Fig. 2.11.

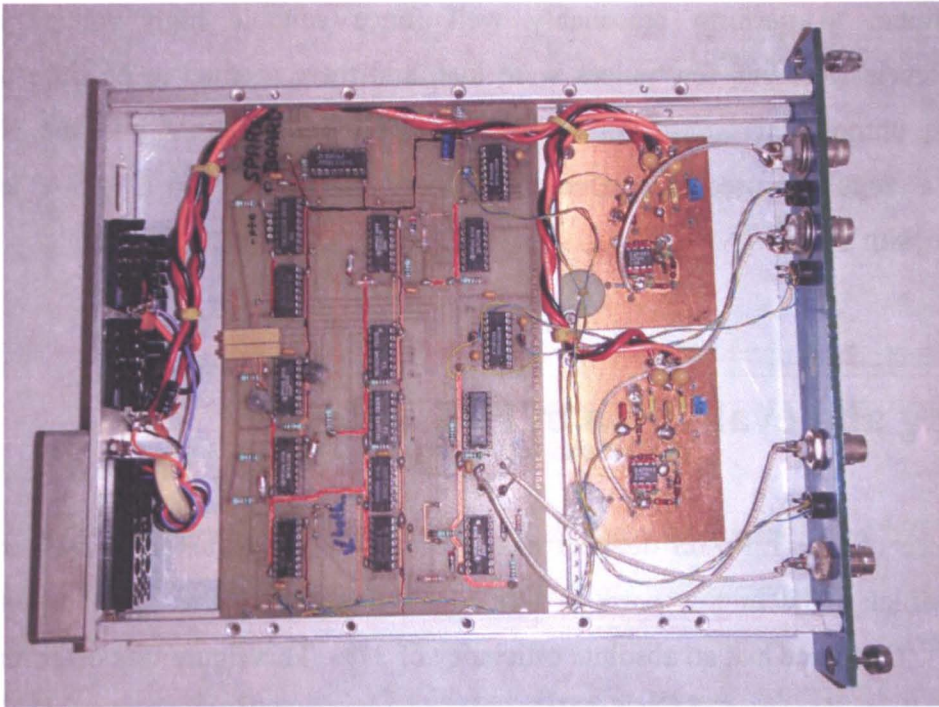


Fig. 2.11: *Modified electronic circuit for pulse discrimination*

The PMT bias arrangements are constructed from discrete components directly soldered onto the pins of the base connector. These circuits have been refurbished with new resistors and capacitors fitted (the high voltage capacitors in particular being prone to aging). The die-cast aluminium boxes that house the PMT bias chains were cleaned and re-painted, and wiring was replaced to bulkhead BNC connectors. This work was necessary as degradation of high voltage components, as well as dirt and contamination, can lead to discharges occurring which in the extreme cases can damage components, and in marginal cases can contribute to dark noise.

Digitization of the PMT signal was originally performed by an Advanced Micro AM686 12ns comparator. As this component is no longer available it was replaced by a pin compatible Linear Technology device – LT1016. This device offered improvements in rise time (10 ns) and immunity to interference. The comparator circuit was originally housed within the detector assembly, close to the PMT. However this made adjustments to the discriminator level (set by a potentiometer) difficult. Also as this threshold level was directly taken from the 5 V power supply it was unduly susceptible to level changes and induced noise. On the refurbished detector the discriminator circuits were relocated in a standard NIM module, alongside the discriminator logic, see Fig. 2.11.

The pulse counting discriminator circuit was constructed from fast TTL logic integrated circuits (ICs). And while several of these ICs are no longer manufactured the circuit was found to perform reasonably well (once suitable high voltage and discriminator levels were set, few pulses were lost, and there seemed to be little over counting). The unmodified circuit was therefore simply incorporated into the NIM module, with a regulator used to convert the NIM +/-12 V supply to a +/-5 V level suitable for use with TTL.

## 2.6 Testing and evaluation of PNL detector

The performance of the  ${}^6\text{LiF:ZnS}$  detector has previously been documented by Barton [17] and McMillan [48]. In this work it was found that a group of eight detectors surrounding a  ${}^{252}\text{Cf}$  source had an absolute efficiency of 37%. This figure was determined from the multiplicity signature of  ${}^{252}\text{Cf}$  which emits on average 3.75 neutrons per fission, and compare very favourably with the typical 50 - 55% efficiency of large  ${}^3\text{He}$  based detectors, which employ as many as 200  ${}^3\text{He}$  tubes, Ensslin [49].

The efficiency of multiple detectors is useful to give an upper limit of sensitivity, but must be regarded with caution, as it will include a significant proportion of neutrons detected after scattering from adjacent detectors. Therefore single detectors perform should be significantly poorer when used in isolation.

Testing a single detector using a  ${}^{252}\text{Cf}$  source of known strength, at a fixed distance, will give a figure for sensitivity. However in a laboratory situation scattered neutrons (particularly from the ground, and nearby walls / buildings) have a significant effect on results, as can be seen by the measurement of count rate against distance, shown in Fig. 2.12.

In free space this measurement would have a  $1/r^2$  relationship. In practice (in this situation at least) the relationship is closer to  $1/r$ . However this measurement is still useful, both as a means for optimising detector performance, and for comparing alternative detector technologies (as long as detectors are positioned consistently, and have a similar geometry). Another useful measure of the effectiveness of the instrument is the consistency of sensitivity down the length of the detector, Fig. 2.13.

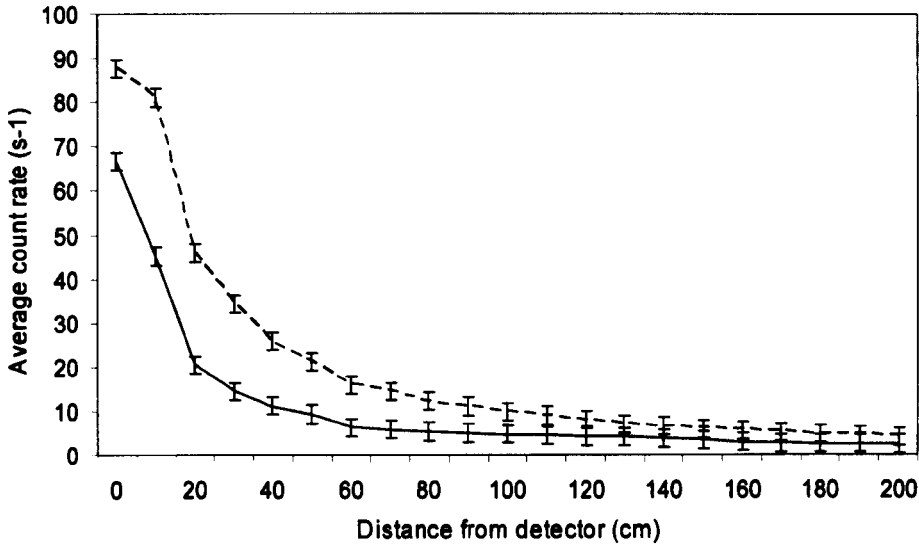


Fig. 2.12: Laboratory testing of a PNL detector (solid line) and <sup>3</sup>He detector (dashed) with a <sup>252</sup>Cf reference source, for bulk count rate with distance.

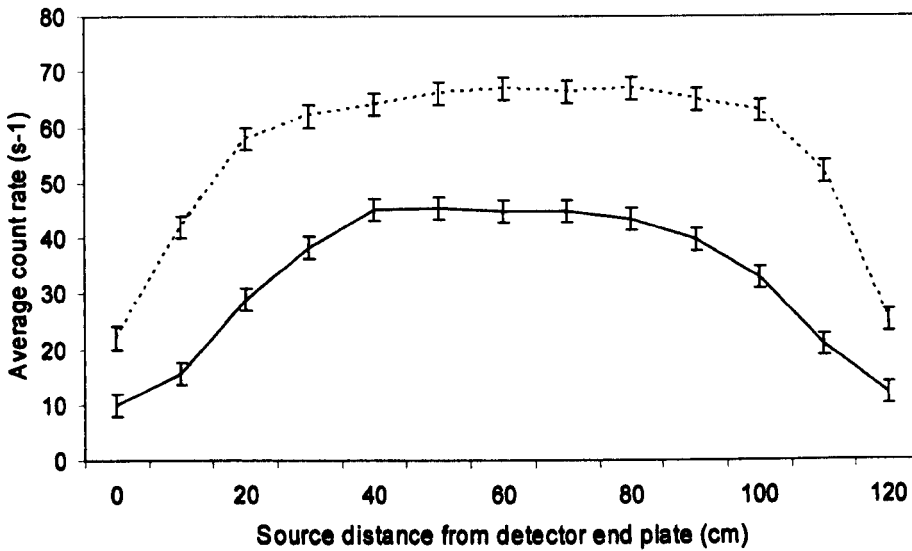


Fig. 2.13: Laboratory testing of a single <sup>6</sup>LiF:ZnS detector (solid line) and <sup>3</sup>He detector (dashed line) with a <sup>252</sup>Cf reference source (23 kBq = 2,600 n.s<sup>-1</sup>), for linearity of performance. Source 10 cm from the face of the detector.

Gamma immunity is an important feature of most neutron detectors, especially for the application under consideration here (see section 1.9). The PNL unit was therefore tested for interference with several gamma sources including: <sup>60</sup>Co and <sup>137</sup>Cs (both in excess of 100 kBq). It was found that even when either source was placed on the surface of the

detector no significant effect was seen, as detailed in Table 2.2. Furthermore the gamma sources had no interfering effect when taking measurement from the  $^{252}\text{Cf}$  reference source. The gamma flux for the largest of these sources, on the detector face, can be approximated as: 50% of  $10^5$  counts per second. This is comparable to the  $10^6$  gamma rejection required by portal specifications.

	$^3\text{He}$ based Detector	Laminar $^6\text{LiF:ZnS}$ detector
Background count ( $\text{s}^{-1}$ )	0.81	0.53
$^{252}\text{Cf}$ ( $5,200 \text{ n.s}^{-1}$ ) - 0.1 m	81.16	45.20
$^{252}\text{Cf}$ - 1 m	9.91	4.73
$^{252}\text{Cf}$ - 2 m	4.19	2.45
$^{60}\text{Co}$ (1 mCi) - 0 m	0.75	0.60
$^{60}\text{Co}$ - 0 m, $^{252}\text{Cf}$ - 1 m	9.82	4.80

Table 2.2: Laboratory testing of benchmark detectors, count rate ( $\text{s}^{-1}$ ) averaged over 300 s.

## 2.7 $^3\text{He}$ proportional counter - benchmark detector

As the de facto standard for thermal neutron detection, gaseous  $^3\text{He}$  tubes represent an ideal bench mark against which to judge the performance of the Laminar  $^6\text{LiF:ZnS}$  detector, and other developments based on this new technology.

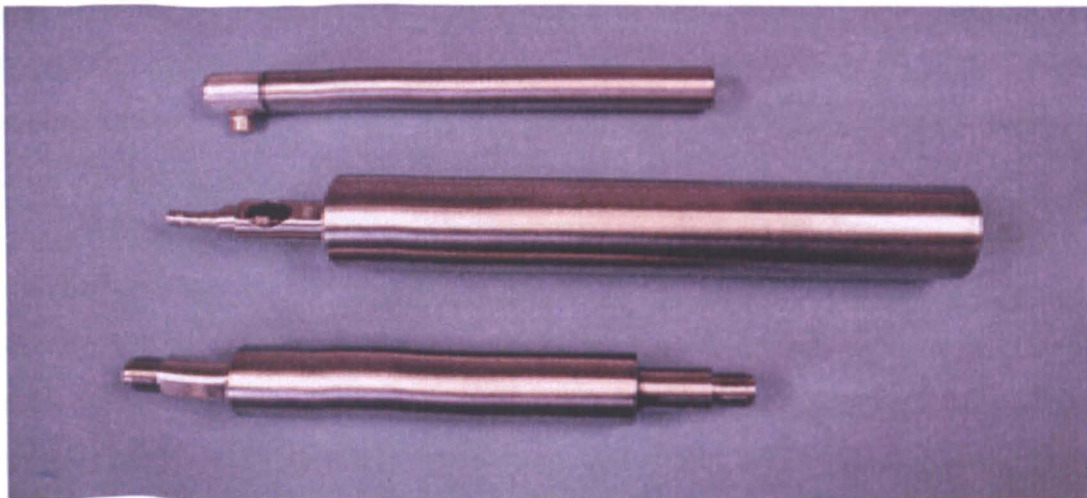


Fig. 2.14:  $^3\text{He}$  Proportional Counters in a range of sizes

<sup>3</sup>He proportional tubes capture incoming neutrons by means of the reaction:



The 764 keV of energy released by the reaction are shared between the proton (573 keV) and the triton (191 keV). In a gas filled tube these charged particles produce an ionizing trail. Freed electrons are then accelerated towards the central anode wire in the tube (typically held at up to 2 kV). The resulting electrical charge collected by the anode is readily detectable, and can be distinguished from electrical noise (and most gamma interference) by means of simple pulse height discrimination. With a capture cross section of 5330 b to thermal neutrons (0.025 eV), these detectors can be highly efficient even with only a small amount of <sup>3</sup>He present (1-2 g in a standard tube). At 4 atmospheres pressure intrinsic sensitivity to thermal neutrons is typically 70 – 80% [19]. While this sensitivity figure can theoretically reach almost 100% through increased pressure, the cost of achieving this in terms of gas and containment are uneconomical. Furthermore at high pressures the ionization products are liable to re-absorption, reducing the charge reaching the detector anode, and thus effecting sensitivity.

While several manufacturers of tubes exist, their products are broadly similar. Subtle variations to quenching gas composition (typically CO<sub>2</sub> or Krypton used to reduce wall effects) and anode wire tension and thickness (adjusted to improve robustness) have only minor impact on the sensitivity, when compared to the critical parameters of volume, diameter and fill pressure. It is therefore relatively straightforward to make comparisons of thermal neutron detectors against a ‘Standard’ <sup>3</sup>He proportional counter.

However in applications involving higher energy neutrons, a large volume of moderating material is required, to slow the neutrons down in energy to the sensitive region of the detectors (Table 1.8 and 1.9). The geometry and thickness of moderator material is selected for a specific application to optimize sensitivity to the energy range of incoming neutrons. In the case of Security portals this is not a trivial task due to the potentially broad energy range of neutrons involved (Chapter 1).

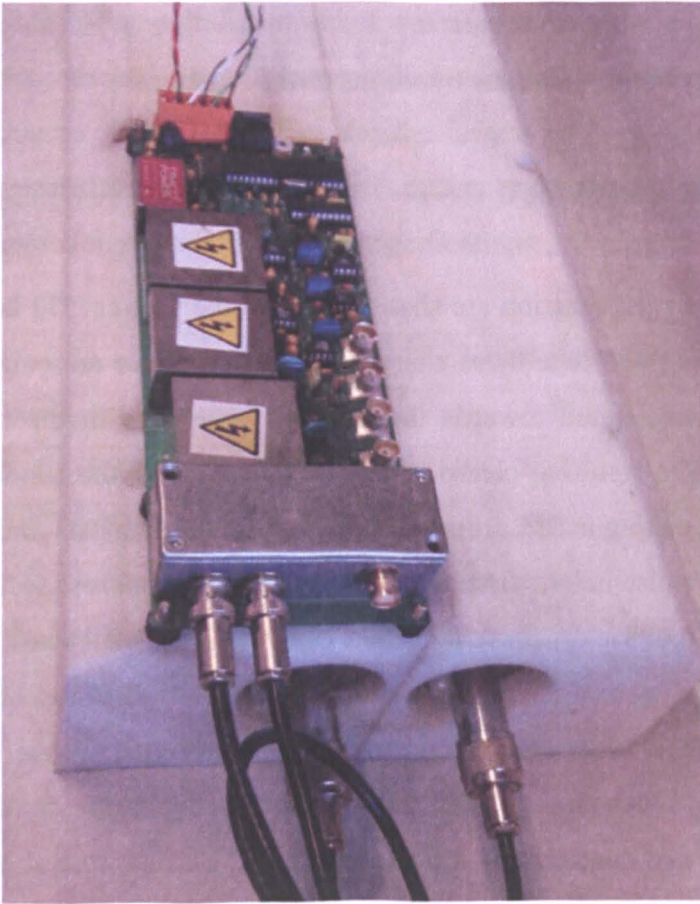


Fig. 2.15:  $^3\text{He}$  based detector used for bench mark testing

The detector used for bench mark testing was supplied by Tata Steel. As a standard system used for security applications, Fig. 2.15, it incorporates two  $^3\text{He}$  tubes manufactured by Saint Gobain. Each tube has an active volume of 50 mm diameter by 1000 mm long and a fill pressure of 4 atmosphere. This combination provides optimum sensitivity to thermal neutrons. High voltage power supplies and amplification / discrimination / pulse counting electronics are integrated into a custom made circuit mounted on top of the detector. The assembly has a minimum of 30 mm of polyethylene moderator all around the detector tubes, with more moderator on the surface furthest away from the target source. The moderator design is based on empirical calculations [19,30] and assumptions about typical target neutron energy, and as such could potentially be improved through Monte Carlo analysis (see Chapter 3). Nevertheless this arrangement of tubes and moderator is typical of security portal assemblies (although longer 1.5 m tubes are also often used), and has been proved to perform well in field trials with  $^{252}\text{Cf}$  sources.

Results for a number of detectors, provided by Tata Steel, are given in table 2.3. These were tested with a 3.07  $\mu\text{Ci}$  source at a distance of 2 m.

	Det1.1	Det1.2	Det2.1	Det2.2	Det3.1	Det3.3	Det4.1	Det4.2	Avg
<b>Position (m above grnd)</b>	2	2	1	1	2	2	1	1	
<b><math>^{252}\text{Cf}</math> source</b>	5.4	5.4	6.5	7.2	5.3	5.7	6.0	6.3	6.0
<b>Counts/ <math>\mu\text{Ci}</math></b>	1.7	1.8	2.1	2.3	1.7	1.8	2.0	2.1	1.9
<b>Background</b>	0.74	0.816	0.912	.792	0.748	0.632	0.728	0.732	0.775

Table 2.3: Sensitivity measurement (counts per s) for 1 m x 50 mm  $^3\text{He}$  based detectors in field testing on open air test site (figures with source present have background subtracted).

Calculation of the neutron flux produced by this source is;

Source strength 3.07  $\mu\text{Ci}$  = 113.6 kBq

For  $^{252}\text{Cf}$  only 3.1% of decays are fission events [50].

On average each fission has a multiplicity of 3.7 [51].

$$113.6 \times 10^3 \times 0.031 \times 3.7 = 13,028 \text{ neutrons/s}$$

$$\text{At 2m, neutron flux is : } \frac{13,028}{4 \times \pi \times 200^2} = 0.026 \text{ n.s}^{-1}\text{cm}^{-2}$$

For a detector measuring 100 cm x 25 cm the total flux at the surface is therefore:

$$2,500 \times 0.026 = 64.9 \text{ n.s}^{-1}$$

The measured value of 6.0  $\text{n.s}^{-1}$  average therefore represents 9.2% intrinsic efficiency. This is consistent with the results reported by Brenizer [38]. It is interesting to note the difference in values between detectors positioned 1m above ground, and those 2 m above ground. This effect is due to neutrons 'reflected' by moderating material in the ground layer.

The  $^3\text{He}$  detector was set up in the laboratory and assessed for correct operation. HT voltage was selected as the mid range from the manufactures data sheet (1250 V). Pulses generated by the pre-amp and shaping amps from both tubes were monitored on an oscilloscope, to check for shape and consistency. The output logic level signals from the discriminator were fed into a timer counter. With a  $^{252}\text{Cf}$  source close to the detector, the threshold level was gradually increased in 100 mV steps. The pulse height distribution, shown in Fig. 2.16 has the two distinct peaks typical of these devices, corresponding to wall effect (small peak) and main signal (large peak) [20]. A suitable operating threshold, between the noise level and neutron roll off, was selected at 150 mV.

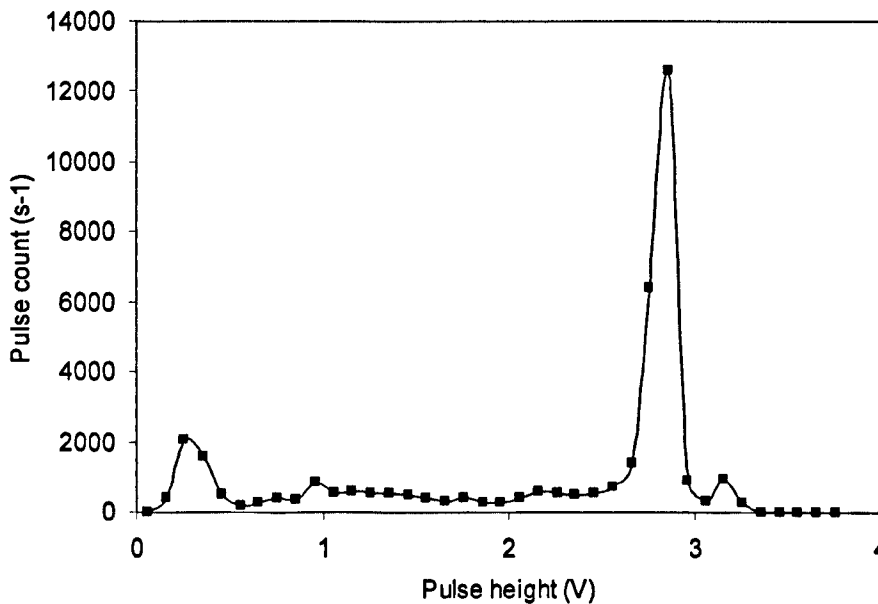


Fig. 2.16:  $^3\text{He}$  Pulse Height Distribution(50 mm tube- 1250 V bias, 150 mV threshold)

Results of count rate against distance for the  $^3\text{He}$  detector are given in Fig. 2.12 and 2.13 along side those for the  $^6\text{LiF:ZnS}$  laminar detector. In order to maintain consistency both measurement were made in the same location in the laboratory. As can be seen from the results these units give a broadly similar performance, with the  $^3\text{He}$  detectors out performing the PNL detector by approximately 20 - 30%.

Gamma immunity measurements were made for the  $^3\text{He}$  detectors, as in section 2.5. As with the PNL detector no gamma effect could be observed with the sources available.

## **2.8 Conclusions**

From this work we are now in the position of having two working neutron detectors suitable for use with the broad energy spectrum produced by fission sources. Both units have been tested and found to offer similar sensitivity, comparable to detectors tested elsewhere. Furthermore both systems were found to be largely immune to gamma interference. As such they offer an excellent bench mark against which further developments can be judged.

# Chapter 3

## Monte Carlo analysis

### 3.1 Introduction

While laboratory and field testing is invaluable in assessing detector performance, all testing has limitations; in terms of accuracy and repeatability, as well as the time constraints, where for statistical accuracy each reading requires data to be collected over several minutes if not hours. Furthermore testing can clearly only be carried out once a physical detector has been released. Therefore a programme of detector modelling was undertaken, in parallel with the laboratory work. The aims of the modelling were to further characterise and optimize bench mark  $^6\text{LiF}$  and  $^3\text{He}$  detectors, extrapolate test data used in the development of the new detector, and evaluate new detector designs prior to the manufacturing stage.

### 3.2 MCNP

MCNP is a general purpose Monte Carlo N-Particle transport code, developed over many years by Los Alamos National Laboratory [25]. The application is well maintained with the release of MCNPX offering extended energy ranges and particle types. It is the industry standard code for analyzing the transport of fission and fusion neutrons by the *Monte Carlo* method. The code deals with transport of neutrons, gamma rays, and coupled transport, i.e., transport of secondary gamma rays resulting from neutron interactions. The MCNP code can also treat the transport of electrons, both primary source electrons and secondary electrons created in gamma-ray interactions. Although for simple problems MCNP runs quickly on modern PCs ( $10^6$  particles in under 2 mins) it is

also capable of using numerous variance reduction techniques to reduce processing time and improve accuracy, particularly useful in deep shielding and criticality calculations.

As processing power is not a serious constraint for the relatively simple models employed here only the simplest variance reduction techniques have been employed for example; particles are destroyed beyond a certain radius of the detector and for some models unidirectional sources are used.

A number of thoroughly verified nuclear cross section libraries are available with MCNP covering most isotopes. The library *endf66* derived from the ENDF/B-VI evaluated nuclear data files, was used for most of the analyses carried out here [31].

### 3.2.1 MCNP input cards

MCNP is very well documented, with an extensive user manual [25] and numerous tutorials / primers available. It is available as an executable and requires only a single text input file, the lines of which are historically referred to as “cards”. The input cards contain the following information:

- *Surfaces*; planes spheres, cones etc
- *Cells*; defined by combining *Surfaces*, and containing a *Material*
- *Materials*; elemental or isotopic composition
- *Source* ; point or distributed sources
- *Tallies* ; output tallies and tables to be generated
- *Particles* ; number of starting particles

Once a basic model has been constructed for a particular problem it is straight forward to make minor adjustments in order for example to optimise geometry. For this project this method was applied to both a standard  $^3\text{He}$  based detector and the PNL Laminar detector.

### 3.2.2 Output tables, tallies and images

Whiles MCNPX can generate a wide range of output data; typically in the form of tables, it is not equipped with a sophisticated graphics interface. In order to verify model geometry and to visualise neutron interactions the Sabrina software package was used.

Developed by K. Van Ripper at Los Alamos Laboratories [52], Sabrina allows visualisation of both models and particle tracks generated by MCNP. Several of the images shown later in this report were produced using Sabrina.

### 3.3 $^3\text{He}$ detector benchmarking

Two MCNP models were constructed incorporating the large  $^3\text{He}$  based neutron detector, supplied by Tata Steel. The first model had the detector positioned in a simplified laboratory space, approximating the conditions used for benchmark testing. A comparison of modelled performance against the lab test results is shown in Table 3.1. For the source at 1m and 2m the results broadly tally, with lab results showing approximately 15% less counts. It is believed that this is primarily due to losses in the detector e.g. wall effect producing pulses too small to register. The strong disparity at 0.1 m is due to an excessive dead time in the detector (introduced to reduce background from cosmic ray neutrons).

	MCNPX Data ( $\text{s}^{-1}$ )	Lab Results ( $\text{s}^{-1}$ )
$^{252}\text{Cf}$ - 0.1 m	165.05	91.16
$^{252}\text{Cf}$ - 1 m	11.31	9.91
$^{252}\text{Cf}$ - 2 m	4.95	4.19

Table 3.1: Comparison of MCNP data with lab results  $^{252}\text{Cf}$  source – 5,200  $\text{n.s}^{-1}$

The second model positioned the detector in an outdoor test site, raised above the ground on a steel stanchion. Generic composition of materials such as earth and concrete, used in this model, were taken from Williams [54]. While the mineral composition of these complex materials will vary widely from place to place, the relatively small neutron cross section of these elements will minimize this impact. MCNP cards for these models can be found in appendix A.

The test site model was verified against experimental results for a number of detectors. Field testing was carried out using a 3  $\mu\text{Ci}$   $^{252}\text{Cf}$  source ( $\sim 13700 \text{ n.s}^{-1}$ ) at a distance of 2 m from the face of the detector, exposed for 10 minutes. The MCNP model used an isotropic  $^{252}\text{Cf}$  point source mapped for  $10^7$  disintegrations. Results are shown in

Table 3.2. Discrepancies of approximately 20% between the modelled and test results are believed to be due to the following factors:

- For simplicity a very thick concrete ground plane was assumed, this is unlikely to be accurate. To determine the actual ground composition (including water content) at the Redeem test site would require excavation, survey and soil analysis beyond the scope of this project.
- In the model it is assumed that detectors perform ideally. In reality not all captured neutrons result in detection, due to wall effects etc. a proportion of neutrons will not generate a sufficient pulse in the anode to exceed the discriminator threshold. This effect is difficult to quantify as it depends on the internal geometry of the tube, operating voltage, gas composition etc.
- Statistical uncertainty; for the relatively small numbers of incidents modelled, on a Poisson distribution a 3 standard deviation error equates to approximately  $\pm 0.15$  cps.

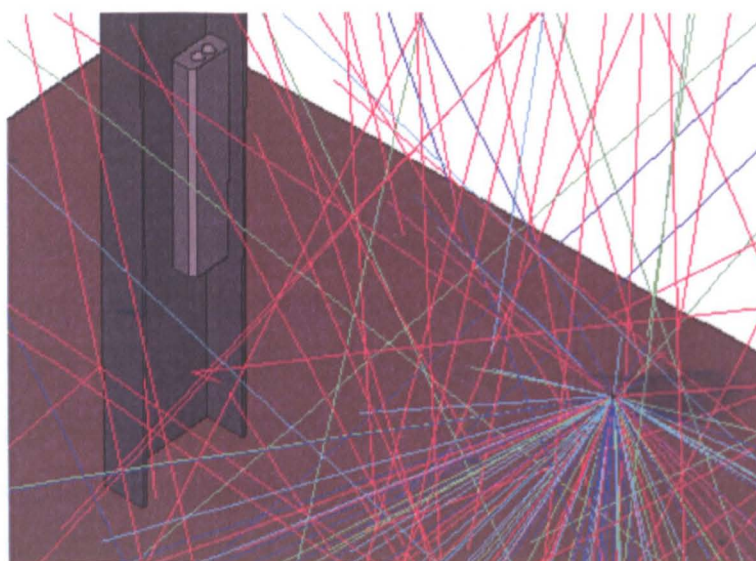


Fig. 3.1: MCNP / Sabrina output (only neutrons interacting with the ground are shown). Track colour represents neutron energy from thermal (red) to fast (blue).

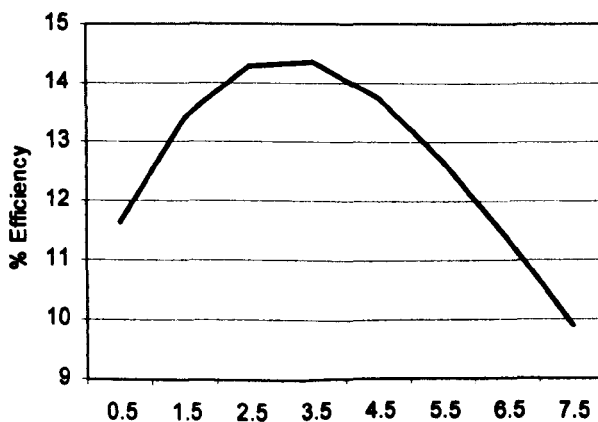
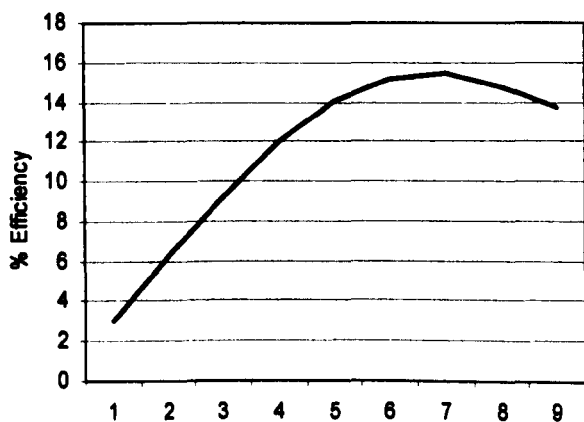
	Counts (s <sup>-1</sup> )	Counts (s <sup>-1</sup> )
<b>Panel position</b>	3 m above ground	1m above ground
<b>Detector 1</b>	5.5	6.5
<b>Detector 2</b>	5.4	7.2
<b>Detector 3</b>	5.3	6.0
<b>Detector 4</b>	5.7	6.3
<b>Panel Average</b>	<b>5.5</b>	<b>6.5</b>
<b>MCNP Model</b>	<b>6.7</b>	<b>7.8</b>

Table 3.2: Comparison of MCNP data with results from Redeem test site <sup>252</sup>Cf source ~13700 neutrons per sec.

Under these circumstances it is felt that the test results are close enough to validate the model for the purpose of this investigation.

### 3.4 <sup>3</sup>He Detector Optimization

Once the basic detector model was developed variations were made to key parameters such as number of tubes and moderator thickness, in order to determine the optimum theoretical performance which could be achieved. To maintain consistency of results the overall height and width of the detector were kept constant at 1000 mm and 50 mm respectively. To speed up modelling time, and improve accuracy of results, a distributed planar source was defined, to irradiate the front face of the detector only. While this is a departure from “real world” conditions it is felt to be a reasonable compromise for a comparative study of this type. Results form these models are summarised in Fig. 3.2-3.5.



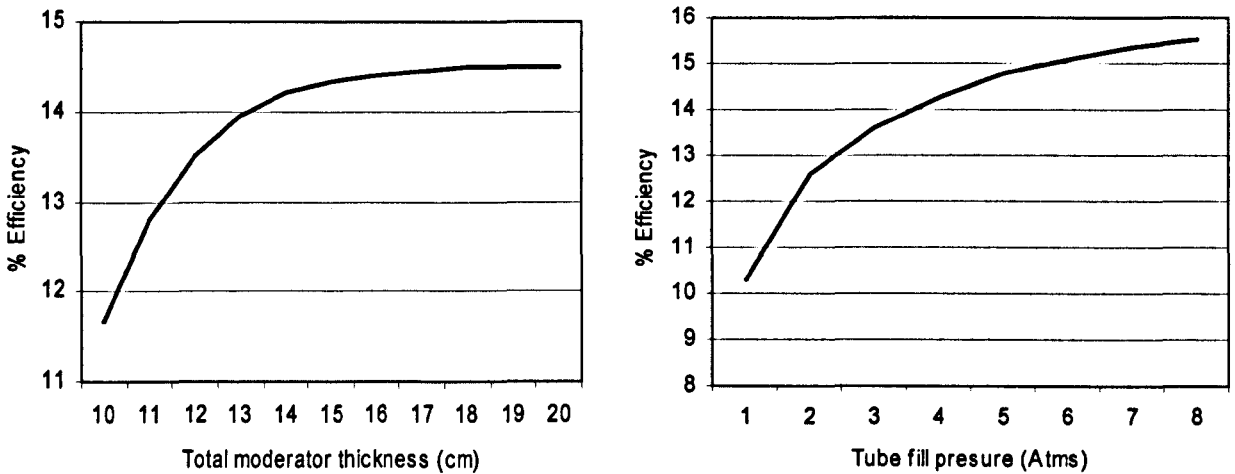


Fig. 3.2 – 3.5: MCNP  $^3\text{He}$  detector optimisation; intrinsic efficiency calculated for key detector parameters

The optimum number of 50 mm diameter tubes in a detector of this size was found to be 7 however the diminishing returns achieved above 4 tubes precludes their use on cost grounds, in any application where size is not severely limited. A similar comment could be made for fill pressure, which can not be economically justified above 5 atmospheres. Efficiency plateaus for moderator thickness above 15 cm, whilst the thickness of moderator in front of the detector tubes (i.e. between the source and the  $^3\text{He}$  detectors) peaks at 3 cm. The optimised  $^3\text{He}$  detector was therefore found to have the following parameters;

- Four  $^3\text{He}$  tubes measuring 50 mm diameter x 1000 mm length fill pressure 5 atms.
- Polyethylene moderator dimensions 500 mm x 1000 m x 180 mm.

The efficiency achieved here peaked at 14.8%. Although this is a significant improvement over the <10% previously seen for this type of detectors, due to the extra tubes required it comes at a high cost (i.e. approximately 50% increase in performance for 100% increase in cost). If space is not an issue it would clearly be more sensible to simply use two lower sensitivity detectors.

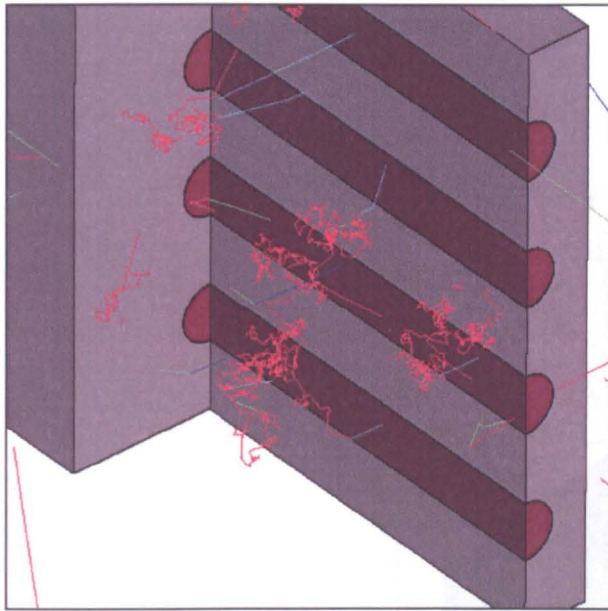


Fig. 3.6: MCNP / Sabrina output  $^3\text{He}$  detector (cross section extracted for analysis)

A cross section of a typical  $^3\text{He}$  based detector, with a number of neutron tracks, is shown in Fig. 3.6. An interesting point to note from this figure is the relatively long staggered path lengths experienced by the fully thermalized neutrons shown in red. The capture cross section (on thermal neutrons) for hydrogen is 0.294 b [134]. Using equation [2.1] for polyethylene (density; 0.95, atomic mass; 13) and without taking into account elastic scattering this would equate to a thermal neutron attenuation length of 53.6 cm. As hydrogen has a thermal elastic scattering cross section of 45.3 b, it can similarly be calculated that scattering will occur every 3.5 mm. Although this means that on average 153 scattering interactions will occur before a thermal neutron is absorbed by the moderator, with a thickness of at least 60 mm between the tubes, for the  $^3\text{He}$  based detector pictured in Fig. 3.6, a significant proportion of neutrons will be lost to capture reactions in the hydrogen. For the detector modelled in Fig 3.6 it was found that 34.4% of neutrons entering the detector assembly were absorbed by the moderator, compared to 14.8% captured in the  $^3\text{He}$ . A more widespread distribution of the detecting elements within the assembly could therefore significantly improve sensitivity.

Through modelling of the PNL detector, it has been found that systems with layered capture agent (and scintillator) can greatly reduce the moderator losses, as shown in the following section.

### 3.5 ${}^6\text{LiF}/\text{ZnS}$ detector

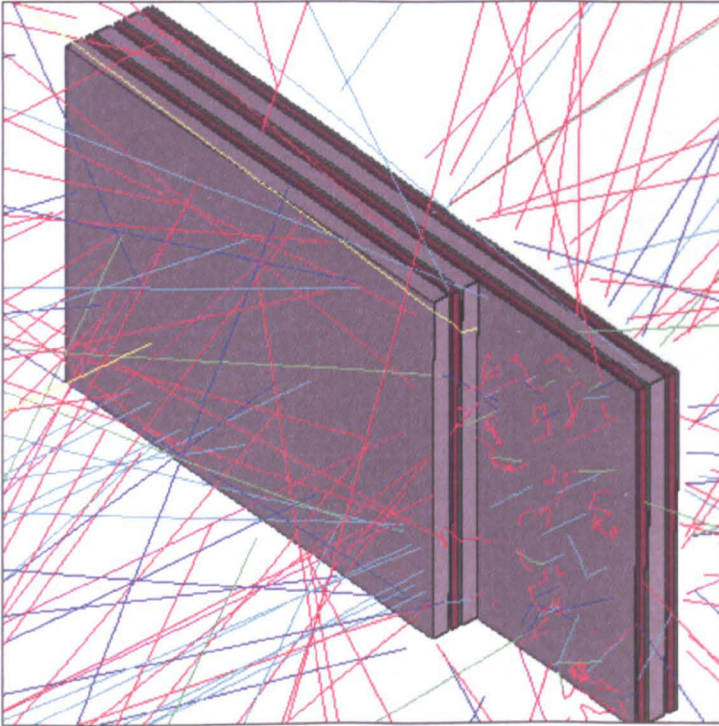


Fig. 3.7: MCNP / Sabrina output  ${}^6\text{LiF}/\text{ZnS}$  detector (cross section removed for analysis)

Composite thermal neutron detectors employing  ${}^6\text{LiF}$  and ZnS have been studied in some depth, experimentally [40,42,48,49,53] and with Monte Carlo modelling [37]. However these efforts have largely focussed on optimisation of the microscopic performance of the detector, i.e. in converting thermal neutrons into light. Integrating the thermal neutron detecting layers into a large device with sensitivity to a broad neutron energy range is not nearly so well understood. In particular key parameters, including the amount and distribution of coating material and moderator, need to be evaluated.

In order to develop a realistic target specification and to start the process of optimising the laminar detector design, the existing PNL detector was modelled, see appendix B. Additionally a series of modified designs were modelled in an attempt to estimate the optimum achievable performance for a detector of this type. A set of comparative results were produced for detectors with the same footprint as the  ${}^3\text{He}$  detectors above, i.e. 1000 x 500 mm.

Parameters studied included; moderator thickness, thickness of the capture / scintillator layer, and detector width.

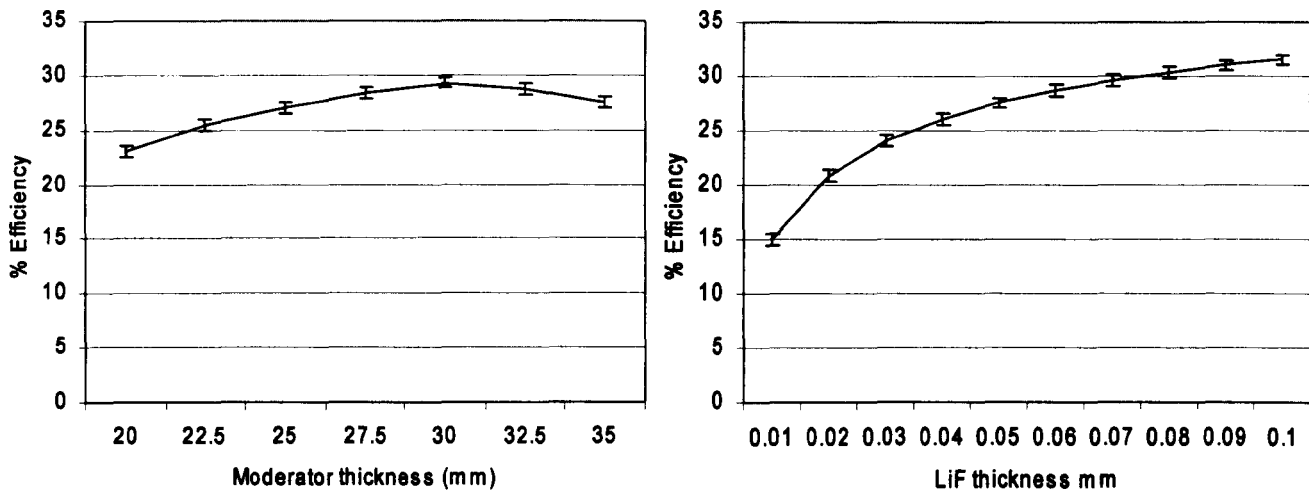


Fig. 3.8 a,b: MCNP <sup>6</sup>LiF detector optimisation; intrinsic efficiency calculated for key detector parameters (a-moderator thickness, b-LiF thickness)

The optimum capture efficiency for the modelled PNL detector was 18.8% for fission neutrons. The optimum achieved for 8 layers of <sup>6</sup>LiF/ZnS, with 3 x 3 cm moderator layers was 38.7%.

Examination of the results from the modelled 8 layer detector suggested that a similar level of performance could be achieved with fewer layers of <sup>6</sup>LiF/ZnS, Fig 3.9 shows 30% of the total efficiency coming from layers 2 to 5, with layers 1 and 8 contributing only 2%. This is particularly important for optimisation of cost against performance.

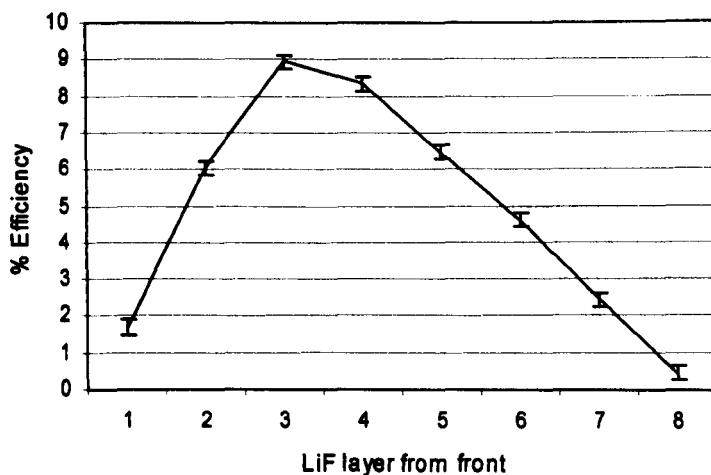


Fig. 3.9: MCNP  ${}^6\text{LiF}$  detector optimisation; intrinsic efficiency contribution from individual layers of capture / scintillator.

The use of asymmetric moderator layout was also investigated. The most efficient of these combinations was found by increasing thickness with depth from the front face of the detector i.e. 2 cm, 4 cm, and 6 cm layers. An efficiency of 31.53% was achieved using this moderator layout with only 4 scintillator layers. An added benefit from this approach is a degree of directionality, with the thicker back layers effectively screening the detector from lower energy neutrons from this direction. This could potentially reduce background sensitivity and susceptibility to false triggering in portal systems.

Interesting results were found from an assesment of detector efficiency against overall size. By maintaining a constant neutron flux to the detector surface it was possible to gradually increase the width of the detector whilst maintaining a constant  $\text{n.cm}^{-2}$  flux. It can be seen from Fig 3.10 that benefits can be gained, beyond the obvious linear size to sensitivity relationship by employing detectors with a width of 50 cm or more. This is undoubtedly due to partially moderated neutrons 'leaking' from the sides of the detector, an effect more prevalent in smaller detectors where the surface area to volume is greatest.

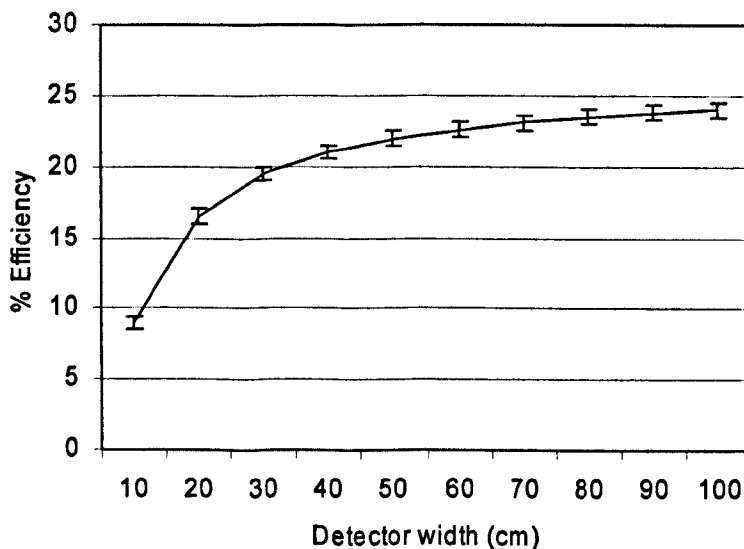


Fig. 3.10: MCNP  ${}^6\text{LiF}$  detector optimisation; efficiency variation with width for a constant flux neutron field.

### 3.6 BN detector

Enquiries into the cost and availability of  ${}^6\text{LiF}$  have led to some concern over its continued suitability for use in very large detectors, as discussed in Chapter 2. Investigations have been expanded therefore, to evaluate the effectiveness of low cost boron compounds as an alternative capture agent to  ${}^6\text{Li}$ . To get the greatest cost benefit, this in particular requires boron to be employed in its naturally occurring isotopic mix (19.8%  ${}^{10}\text{B}$  [57]). Boron Nitride ( ${}^{10}\text{BN}$ ) and ZnS have been reported as an effective combination (Chapter 4) for thin film detectors in a weight ratio of 1:4. As the relative densities of ZnS and BN are  $4.0\text{ gcm}^{-3}$  and  $1.9\text{ gcm}^{-3}$  this equates to an atomic ratio of 1:2. The formula for the capture / scintillation layers applied to MCNP was therefore taken as follows;



The overall mass density applied for the layer was  $3.58\text{ gcm}^{-3}$ . At this stage no binding material was included in the model, as this was intended to be a minor constituent, containing compounds with relatively low neutron cross section.

Initially the MCNP model produced for the  ${}^6\text{LiF}:\text{ZnS}$  was modified with the above BN:ZnS mixture. The results for neutron captures gave an efficiency of 15.3%, a slight reduction on the performance to the  ${}^6\text{Li}$  detector (in line with combination of cross section and isotopic composition). The effect of capture layer thickness was also modelled, with results given in Fig. 3.11.

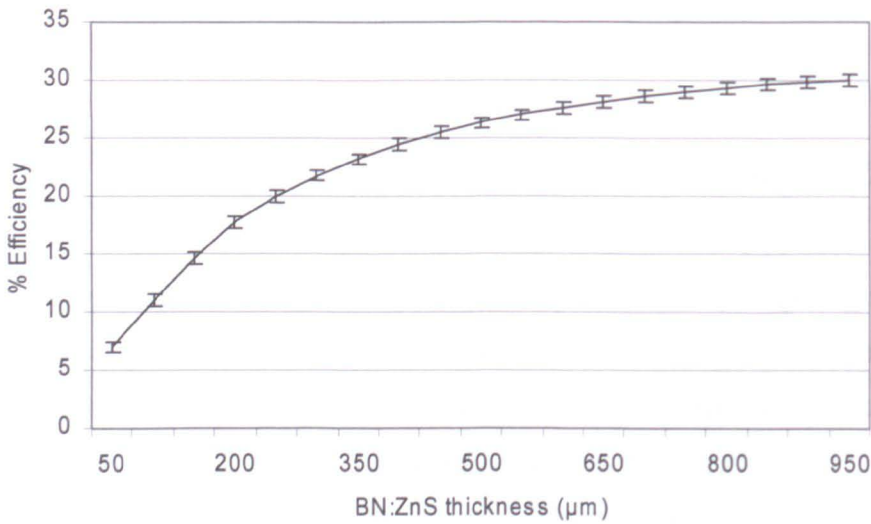


Fig. 3.11: *Effect of boron capture layer thickness on intrinsic efficiency*

From this it can be seen that to achieve optimum performance, in this configuration, a layer thickness of up to 1 mm is required. Experimental work (Chapter 2 and 4) suggests this thickness is significantly greater than practical, due to light lost in the opaque mixture. An 18% efficiency for a 200 µm seems to be a realistic target however.

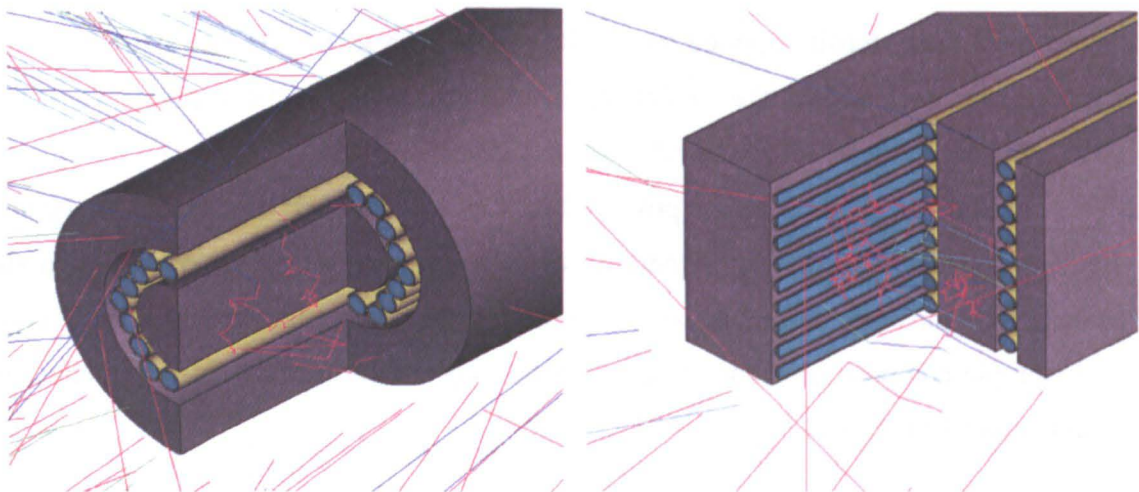


Fig. 3.12: *Cutaway ray traces of rod based detector models*

Alternative detector geometries have also been assessed, which could allow better distribution of capture material within the matrix, hence improving sensitivity without greatly increasing layer thickness, see Fig. 3.12. In particular a number of designs of rod based detectors have been simulated. The latter of these designs employing a matrix of

rods, surrounded by thin BN:ZnS tubes, seems to offer a potential improvement in sensitivity over the laminar construction; as shown in Table 3.3.

<b>Light Guide Arrangement</b>	<b>Moderator comments</b>	<b>Surface area capture/scintillator</b>	<b>Efficiency</b>
3 x linear plates	4 x 2 cm sheets	9000 cm <sup>2</sup>	16.4%
21 x 1 cm rods	4 x 2 cm sheets	1320 cm <sup>2</sup>	21%
21 x 1 cm rods	As above +2 cm on rear face	1320 cm <sup>2</sup>	23%
21 x 1 cm rods	Solid block drilled for guides	1320 cm <sup>2</sup>	29%

Table 3.3: *Relative efficiency of alternative detector geometries*

While the above figures are encouraging, the MCNP model does not include a treatment of the scintillation process or the transmission of light produced. While other codes permit optical simulation, such analyses are heavily dependent on precise knowledge of optical parameters and surface conditions within the materials. For the complex composite materials in use here these parameters would be very difficult to quantify. An experimental approach to assessing film samples and light guides is therefore preferred to determine comparative performance of the various combinations of coatings and light guides. Furthermore, factors such as availability of materials e.g. wavelength shifting acrylic in rod form, and realistic manufacturing techniques must be considered, if alternative designs are to be realised.

### 3.7 Sample testing assembly

In order to assess scintillation / capture compounds and light guides a small scale test rig was constructed employing a small wavelength shifting light guide; an MCNPX model of this assembly is shown in Fig. 3.13. The test rig employed a large amount of moderator to improve thermalization of the source which was housed close to the light guide.

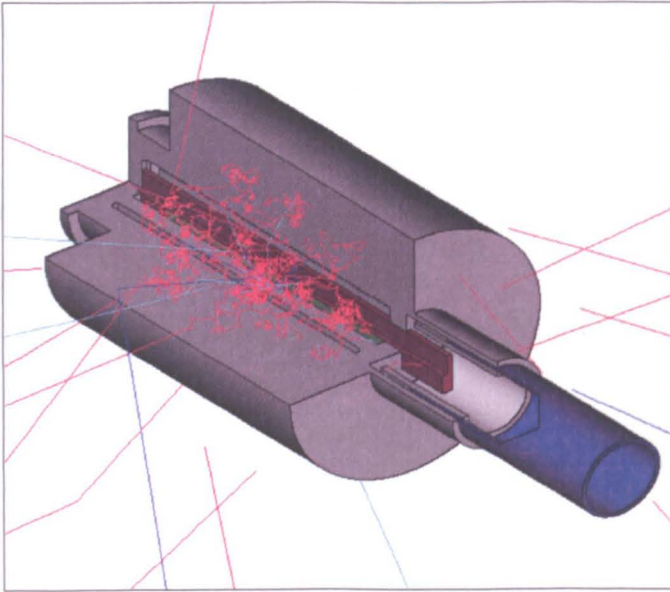


Fig. 3.13: *Cutaway ray traces of small light guide model*

The model was used to build confidence in the results generated by the test rig, and to extrapolate results beyond the available test samples. MCNP data for this model are tabulated along side lab test results in Chapter 4.

### 3.8 Conclusions

Through assessment of Monte Carlo models it has been possible to optimise theoretical performance both of the  ${}^6\text{LiF:ZnS}$  detector (developed by Barton et al) and  ${}^3\text{He}$  proportional counter systems supplied by Tata Steel. This work has provided a better understanding of the neutron capture mechanisms within the detectors, and has led to a preliminary design of a scintillation detector employing non-isotopically enriched boron in place of  ${}^6\text{Li}$ . Due to the reduced effectiveness of boron in this form (compared to  ${}^6\text{Li}$ ) it is important to maximise light generation and coupling, discussed in Chapter 4, and signal processing; Chapter 5.

# Chapter 4

## Material selection for boron based detectors

### 4.1 Introduction

Large area thermal neutron detectors employing  ${}^6\text{Li}:\text{ZnS}$  have been found to be well suited to low background, low count rate applications [48], and as such are an ideal candidate for replacement of  ${}^3\text{He}$  proportional counters in portal monitors (as well as many other industrial and scientific applications). However the cost and availability of  ${}^6\text{Li}$  for use in these detectors is prohibitive. It is believed that  ${}^{10}\text{B}$  can provide an alternative cost effective solution, particularly if it can be used in its naturally occurring ratio with  ${}^{11}\text{B}$  (19.9%  ${}^{10}\text{B}$ , 80.1%  ${}^{11}\text{B}$ ). Monte Carlo modelling has confirmed that this is potentially feasible. The development of a new detector requires the selection of suitable boron compounds, as well as associated scintillating material, binders and wavelength shifting light guides. This chapter details the background research and laboratory studies undertaken in the selection of these materials.

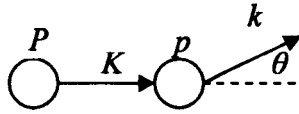
## 4.2 Selection of neutron capture and scintillating compounds

Although neutrons have no electrical charge and therefore no primary ionising effects on matter, their interactions are capable of releasing energetic charged particles, which in turn can be converted into a useful, measurable, electrical signal. This process clearly requires at least two stages. In the first stage a charged particle is produced through interaction with the absorber material. This can be achieved by two means: either an elastic collision, in which kinetic energy from the neutron is passed to the interacting nucleus which recoils producing an ionising trail, or alternatively a neutron capture reaction can take place; for several isotopes this results in the spontaneous fission of the target nucleus, and the useful emission of several energetic charged particles and gamma rays. In the second stage of the process the charged particles (or gamma rays) generated by the neutron interactions are either directly converted to an electrical signal, by some form of ion multiplication (e.g. acceleration through an electric field), or they interact with a scintillating compound to produce light, which is in turn readily interpreted by a photo detector such as a photomultiplier tube.

While new solid state [55] and ionising [56] techniques are being developed for neutron detection it seems these methods are at present only suited to relatively small detectors, and therefore do not offer the gross sensitivity required by this project. The decision was therefore made in the early stages of the work to base the detector on an optimized combination of neutron capture and scintillation materials, as discussed in Chapter 2 and 3.

### 4.2.1. Neutron interactions - Recoil

Neutron recoil, often referred to as an (n,n) reaction, typically involves light atoms such as hydrogen, which with a single proton, have a mass very similar to that of a neutron. By conservation of momentum equation [4.1], where  $\theta$  = angle of divergence,  $P$  and  $p$  are particle atomic masses; it can be seen that a neutron can transfer almost all its kinetic energy ( $K$  and  $k$ ) to the proton in a single collision; i.e. if  $\theta = 0$  and  $P = p$ .



$$\frac{k}{K} = \text{Cos}(\theta) 4 \frac{Pp}{(P+p)^2} \quad [4.1]$$

The average proportion of energy transferred from a neutron during such elastic collisions  $\xi$  is given by [4.2].

$$\xi = \frac{2p}{(p+1)^2} \quad [4.2]$$

For elastic interactions with a hydrogen nucleus, therefore typically 50% of energy is transferred.

In order to pass on sufficient energy to the scintillator this reaction clearly requires fast incoming neutron (energy >1 MeV). At these energies the cross section for hydrogen is less than 5 barns. The microscopic cross section  $\sigma_R$  can be converted to a macroscopic inverse attenuation length  $\Sigma_R$  (with units  $\text{cm}^{-1}$ ) using formula [4.3].

$$\Sigma_R = \frac{\sigma_R}{1 \times 10^{24}} \times \frac{N_a d}{M} \quad [4.3]$$

Where  $d$  is density,  $M$  is gram atomic weight of the isotope, and  $N_a$  is Avogadro's number.

For a typical polymer hydrocarbon, H will be present in a proportion of less than 50%, with a typical mass density of  $1 \text{ g/cm}^3$ . The macroscopic inverse attenuation length for fast neutrons is therefore;

$$\Sigma_R = \frac{0.5 \times 6.022 \times 10^{23} \times 5}{1 \times 10^{24} \times 1.008} = 1.49 \text{ cm}^{-1} \quad [4.4]$$

The proportion of neutrons captured  $Q$ , in a layer of thickness  $T$  is given by [4.5]

$$Q = 1 - e^{-\Sigma_R T} \tag{4.5}$$

From this is can be calculated that for a 50% probability of interaction a detector requires a 0.47 cm layer of hydrocarbon, in addition to the scintillation material.

As the path length for the recoil protons is of the order of only a few microns it requires a large amount of scintillating material interspaced with hydrogen to achieve a significant sensitivity; as is the case with liquid scintillators such as NE213. Maintaining good gamma immunity with this type of detector is extremely problematic. Therefore although this interaction is an interesting prospect for small fast neutron detectors, it is inappropriate for a large high efficiency detector under development in this project.

## 4.2.2 Neutron interactions - Capture

Although many elements interact with, and capture neutrons, the majority of these undergo some form of activation, whereby a new isotope is temporarily created, which decays emitting charged particles, and gamma rays ( $\gamma$ ) which can in turn be detected. The activated isotopes are however generally stable for a relatively long period, raging from seconds to hours. Silver is a good example of a useful activation detector element. Its two naturally occurring isotopes have the properties listed in table 4.1. While the high thermal neutron cross section and useful beta particle energy make it an interesting candidate for use in detectors, its delayed emission (140 s half life) mean it is inappropriate for applications requiring a real-time measurement.

Isotope	Abundance	Induced Activity	Half life	Thermal Cross section
$^{107}\text{Ag} (n, \gamma)$	51.8%	1.49 MeV $\beta^-$	140 s	30 b
$^{109}\text{Ag} (n, \gamma)$	48.2%	2.24 / 2.82 MeV $\beta^-$	24.2 s	110 b

Table 4.1: Silver activation reactions[21]

By contrast a handful of isotopes have neutron reactions with a high probability of capturing neutrons and promptly emitting energetic charged particles, such as alpha

particles ( $\alpha$ ) and heavy charged ions. The most useful of these are  $^3\text{He}$ ,  $^6\text{Li}$  and  $^{10}\text{B}$ . As helium is only available as a gas, it is difficult to incorporate into scintillation detectors, and as discussed in chapter 1 is now commercially far from ideal. That leaves  $^6\text{Li}$  and  $^{10}\text{B}$  as the only suitable capture agents for use in composite scintillation detectors, as summarized in Table 4.2.

Isotope	Abundance	Stable Compounds	Thermal Cross Section	Reaction Products	Reaction Energy MeV	Cost £/gm
$^6\text{Li}$ (n, $\alpha$ )	7.4%	LiF Li Glass	940 b	$^3\text{H} + \alpha$	4.78	50
$^{10}\text{B}$ (n, $\alpha$ )	19.8%	BF <sub>3</sub> gas BN, B <sub>2</sub> O <sub>3</sub>	3840 b	$^7\text{Li} + \alpha$	2.31 - 93% 2.78 - 7%	5.5

Table 4.2: Prompt neutron reactions emitting energetic charged particles

In both these isotopes sufficient energy is released into the reaction products, in order to produce either a direct interaction in an ionising tube or solid state device, or to initiate a significant scintillation event in a scintillating compound.  $^6\text{Li}$ , although lower in cross section, produces the most energetic reaction products. As such it is an ideal candidate for scintillation detectors, and has been the element of choice in both bulk and imaging systems [42, 43], including Barton's original laminar detector [17]. However for reasons of price and availability, detailed in Chapter 2,  $^6\text{Li}$  has been rejected as a capture isotope, in favour of  $^{10}\text{B}$ , for the low cost devices under development in this project.

### 4.3 Boron as a neutron capture agent

Boron is a relatively rare metallic element, however several of its oxides are water soluble, and it is therefore found in significant quantities as evaporated deposits; these are mined for various industrial applications, including the production of bleach, fibreglass, ceramics and semiconductors [64]. The average isotopic distribution of natural boron is 19.8%  $^{10}\text{B}$  and 80.2%  $^{11}\text{B}$  [57], giving it a standard atomic weight of 10.81. Several stable, solid boron compounds are commercially available such as sodium borate (Borax),

BP,  $\text{MgB}_2$ , BN,  $\text{B}_4\text{C}$  and numerous hydrocarbon based compounds including organoboranes, carboranes, etc.

Boron has been used for many years as a neutron capture agent in organic scintillation detectors, commercially available as both liquid and plastic scintillators such as; Bicon Bc-454 [58] and Eljen EJ-254 [59], where 5% by weight of natural boron is present (approx. 1%  $^{10}\text{B}$ ). In these applications the boron is held within the organic polymer matrix and is therefore relatively stable. The one clear disadvantage with this type of detector is sensitivity to gamma radiation. Although this can be mitigated by pulse shape discrimination; for low background applications, such as security portals, this source of 'noise' is completely unacceptable, and rules out the use of this technology.

Combined with an inorganic scintillator, in thin layers, boron has been used to produce thermal neutron detectors with reasonable sensitivity and a high degree of gamma immunity, Gatti [60] achieved 6% effective sensitivity in 1952 with almost complete gamma insensitivity.

In the selection of an appropriate boron compound for use in detector panels, the following factors must be taken into consideration;

1. Stability in solid form; necessary for ease of manufacture and robustness.
2. Non hygroscopic; impractical to have a sealed enclosure.
3. Good optical properties; colour, refractive index, opacity.
4. High proportion of boron within the compound; the higher the better.
5. Cost and availability; ideally commercially available as a fine powder.

Of the available organic compounds almost all are too reactive, or contain only a small proportion of boron. Several inorganic compounds on the other hand such as  $\text{MgB}_2$  and  $\text{B}_4\text{C}$  have a very high proportion of boron and meet all the other criteria with the notable exception of their optical properties. For example; both magnesium borate and boron carbide are dark grey to black in colour, and therefore offer limited scope for transmission of light. Boron nitride however has a high proportion of boron, is highly stable and is available as a white powder.

### 4.3.1 Boron Nitride

With the simple formula BN and a molar mass of 24.82, boron nitride is highly stable in two solid crystalline forms; cubic and hexagonal. In this respect BN is very similar to carbon, with the properties of the two crystalline structures closely parallel to those of carbon. In its cubic form it is comparable to diamond; being inert, very hard, and although not completely clear it is translucent. However with a high refractive index and rough surface it appears pale grey in powder form. It is readily available, in this form, as it is produced commercially for use as an abrasive, in applications where diamond is too reactive, e.g. for polishing steel. Hexagonal BN has a layered structure similar to graphite. In this form it is soft, and white in colour, and is readily found in fine powder form, for use as a lubricant, particularly in the paints and cosmetics industry.

Boron nitride has been reported in several papers to have scintillating properties [61, 62]. However its performance as a scintillator was reportedly modest, and could not be readily reproduced in the laboratory using the samples of BN available to us.

Structure	Density ( $\text{gcm}^{-3}$ )	Refractive index	Colour / Opacity	Typical Grain size ( $\mu\text{m}$ )	Cost (\$/gm)
Hexagonal	2.1	1.8	White / opaque	<2	0.1
Cubic	3.45	2.1	Straw / clear	1 - 3	5

Table 4.3: *Physical properties of boron nitride*[63, 64]

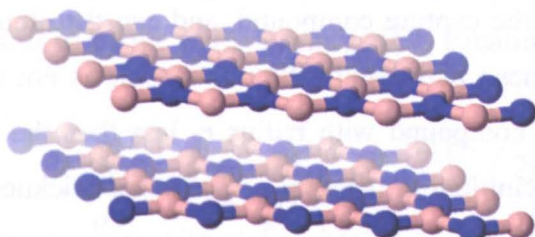


Fig. 4.1: *Hexagonal  $\alpha$ -BN structure*

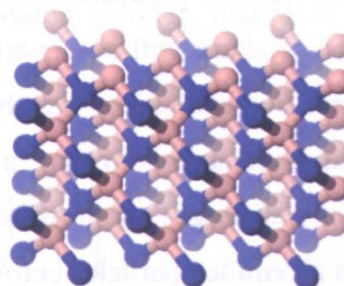


Fig. 4.2: *Cubic  $\beta$ -BN structure*

In order to assess the properties and performance of the two forms of BN the following samples were acquired from commercial suppliers;

1. Cubic BN powder with a grain size of 1-3  $\mu\text{m}$ , purity 99%. Supplied by Superabrasive Technologies Ltd, Leighton Buzzard.
2. Hexagonal BN powder with a nominal grain size of 2  $\mu\text{m}$ , fractional content of Boron 44%. Supplied by ESK Ceramics GMBH.

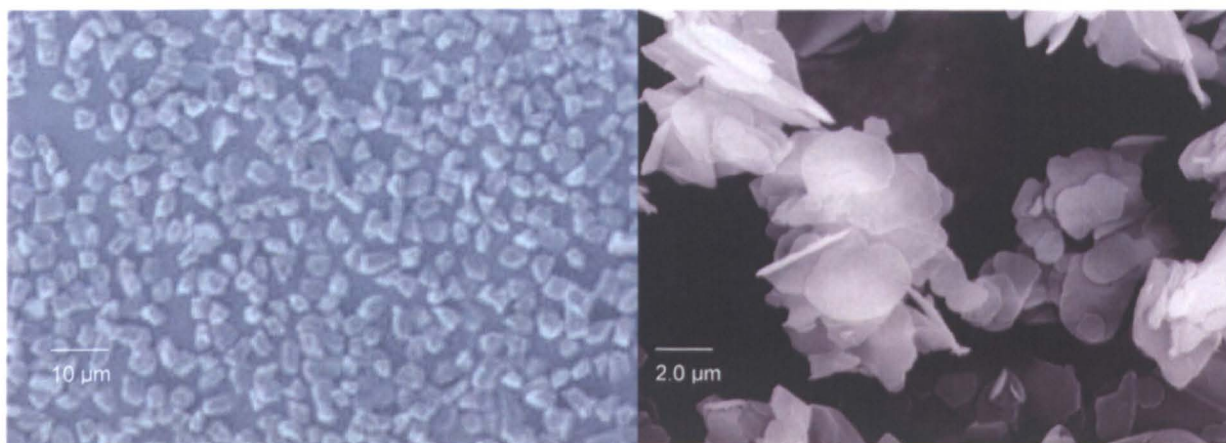


Fig. 4.3: *Cubic BN (left), Hexagonal BN (Right)*[64]

### 4.3.2 Grain size

It is believed that particle size, for both the capture agent and the scintillating compound, is of critical importance to the success of the detector. Hutchinson [53] broadly found the grain size to be inversely proportional to sensitivity in  $\text{LiF}:\text{ZnS}$  screens. Stephan [37] conducted a Monte Carlo analysis of similar screens and concluded that grain radii of 1 – 5  $\mu\text{m}$  offered the best detection characteristics. Where the mean free path length of the charged reaction products is smaller than the grain size it is clearly possible that some reaction products will not emerge from the capture compound, and can therefore not be detected. For grain sizes less than the mean path length the relationship is not so clear. The ideal scenario is to have a capture compound with radius  $r_g$  less than the reaction product path length  $r_a$ , surrounded by scintillation material of sufficient thickness  $r_{gg}$  to absorb all emitted particles before they re-enter an adjacent grain of capture compound, as shown in Fig. 4.4.

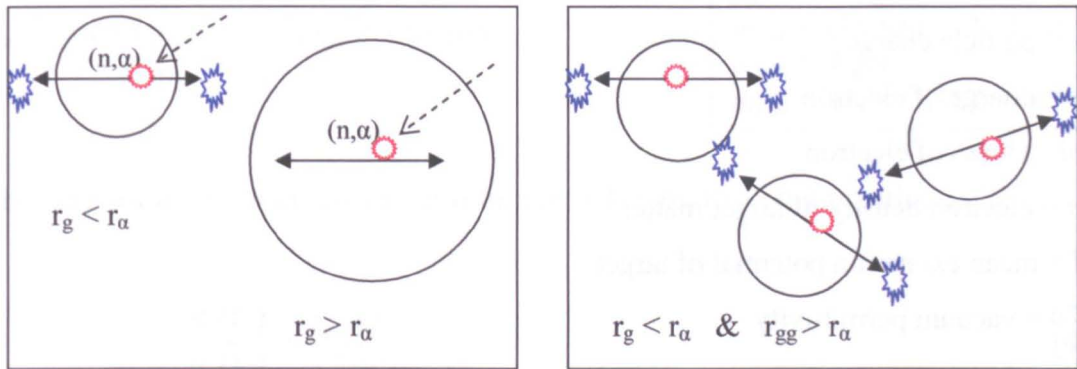


Fig. 4.4 a,b: Grain size consideration in BN; a – left illustrates implications of capture particle size, b – right need for sufficient scintillating material

During the  $^{10}\text{B}$  (n,  $\alpha$ ) reaction the interacting neutrons are predominantly thermalised (<0.025eV) and can be assumed to have no kinetic energy. For conservation of momentum, the reaction products will therefore be emitted in opposite directions, and the distribution of energy between the lithium nucleus and the alpha particle can be readily calculated, from their relative mass  $M_{\text{Li}}$  and  $M_{\alpha}$ :

$$E_{\text{Li}} + E_{\alpha} = 2.31 \text{ MeV} \quad [4.5]$$

$$\sqrt{2M_{\text{Li}}E_{\text{Li}}} = \sqrt{2M_{\alpha}E_{\alpha}} \quad [4.6]$$

By solving the simultaneous equations [4.5] and [4.6] it can be shown that;

$$E_{\text{Li}} = 0.84 \text{ MeV} \quad \text{and} \quad E_{\alpha} = 1.47 \text{ MeV}$$

The rate of energy loss for charged particles passing through matter is classically described by the Bethe Formula [65] equation [4.7]

$$-\frac{dE}{dx} = \frac{4\pi}{m_c c^2} \cdot \frac{nz^2}{\beta^2} \cdot \left(\frac{e^2}{4\pi\epsilon_0}\right)^2 \left[ \ln\left(\frac{2m_c c^2 \beta^2}{I(1-\beta^2)}\right) - \beta^2 \right] \quad [4.7]$$

Where;

$$\beta = v / c$$

$v$  = particle velocity

$E$  = particle energy

$x$  = distance travelled

$z$  = particle charge

$e$  = charge of electron

$m_e$  = mass of electron

$n$  = electron density of target matter

$I$  = mean excitation potential of target

$\epsilon_0$  = vacuum permittivity

For low energy ( $v \ll c$ ) this reduces to [4.8]

$$-\frac{dE}{dx} = \frac{4\pi n z^2}{m_e v^2} \left( \frac{e^2}{4\pi\epsilon_0} \right)^2 \left[ \ln \left( \frac{2m_e v^2}{I} \right) \right] \quad [4.8]$$

For a given particle of known energy the relative path length  $R_n$  in any medium of atomic mass  $m_n$  density  $\rho_n$  can be calculated using the Bragg – Kleeman rule [66] equation [4.9]

$$\frac{R_1}{R_2} = \frac{\rho_2}{\rho_1} \sqrt{\frac{m_1}{m_2}} \quad [4.9]$$

As the density of air is  $0.001293 \text{ g/cm}^3$  [67] and the effective atomic mass of air is about 14, the mean free path lengths for the  $\alpha$  and Li ion relative to those in air are therefore;

$$R = 3.46 \times 10^{-4} \cdot \frac{\sqrt{m}}{\rho} \cdot R_{air} \quad [4.10]$$

The alpha particle range in air (at  $15^\circ\text{C}$  and 1 atm) [67] is closely approximated by:

$$R_{\alpha\text{-air}}[\text{cm}] = \begin{cases} 0.56 E_\alpha & \text{for } E_\alpha < 4 \text{ MeV} \\ 0.325 E_\alpha^{1.5} & \text{for } 4 \leq E_\alpha \leq 8 \text{ MeV} \end{cases}$$

Applying [4.10] to the alpha particle generated in boron on neutron capture (energy 1.47 MeV) the range can thus be calculated as;

$$R_{\alpha \text{ BN}} = 4.86 \mu\text{m} \quad R_{\alpha \text{ ZnS}} = 4.58 \mu\text{m}$$

$\rho_{\text{BN}} = 1.9 \text{ gcm}^{-3}$ $m_{\text{BN}} = (10.8+14)/2 = 12.4$ $\rho_{\text{ZnS}} = 4 \text{ gcm}^{-3}$ $m_{\text{ZnS}} = (32+65.3)/2 = 48.65$
---

The range of the Lithium ion can also be derived from the Bethe equation as;

$$\frac{R_1(V)}{R_2(V)} = \frac{z_2^2 \cdot m_1}{z_1^2 \cdot m_2} \quad [4.11]$$

Where  $R_1(V)$  and  $R_2(V)$  are ranges for different particles of the same initial velocity,  $z$  is the charge and  $m$  is the mass of the particle. From [4.11] it can be calculated that;

$$R_{\text{Li BN}} = 4.86 \times 0.08 \times 4 = 1.55 \mu\text{m}$$

$$R_{\text{Li ZnS}} = 4.58 \times 0.08 \times 4 = 1.48 \mu\text{m}$$

$\text{From } E = 0.5 v^2 m$ $V_{\text{Li}} = \sqrt{(2 \times 0.84 \times 1.6 \times 10^{-13} / 7 \times 1.7 \times 10^{-27})} = 4.7 \times 10^6$ $E_{\alpha}(V) = 0.12 \text{ MeV}$ $R_{\text{Li}} / R_{\alpha} = 0.081$
--

The rate at which these particles collect electrons and loose their charge is however far from linear, therefore these figures are only useful as a guide. A more accurate figure can generated from Monte Carlo analysis, for example using the SRIM code (Stopping and Range of Ions in Matter [68]). This program has been used and enhanced for almost thirty years. It is therefore well tested and should be reliable for most standard material and conditions. Predictions of path length produced using SRIM are shown in Fig. 4.5, for the reaction products of  $^{10}\text{B}$  and  $^6\text{Li}$  in ZnS LiF and BN. The values corresponding to the energy of the reaction product generated on neutron capture have been marked with circles for  $^{10}\text{B}$  and triangles for  $^6\text{Li}$ . The SRIM results tally well with the empirical calculations for  $\alpha$  particles, but at approximately  $2.5 \mu\text{m}$ , they are somewhat higher than those for the Li ions.

It is clear from these calculations that the paths lengths of the reaction products from  $^{10}\text{B}$  are significantly shorter than those for  $^6\text{Li}$ . It is therefore even more important that small grain BN is used in the detector. An ideal grain size for the BN would appear to be  $< 2 \mu\text{m}$ , with an adjacent layer of ZnS of thickness  $> 5 \mu\text{m}$ . A volumetric ratio for the BN:ZnS of 1:3 would satisfy these conditions.

It is interesting to consider that the hexagonal BN has a platelet structure with thickness much less than the nominal  $2\ \mu\text{m}$  width, as shown in Fig. 4.3. It is possible to envisage that given a thorough technique for mixing, the relatively larger and more symmetrical ZnS grains could be well surrounded by a relatively thin layer of BN, providing short coupling path for the charged reaction products between the BN and ZnS.

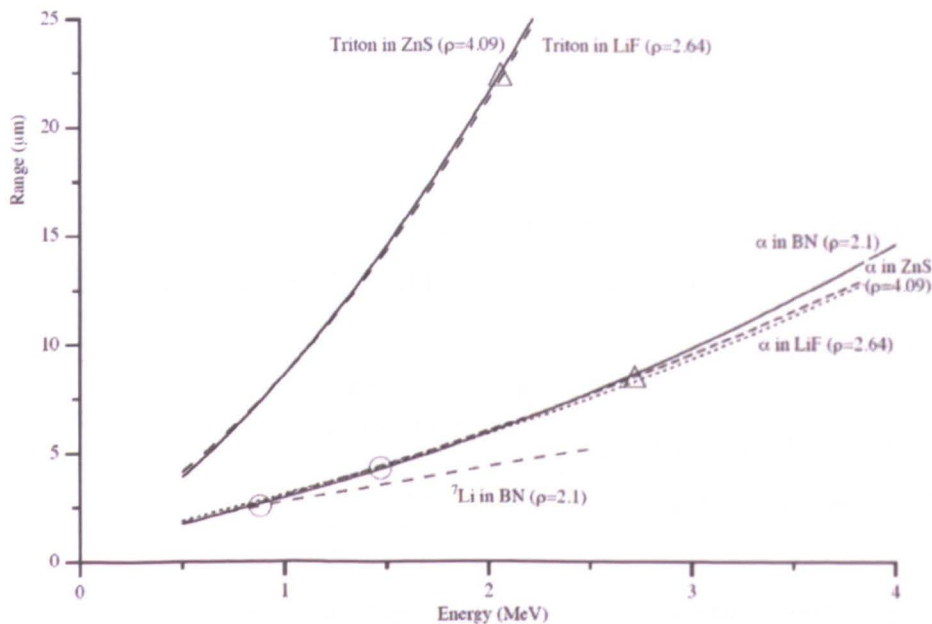


Fig. 4.5: SRIM calculations for  $^3\text{H}$ ,  $\alpha$  and  $^7\text{Li}$  ions in BN, LiF and ZnS

A plot of the energy loss through the path length is described by the Bragg curve. Fig. 4.6 shows a typical example. It is interesting to note that a significant proportion of the energy of the particle is deposited in final stages of its path. This is encouraging for our application as it suggests a reasonable proportion of the total energy will be deposited in the scintillator material, rather than the BN where the charged particle is generated.

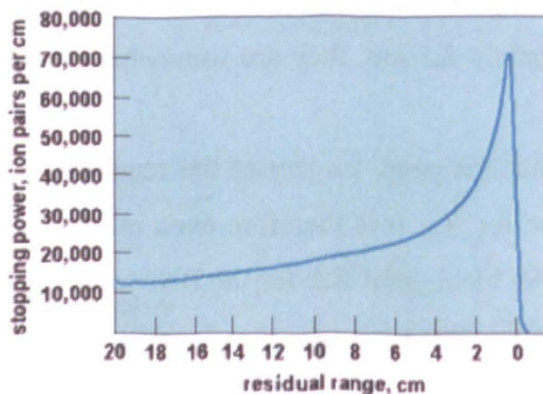


Fig. 4.6: Energy deposition of charged particles (Bragg curve) for alpha particles in air [69]

## 4.4 Performance of scintillating compounds

Selection of an appropriate scintillating material is an essential aspect of the design of a compound laminar neutron detector. The primary requirements for this application are as follows;

- High photon conversion efficiency when interacting with  $\alpha$  particles and other neutron capture products.
- Short wavelength of maximum emission ideally  $< 450$  nm to allow efficient wavelength shifting in the light guide and subsequent detection, typically by a photomultiplier tube.
- Long term stability. In particular the material should be non-hygroscopic, due to a potentially large exposed surface area.
- Reasonable transparency and low refractive index to minimise the self absorption of scintillated light.

Other factors such as cost and availability in powder form (with grain size  $< 10$   $\mu\text{m}$ ) are important but can often be difficult to ascertain without placing orders, as they are very much dependent on quantity and application. However specialist scintillating materials containing high purity components and rare earth metals, e.g. Lutetium, Thallium, Gallium, Europium and Cerium, have been found to have higher cost by at least an order of magnitude than standard bulk compounds such as CsI, ZnS and most plastic scintillators.

### 4.4.1 Inorganic Scintillators

By far the largest class of scintillators is inorganic, from the zinc sulphide plates used by Rutherford, to recently commercialised cerium doped chlorides and bromides [70, 71]. They offer unrivalled brightness and energy resolution, however this is often at the expense of long luminescence decay time and mechanical inflexibility. Table 4.4 lists the key performance characteristics of some of the most important inorganic scintillators, all

of which exhibit peak emissions in the Blue – Blue/Green, wavelengths required for optimum performance in this application.

Luminescence in inorganic scintillators is a property of the material in its crystalline state and can be categorised as either intrinsic (self-activating) or extrinsic (activated). Luminescent centres, where radiative transitions occur, in intrinsic scintillators are molecular systems of the lattice, or defects within the lattice. Extrinsic scintillators form luminescent centres through the addition of doping ions, or activators. Although there is no firm rule, self-activated scintillators often have low efficiency and fast decay time compared to equivalent activated compounds which form the bulk of commercial scintillation detectors [21]. The mechanisms by which scintillation occurs are highly complex and not fully understood for many compounds. Therefore most development and characterization of scintillators is derived empirically. In some cases this leads to wide variations in reported performance of apparently similar materials, ZnS(Ag) being a particularly noticeable example[38,39,72,73,74], where widely differing performance can result from minor composition changes or the presence of trace impurities.

While the number of photons produced in the scintillator is approximately linear with the energy deposited, the relative performance of inorganic scintillators to gamma and alpha radiation varies for different materials. However in general the scintillation efficiency is much less dependant on particle type than for organic materials (typical  $\alpha:\gamma$  ratios are between 0.2 for oxides such as BGO and 0.7 for alkaline halides NaI(Tl) and CsI(Tl) [75]). This means they are well suited to application in neutron plates, especially where gamma rejection is an issue.

A major problem in the use of inorganic scintillators is their mechanical vulnerability, particularly when dealing with single crystals, additionally these materials are often very hygroscopic (eg NaI, CsI(Na) etc). Both these factors cause significant problems, when dealing with large detectors, which are reflected in the complexity and cost of detector systems. There are however a number of manufacturing techniques used to mitigate these problems which can be applied to applications requiring thin film scintillators [22]:

- *Glass*: Simple to manufacture, low light yield due to irregular lattice structure. Specifically  $^6\text{Li}$  based for neutron detection, gadolinium silicate Tb-doped for X-rays.

- *Powder*: As used on X-ray screens e.g. ZnS:Ag, LaOBr:Tm, gives good spectral resolution. Because of poor light transmission, efficiency is low. Powder dispersed in a polymer matrix of similar refractive index can improve efficiency, but is not suitable for hygroscopic materials.
- *Ceramics*: Can have density up to 99.9% of single crystal, with <30  $\mu\text{m}$  grain size. Efficiency up to 50% of NaI:Tl.
- *Films*: Epitaxial growth onto a substrate used to produce thin films of practically all scintillation materials.

Scintillator	$\lambda_{\text{max}}$ (nm)	$\rho$ ( $\text{gcm}^{-3}$ )	$\gamma$ ray Efficiency (photons/ MeV)	Decay time (ns)	$\alpha$ : $\beta$ ratio	Refractive index	Stability - Common name	Ref.
NaI:Tl	415	3.67	43,000	230	0.66	1.85	♦	21,22
CsI *	310	4.51	2,000	16	0.85	1.95	◇	21
CsI:Tl	560	4.51	51,800	560	0.67	1.79	◇	21,22
CsI:Na	420	4.51	38,500	420	0.5	1.84	♦	21,22
CaI <sub>2</sub>	410	3.96	86,000	550			♦	21
BiGeO	480	7.13	4,500	340	0.2	2.15	BGO	
ZnS:Ag	450	4.09	47,000	<1000	0.5	2.36		21
ZnO:Ga *	400	5.6	<40,000	< 5		2		76,77
CaF <sub>2</sub> :Eu	433	3.18	24,000	800	0.2	1.44		78
CaF <sub>2</sub> *	~250	3.18	<20,000	900		1.44		79
LaBr <sub>3</sub> :Ce	380	5.29	61,000	28			♦	71
CeBr <sub>3</sub>	371	5.2	68,000	17			♦	70
CeCl <sub>3</sub> :Ce	360	3.9	28,000	23			◇	70
RbGd <sub>2</sub> Br <sub>7</sub> :Ce	420	4.8	54,700	66				21
Y <sub>2</sub> O <sub>3</sub>	370	5.04	15,480	28	0.2			21
CdWO <sub>4</sub>	470	7.9	19,700	2,000	0.2	2.2		21
YAlO <sub>3</sub> :Ce	365	5.3	18,000	30		2.0	YAP	81
Y <sub>3</sub> Al <sub>5</sub> O <sub>12</sub> :Ce	550	5.35	17,000	31		1.9	YAG	82
Y <sub>2</sub> SiO <sub>5</sub> :Ce	420	2.7	25,000	40		1.8	YSO	82
LuAlO <sub>3</sub> :Ce	375	8.34	11,400	16/80/			LuAP	83

				520				
$\text{Lu}_2\text{SiO}_5:\text{Ce}$	420	7.4	30,000	40		1.82	LSO	83
$\text{Lu}_2\text{SiO}_7:\text{Ce}$	380	7.3	30,000	30		1.8	LPS	83,84
$\text{ScBO}_3:\text{Ce}$	380	2	17,000	30			SBO	82
$\text{BaF}_2$	220	5	4,000	0.8			◇	83
	320		12,000	630				
BN	400	2.1	2,000	2.5		1.65/2.	HDBN	61
						13		
Ce Glass	~450	2.6	<3500	50 - 75	0.1	1.5		21

Table 4.4: *Properties of inorganic scintillators*

◆ *Material is significantly hygroscopic, ◇ material is slightly hygroscopic,*

*\*data shows significant discrepancies, this may be partly due to different doping / testing regimes.*

For use as thin films, in laminar neutron detectors, the above scintillators can be narrowed down significantly by excluding all those which are hygroscopic, have low efficiency, or produce a peak emission wavelength outside the blue range (above 500nm):

The most suitable remaining candidates are therefore;  $\text{ZnS}:\text{Ag}$ ,  $\text{ZnO}:\text{Ga}$ , plus the cerium doped fast inorganics such as LSO and YAP. Although many studies have been made of the performance of these materials results vary widely, presumably due to variations in the composition and preparation of the test samples:

## **ZnS:Ag**

Although doped Zinc Sulphide is one of the oldest and brightest of the scintillators, due to its opacity it is only useful in thicknesses up to  $25 \text{ mg/cm}^2$  [21]. At these thicknesses it performs poorly as a gamma detector, but is more than sufficient to capture the energy in heavy charged particles. However finding an accurate figure for the absolute conversion efficiency of  $\text{ZnS}(\text{Ag})$  is difficult, as numerous recipes for this scintillating compound exist, manufactured for a variety of applications such as; cathode ray tubes (CRTs), fluorescent lighting and x-ray imaging. Incorporating varying concentration of the silver dopant and quenching agents such as nickel and chlorine, the different grades of material

appear to have widely varying brightness and decay time. Numerous studies have been undertaken to assess and optimize ZnS as a scintillation detector[38,39,72,73,74], both in relation to its brightness and decay characteristics and results vary widely.

A conservative estimate of conversion efficiency for gamma is 13% [23]. For 450 nm light (2.75 eV) this equates to 47,000 photons for 1 MeV input. Efficiency for alpha is believed to be approximately 60% of the figure for gamma, due to a quenching effect on the rapid ionisation caused by the passage of the charged particle [22]. This equates to overall efficiency of 8% or  $2.8 \times 10^4$  photons/ 1MeV $\alpha$ . This relatively high ratio of alpha : gamma efficiency is clearly an advantage where gamma rejection is required. The high refractive index means that particle size also affects efficiency due to internal reflections and light trapping.

The spectral response of ZnS(Ag) varies with manufacture. Fig. 4.7 shows absorption and emission peaks for a typical grade supplied by Phosphor Technologies. The 450 nm emission peak for ZnS:Ag is well matched to standard Bialki photomultipliers (400 nm peak response) [84], however after wavelength shifting in the light guide, by typically 100 nm, the resultant emission peak is around 550 nm. The PMT sensitivity at this wavelength is reduced by up to 50%.

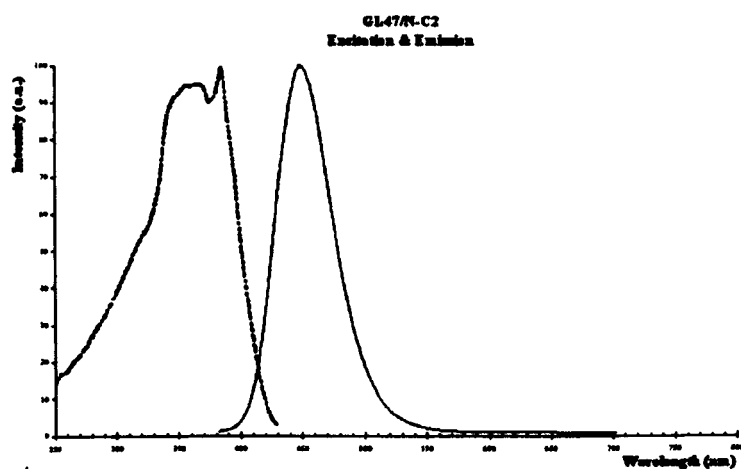


Fig. 4.6: *Excitation(dotted) / emission spectrum for ZnS:Ag [Phosphor Technologies' grade GL47]*

Due to its slow decay time (in excess of  $1\mu\text{s}$ ) ZnS is only appropriate for low count rate applications. Work has been done by Barton [26] to improve response time, through the addition of nickel which acts as a quench element, however this appears to be at the cost of efficiency. Matsubayashi [40] reported that high Ni content also has a

detrimental effect on opacity (with a noticeable yellowing). Optimising Ni content is therefore important where reasonable speed and maximum efficiency is required, e.g. due to self absorption etc.

ZnS:Ag is readily available in large quantities and at relatively low cost from a number of commercial suppliers. Phosphor Technology [85] supply several grades for prices between £250 and £340 per kg (2008). The different properties of these products are determined by the market for which they were developed, as shown in table 4.5, and are generally available in different mean particle sizes from 3 to 10  $\mu\text{m}$ .

Grade	Type	Application	Characteristics	2008 Price £/kg
GL47/N-S1	Scintillation	Screens etc	Ni killed – short decay time	£322
GL47/N-C1	P11	CRT	Deep Blue – long decay	£348
CL47/N-C2	P12	CRT	Bright Blue – long decay	£243

Table 4.5: *Properties of commercial grade ZnS [85]*

## ZnO

Studies have been made into the performance of un-doped ZnO [76] and Gallium doped ZnO:Ga as a detector of  $\alpha$  particles [77]. Whilst they conclude that ZnO is a very fast inorganic scintillator, with a decay time of between 1 and 5 ns, figures for the efficiency are less clear suggesting between 5,000 and 40,000 photons/MeV. Barton [72] directly compared ZnO:Ga with ZnS:Ag and found the ratio of light output to be a approximately 1:3.

The excitation and emission peaks for ZnO:Ga are shown in Fig. 4.8. While the peak emission wavelength of 400nm is suitable for wavelength shifting, the small Stokes shift is indicative of a relatively high self absorption. This may well be the cause of the fast decay time and lower overall efficiency. While ZnO is interesting for applications requiring high count rates, its fast scintillation decay will severely hamper neutron discrimination techniques, required in applications where low background rate and gamma rejection are important.

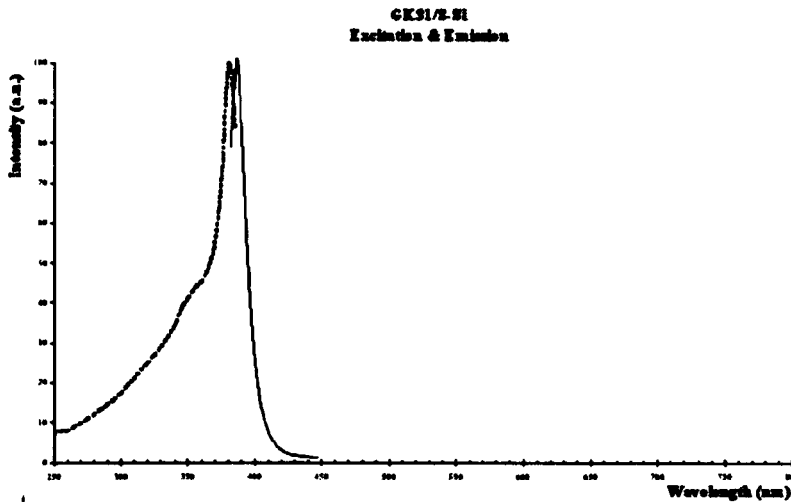


Fig. 4.8: Excitation(dotted) / emission spectrum for ZnO:Ga [Phosphor Technologies' grade GK31]

## CaF<sub>2</sub>

Although CaF<sub>2</sub>:Eu has a lower conversion efficiency than ZnS:Ag [78], it has shorter decay time and slightly shorter emission wavelength, it also has a lower refractive index which will improve optical performance when mixed with a binding agent [79]. CaF<sub>2</sub>:Eu is often used in Phoswich detectors as the  $\beta$  detector in combination with NaI for  $\gamma$ . Here its low effective atomic number ( $Z_{\text{eff}} = 16.5$ ) reduces  $\beta$  scattering, and long decay time enables pulse shape discrimination. Due to the cost of rare earth materials CaF<sub>2</sub>:Eu is however an expensive specialised product.

Undoped CaF<sub>2</sub> is also known to be a good scintillator having an efficiency of about 80% of CaF<sub>2</sub>:Eu, it also has a slightly longer decay time of 940 ns [78, 79]. It is optically clear, has a short emission wavelength <300 nm and is readily available (£30 /kg), and may therefore be worth considering as a candidate for this application. A relatively rapid roll off with temperature is a concern for CaF<sub>2</sub>:Eu and CaF<sub>2</sub> for applications in non-laboratory environments.

## Ce Doped Fast Inorganics

This is a more recently developed group of scintillators, which offer the benefits of fast response, short wavelength of peak emission and relatively high efficiency. However in

general they are expensive to manufacture due to the high content of rare earth materials, this could exclude them for use on a large scale. Of these raw products Lutetium is the rarest and the most expensive at a price of \$144 /g (Aldrich 2011), and should therefore be avoided.

The most widely available of these materials is  $\text{Y}_2\text{SiO}_5:\text{Ce}$  (YSO). This is commonly used in scanning electron microscopes, and is available as a powder. At a typical cost of \$10 per gram [49], for small quantities, it is an order of magnitude more expensive than ZnS.

YAP ( $\text{YAlO}_3:\text{Ce}$ ) and YAG ( $\text{Y}_3\text{Al}_5\text{O}_{12}:\text{Ce}$ ) are both widely used as stable single crystals and powders, and are both suitable for  $\alpha$  detection, with a reported efficiency relative to ZnS:Ag of 30% and 11% respectively [72, 81]. An excitation and emission spectrum for a commercial grade of YAP is shown in Fig. 4.9. An interesting characteristic of this material is the low peak emission wavelength, which would be well suited for use with wavelength shifters.

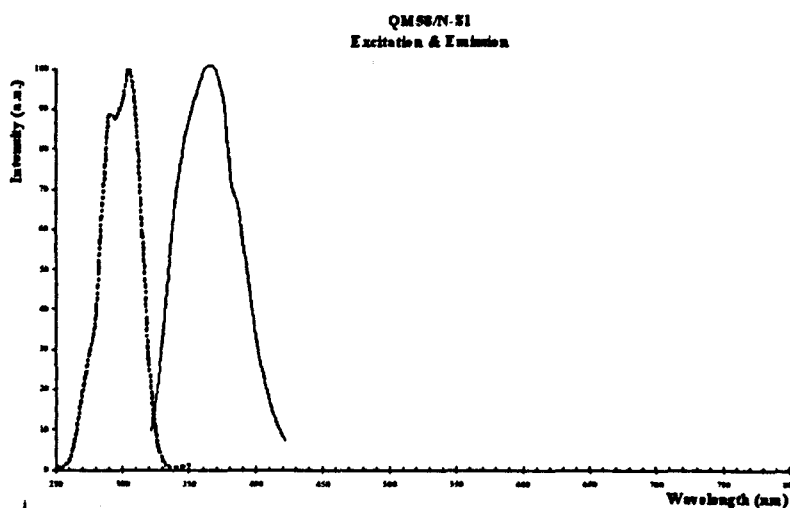


Fig. 4.9: *Excitation / emission spectrum YAP*

## 4.4.2 Organic Scintillators

In contrast to inorganic crystals, luminescence in organic compounds is an inherent molecular property seen in any phase (solid, liquid or gas)[21]. Organic scintillators tend to be characterised by a faster decay time, but lower efficiency than inorganics. Luminescent decay time is described by a fast (2-30 ns) and slow ( $>1 \mu\text{s}$ ) component. The overall and relative intensity of these components is dependent on the type of particle causing the scintillation due to ionisation quenching. For the fast component, electrons,

protons, neutrons and alpha particles have an approximate intensity ratio of 10:5:4:1 [22] which varies non-linearly with absorbed energy. The delayed scintillation component is much less affected by particle type; thus allowing particle identification through pulse shape discrimination, as shown in Table 4.6.

Particle	Relative fast scintillation component	Tail emission (% of main pulse)	Delayed photons per MeV
5 MeV $\alpha$ particle	1	20	350
5 MeV neutron	4	14	980
1.1 MeV gamma	10	3.5	610

Table 4.6: *Ratio of fast and slow scintillation components in anthracene [22]*

Whilst there are many scintillating organic compounds only relatively few are widely used; these are generally combined in small concentrations within a bulk solvent, and possibly a wavelength shifter. Energy from the interacting particle absorbed by the bulk solvent is passed to the scintillator; light produced can then be wavelength shifted, as required to produce optimum response from the photomultiplier tube. Properties of some standard organic scintillators are given in Table 4.7.

Scintillator	$\lambda_{\text{max}}$ (nm)	$\rho$ ( $\text{gcm}^{-3}$ )	$\gamma$ Efficiency ( $\text{ph MeV}^{-1}$ )	Decay time(ns)	Refractive index	Trade name	Ref.
Anthracene	447	1.25	18,000	32	1.6		[22]
Stilbene	410	1.16	10,000	4.5	1.6		[22]
Polystyrene			7,000				[86]
PVT	400	1.3	10,000	2.4	1.6	BC-400	[87]
Liquid	425	0.88	16,000	2.5		BC-505	[87]
Ir doped PVT	520		32,000	850			[88]
PVK : Ir	510		32,000	850			[89]
pTerphenyl	420	1.23	24,300	3.7	1.65	pTP	[90]

Table 4.7: *Properties of common organic scintillators*

Organic scintillators can be fabricated into very thin films, down to a film density of  $20 \mu\text{g cm}^{-2}$ , and are commercially available down to  $10 \mu\text{m}$  thick [4]. They are widely used, as timing elements in heavy ion particle experiments [91,92,93], in phosphor sandwich or Phoswich detectors, and in medical dosimetry etc. Their fast response and low atomic mass are of particular importance, as is their ability to be manufactured into almost any shape. Limitations of these detectors are their degradation with temperature and their susceptibility to radiation damage. Materials are being developed to improve these characteristics, but they generally exhibit lower efficiency [94,95].

Response of organic scintillators to heavy charged particles is a complex function of ion velocity and atomic number. In general light yield increases with decreasing atomic number of the ion thus enhancing their performance as  $\alpha$  detectors [96]. However due to ionisation quenching (from damaged molecules) the efficiency of organic scintillators will never approach that of the best inorganic scintillators.

A study of one of the most common commercial ternary scintillators NE102 (BC400) for use in thin film detectors [94] concludes that the efficiency is maximised at a thickness corresponding to the ionisation range of alpha particles in the PVT i.e.  $40 \mu\text{m}$  for  $^{241}\text{Am}$ . Overall efficiency for this material to  $\alpha$  particles is  $> 1000$  photons per MeV. This is at least a factor of 10 down on gamma efficiency, and approximately 2% of the performance of ZnS:Ag.

Some work has been done to assess composite organic neutron detectors, but with limited success; Knoll [96] dispersed  $^3\text{He}$  filled microspheres in organic scintillator, however this difficult technique had poor n-gamma discrimination and low overall efficiency. Due to susceptibility to gamma interference and poor overall efficiency it is unlikely that organic materials will be useful for low background neutron applications. However a sample of scintillation grade p-Terphenyl has been acquired for assessment and evaluation. p-Terphenyl (pTP), when doped with diphenylbutadine, has some of the most promising properties of the organic plastic scintillators, including; good light yield, fast recovery, low refractive index and high stability. It is also readily available in powder form and at \$140/kg (Chemical land-industrial chemicals 2010), it is one of the cheapest scintillating compounds.

### 4.4.3 Scintillator testing

Due to variability in the reported performance of scintillating materials (particularly powders), a simple testing regime was undertaken. The objective was not to attempt to produce absolute figures for scintillation brightness etc., but to provide comparative information useful for the selection of a scintillator specific to this application. The following parameters were therefore investigated;

- Relative brightness of initial scintillation peak
- Total relative brightness – integrated signal
- Decay time to 10% of initial peak

Because the broad principal on which the detector is to operate requires the use of wavelength shifting light guides, the above parameters were measured firstly with samples directly coupled to a photomultiplier and subsequently with samples coupled by a short wavelength shifting light guide. As the reaction products from neutron interactions with  $^{10}\text{B}$  and  $^6\text{Li}$  were of primary interest, testing was carried out using a small  $^{241}\text{Am}$  reference source (approximate activity 37 kBq). The alpha decay of  $^{241}\text{Am}$  has five characteristic energies with the most prevalent being 5.486 MeV (85.2%) and 5.443 MeV (12.8%) [144]. While these particles are more energetic than the neutron reaction products for both  $^{10}\text{B}$  and  $^6\text{Li}$ , given in table 4.2, they are close enough to be a good experimental substitute. Furthermore the 57 keV gamma rays emitted by  $^{241}\text{Am}$  are low enough in energy to have little effect on these tests.

The first set of measurements were made using a simple light tight test rig housing a EMI photomultiplier type 9821. Samples were prepared by coating clear adhesive tape with a thin layer of scintillating powder. The tape was then mounted on a slide, powder side up. To prevent cross contamination of the test rig, the bulk of each sample was masked off with further tape, leaving a small window onto which the alpha source could be located using an M4 washer as a stand off.

The photomultiplier was run at a fixed voltage (1750V). A 1GHz bandwidth LeCroy oscilloscope was used to capture pulse data at a sampling rate of 0.4ns. For each sample in excess of 100 pulses were collected and downloaded for analysis. A macro written under Microsoft Excel automated analysis of the data into the following steps;

- Collate all data onto single sheet
- Apply noise gate to remove low level background noise
- Isolate events using a fixed trigger threshold
- Find peak value
- Integrate pulse area
- Measure pulse width to 10% of the peak value

A summary of the results of these tests is given in Table 4.8.

	Peak Height (V)	Pulse Area (nVs)	Pulse width to 10% of peak (ns)
ZnS:Ag (GL47-NS1)	2.77	185	226
ZnS:Ag (GL47-NC1)	0.971	110	458
ZnO:Ga (GK31/S-S1)	5.60	33.2	14.3
YAlO <sub>3</sub> :Ce (QM58/N-S1)	0.628	24.3	117
Y <sub>2</sub> SiO <sub>5</sub> :Ce (QBK58/N-A2)	0.814	30.4	102
p-Terphenyl (PTP)	0.965	11.0	27.0

Table 4.8: *Comparative performance of powdered scintillators under a radiation (measured using EMI 9821 PMT at 1750 V)*

This first indication of the relative merits of the different phosphors raises several interesting points. Firstly while ZnO:Ga generates the highest peak value, by at least a factor of two, its rapid decay characteristic results in a total brightness (indicated by pulse area) significantly worse than the two grades of ZnS. In terms of overall brightness the ZnS:Ag comfortably outperforms the other phosphors, by at least a factor of three. However it is interesting to note the considerable difference between the two samples of ZnS. Phosphor Technology would not provide detailed chemical composition of these materials for commercial reasons, however the S1 grade is described as a scintillation grade material with a shortened decay time achieved through addition of nickel. The C1 grade phosphor is primarily intended for use with cathode ray tubes and as such has a longer decay time. While the addition of nickel in the S1 grade explains the shorter decay time, the contrast in peak signal and total light output between the two samples is

surprising; S1 grade easily outperforming the C1 grade. This is in contrast to work done by Barton [72] who found that while addition of nickel shortened decay time it also reduced overall efficiency. It can only be assumed that the C1 phosphor has a different concentration of silver, or other additions required for CRT applications, possibly to extend the wavelength of the light produced.

Alongside brightness and decay characteristics, wavelength is a critical parameter of the scintillating compound. The efficiency with which the light is collected by the light guide and transmitted to the photomultiplier is undoubtedly responsible for a significant proportion of signal attenuation within the detector. Furthermore it is reported by Barton [97] that the spectral distribution of light in the tail of a ZnS:Ag scintillation event differs from that of the peak, with a UV filter reducing the tail energy by a factor of 5 but leaving the initial peak relatively un-affected. This has implications not only for coupling efficiency but also for pulse shape discrimination techniques. To get a true measure of the performance of each material a test rig was therefore devised to couple the scintillating sample to the PMT through a short interchangeable light guide; Fig 4.10 and 4.11. The light tight assembly was intended as a flexible test bed not only for samples of scintillation materials but also for neutron capture compounds and alternative light guide materials.

For scintillator testing a carriage was fabricated to hold a sample slide, produced as described in the tests above. The  $^{241}\text{Am}$  source was attached to a mounting hole in the assembly, and measurements were taken as in the previous tests.

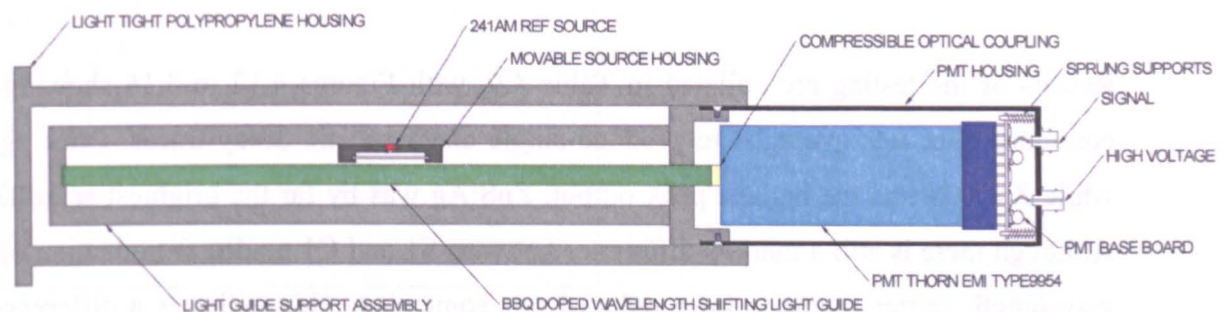


Fig. 4.10: Schematic of test assembly housing wavelength shifting light guide and photomultiplier

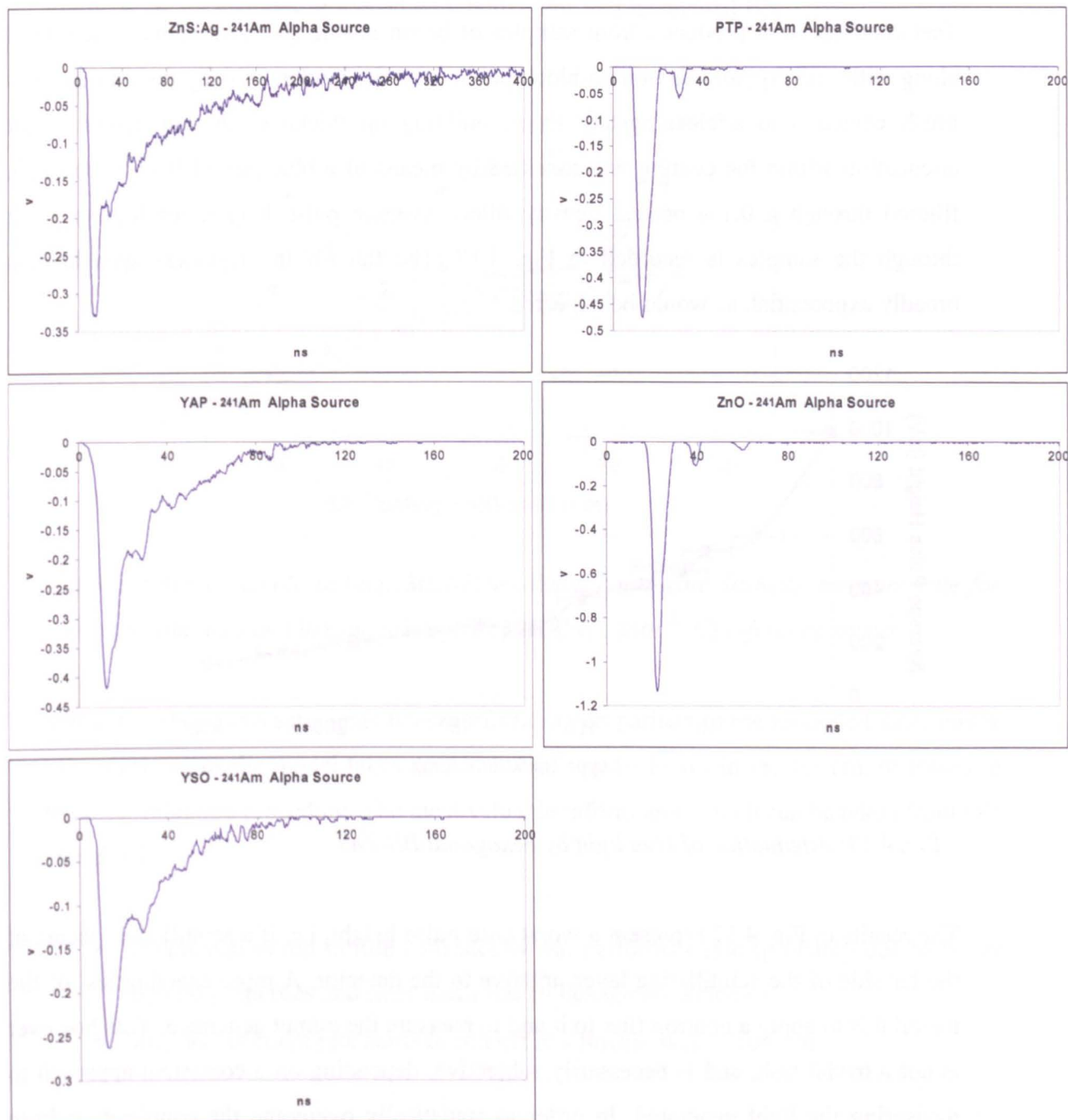


Fig. 4.11: Photograph of light guide test assembly

	Peak Height (V)	Pulse Area (nVs)	Pulse width to 10% of peak (ns)
ZnS:Ag (GL47-NS1)	0.73	45.15	88
ZnS:Ag (GL47-NC1)	0.33	38.17	220
ZnO:Ga	1.22	17.46	8
YAlO <sub>3</sub> :Ce (YAP)	0.42	22.12	67
Y <sub>2</sub> SiO <sub>5</sub> :Ce (YSO)	0.26	13.64	72
p-Terphenyl (PTP)	0.47	10.35	14

Table 4.9: Performance of powdered scintillators coupled by wavelength shifting light guide, when exposed to  $^{241}\text{Am}$   $\alpha$  source

Results of the testing are collated in Table 4.9, with Figures 4.12 to 4.16 showing the combined data sets averaged to produce single characteristic decay traces. Once again, while ZnO:Ga had the highest peak output, ZnS:Ag was by far the brightest scintillator. Although there is still a marked difference between S1 and C1 grades, introduction of the wavelength shifter seems to have reduced this somewhat. This indicates a difference in wavelength for at least a proportion of the light produced. The reasonably short decay time and exceptional brightness of the S1 grade material (along with a relatively low cost) make it the obvious choice for use in thin neutron capture / scintillating layers.



Figures 4.12 to 4.16: Scintillation decay for ZnS:Ag, PTP, YSO, ZNO:Eu, YAP (pulse height in Volts plotted against time in ns). Averaged traces taken through BBQ wavelength shifting light guide

## 4.5 Performance of capture compounds

Test coatings were produced from samples of boron nitride (both hexagonal and cubic) along with ZnS:Ag, and Kraton co-block polymer as the binder. Initially the mixture was brush coated onto a clear acetate sheet, building up thickness in thin layers. Light attenuation within the coating was assessed by means of a blue pulsed IBH Nano LED, filtered through a 0.1% neutral density filter. Average pulse height, for light passing through the samples is recorded in Fig. 4.17. The fall off in brightness seen here is broadly exponential, as would be expected.

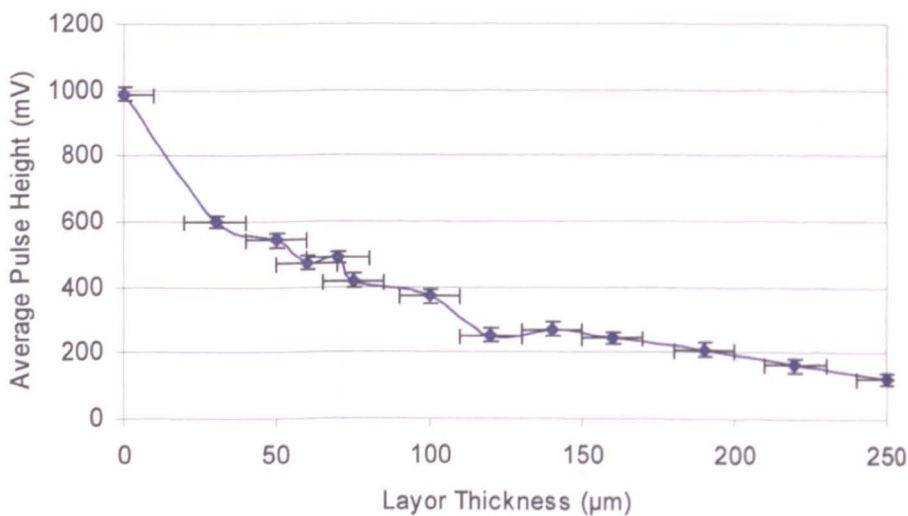


Fig. 4.17: Attenuation of blue light by hexagonal BN/ZnS

The results in Fig. 4.17 represent a worst case pulse height, i.e. if a scintillation occurs at the far side of the scintillating layer, relative to the detector. A more exacting test of the material is to apply a neutron flux to it and to measure the output generated. This however is not a trivial task, and is necessarily subjective, depending on a consistent approach to measuring the light generated. In order to statistically overcome the contribution from photomultiplier noise, and possible background effects it is necessary to use as big a sample as possible, and to apply some type of discrimination technique. The light guide test rig (Fig 4.10 & 4.11) was used with a sample mounted above and below the light guide, and a  $^{252}\text{Cf}$  reference source inserted into a pocket inside the light tight enclosure. Pulses from the PMT were captured by the LeCroy oscilloscope with a fixed threshold setting, and were then downloaded to a PC for analysis. An Excel macro was used to

perform pulse counting analysis on each of the recorded traces (see Chapter 6 for detailed explanation). The measured neutron flux is plotted against MCNP predictions (Chapter 3) in Fig. 4.18, for samples produced with both cubic and hexagonal BN.

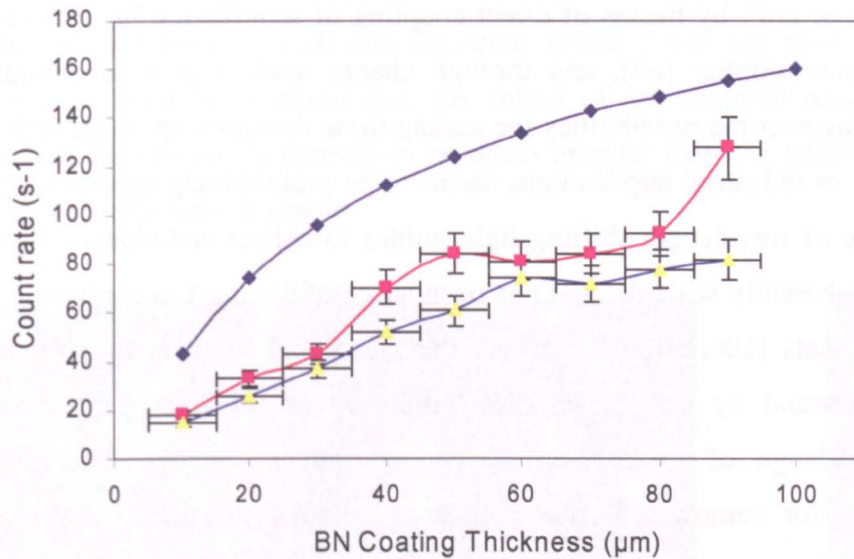


Fig. 4.18: *Small sample testing; MCNP predicted count rate(dashed), measure rate for cubic (bottom line) and hexagonal (top line)BN/ZnS , with  $^{252}\text{Cf}$  reference source.*

While the above measurements underperform in comparison to the modelled data, this is not surprising as the model takes no account of optical losses in the system, or losses in the discrimination procedure. The most valuable information which can be taken from this exercise is;

- Hexagonal boron nitride consistently out performs cubic (probably due to better optical properties and finer grain size in hexagonal material)
- Increase in count rate starts to roll off at a thicknesses of 100 µm

The decision was therefore made to use hexagonal boron nitride, in combination with ZnS:Ag for the coating material, applied at a thickness of between 100 and 200 µm.

## 4.6 Wavelength shifting light guides

Boron Nitride has been used to produce several thermal neutron detectors, with an active area of a few mm or  $\text{cm}^2$ , by means of direct coupling of scintillation layers to a CCD array [98] or photomultiplier [60], and through charge readout of a semiconducting composite [99]. However the possibilities for scaling these detectors up, to an active area useful for security or industrial applications, seems to be prohibitively expensive. On the other hand the use of wavelength shifting light guides to collect and channel light to a photo detector is inherently scalable, and has been successfully used in conjunction with thermal neutron panels [100,101,102]. In fact the theoretical limit to the size of such detectors is only bound by the transmission efficiency of the light guides, and the manufacturing challenge of producing large light tight assemblies. Given quoted attenuation lengths for commercial light guides of up to 4 m (Saint-Gobain [103]), detectors with an active area of  $\text{m}^2$  rather than  $\text{cm}^2$  are almost certainly a realistic goal.

Optimum performance from the detector however can only be achieved by maximising the amount of light transmitted from the capture / scintillating layer to the photomultiplier, in order to allow rejection of noise generated in the PMT or from gamma background. The first consideration in this respect is the selection of an appropriate fluorescent material.

The PNL detector used light guides supplied by Rohm & Haas, sold as Plexiglas GS2025 [104], in sheets 10 mm thick. This material is cast from a polymethylmethacrylate (PMMA) resin containing the fluorescent compound BBQ (Benzimidazo-benzi-sochinolin-7-on) in a concentration of 100mg/l. As well as having excellent optical properties, PMMA has a molecular formula of  $\text{C}_5\text{H}_8\text{O}_2$ , and a density of  $1.18 \text{ gcm}^{-3}$  [134]; this gives it a relatively high hydrogen density, and as such it is a useful neutron moderator.

Rohm Haas no longer supply Plexiglas and as such this particular material is no longer available, however similar products are manufactured by Saint-Gobain Crystals (BC-482A) and Eljen Technology (EJ-280), based on polyvinyl toluene (PVT) [105]. The concern with this material is that as a relatively efficient scintillator, PVT will potentially generate interference pulses, induced by background gamma. Furthermore the specialist nature of this material renders it prohibitively expensive. Other translucent fluorescent acrylics are commercially available from a large number of suppliers, at much lower cost.

These materials are supplied in a range of colours from red to blue, see Figure 4.19, and appear to be mostly manufactured in China, for use in decorative applications such as shop fittings. A fluorescent PMMA acrylic was acquired for testing. Manufactured by BWF profiles [106] and supplied by Clear Plastic Supplies, this material is available as extruded rods from 6 to 20 mm diameter. While it was not possible to discover which dyes were used in its production, the colour of this material was visually close to the green of fluorescein. It appears to be much brighter than the GS2025 and is presumably therefore more heavily doped.

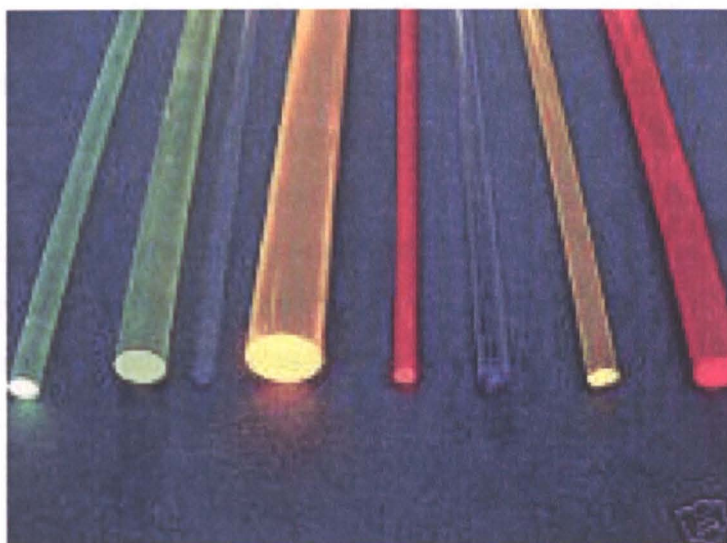
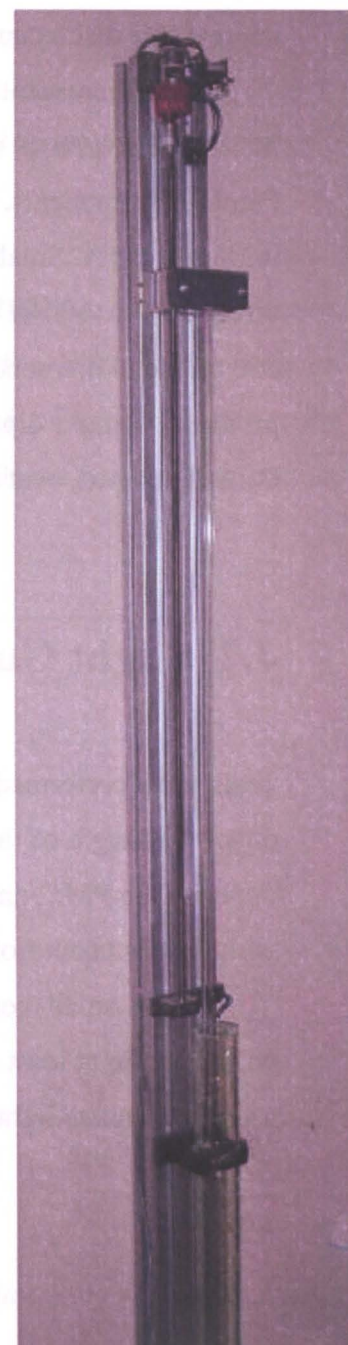
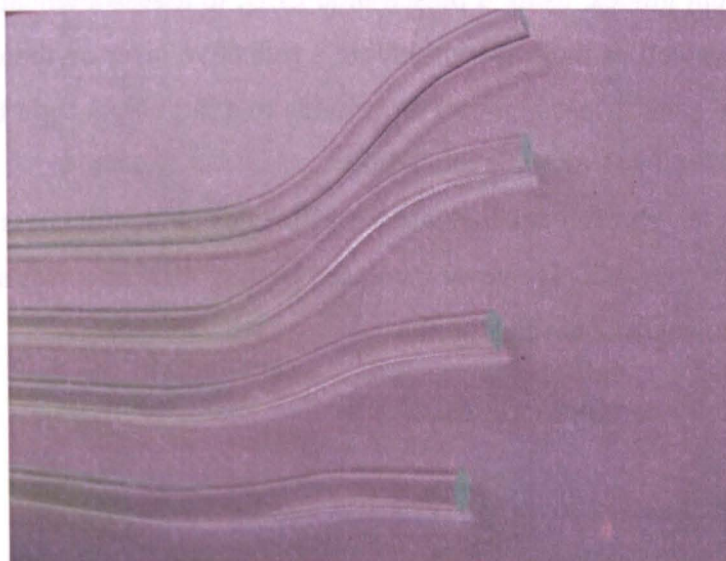


Fig. 4.19: (above) Commercial fluorescent acrylic

Fig. 4.20: (right) Dip coating apparatus for 1 meter rods

Fig. 4.21: (below) Dip coated acrylic light guides bent to shape after coating



An alternative approach to the production of wavelength shifting light guides is by the application of thin films of fluorescent lacquer to a clear acrylic substrate. This technique is described in detail by Viehmann [107], and in theory allows light guides to be made cheaply in almost any shape. Viehmann claims an impressive 100% efficiency was achieved using this technique with 0.2 to 0.5 % concentration of BBQ dye in layers only a few micrometers thick. However, the commercial GS2025 Plexiglas from Rohm Haas has a concentration of 0.01% BBQ and 10mm thickness, employing over 100 times as much dye. It is therefore thought that Viehmann's results can not be taken at face value. To address this discrepancy a program of testing was undertaken.

A fluorescent lacquer was produced by dissolving BBQ in toluene, and then mixing this with a clear conformal coating material (Electrolube HPA), supplied by Farnell Components. Mixtures were made with a concentration of BBQ by weight of 0.2% and 0.5%. Small test light guides were produced by brush application of the coating directly onto 10mm thick acrylic, laser cut to a fixed test sample size of 40 mm x 350 mm, and diamond polished on all faces. Longer 10 mm diameter rod guides were also produced using a dip coating technique and a motorised linear slide shown in Fig. 4.20. Partially coated, bent acrylic rods are shown in Fig. 21.

## 4.7 Light Guide Testing

Tests were performed on all light guides, using a pulsed blue LED, to assess attenuation down the length of the guide, as well as the effect of adding a reflective layer on the end opposite the PMT, and onto the sides. Measurements were made in a large light tight box with signals taken from an ET9791 PMT operating at 2200 V.

The small coated samples showed an increase in efficiency with thickness of coating up to at least 80  $\mu\text{m}$ , see Fig. 4.22. However increased coating thickness was also seen to attenuate light down the length of the light guide.

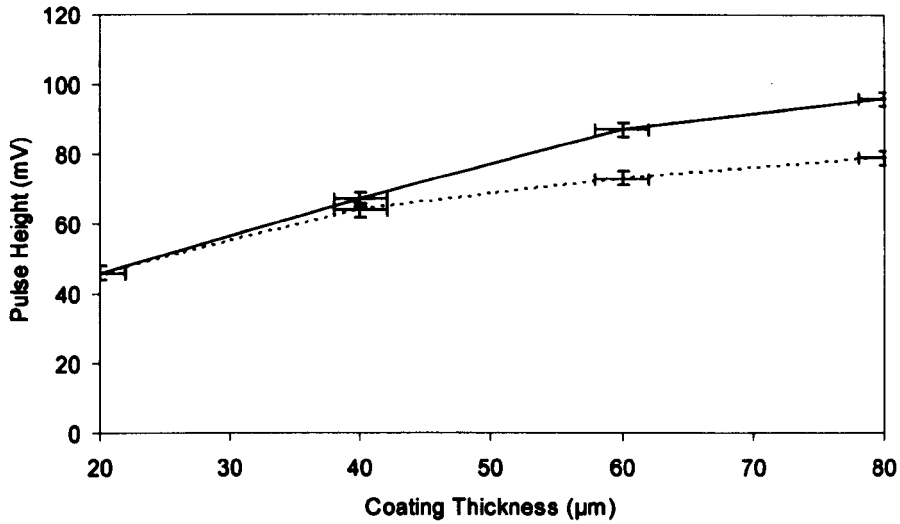


Fig. 4.22: Performance of small coated light guide (solid line – 100mm from PMT, dashed line- 250mm from PMT)

Results for the BBQ doped solid acrylic (Plexiglass GS2025) in Fig. 4.23 show a roll off in performance of over 20% down the length of the light guide, with an improvement of between 13% and 24% achieved by the addition of a foil reflector to the end opposite the PMT. The attenuation figures are comparable to results from similar studies [68, 69].

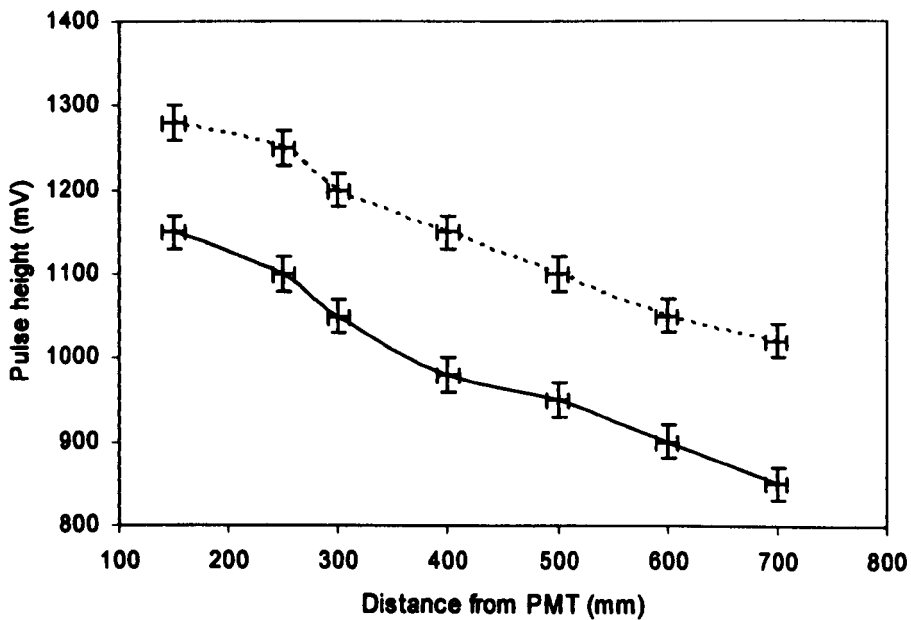


Fig. 4.23: Performance of Plexiglas GS2025 light guide (solid line – no reflector, dashed line- foil reflector)

A number of techniques for applying the reflective layer were tested with both solid guides (SG) and coated bar (CB), including white paint and aluminised foil. Results for these are shown in Fig. 4.24.

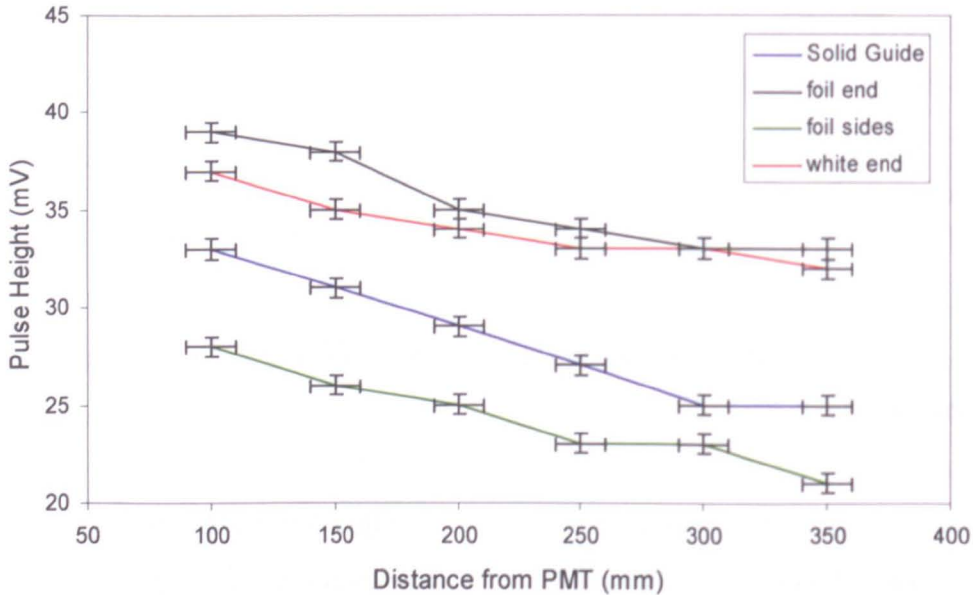


Fig. 4.24: Attenuation of light in solid light guides (tested with 450 nm LED)

Attenuation tests of the short coated light guides were reasonably encouraging, see Fig. 4.25. However further tests carried out with 1 m long, 10 mm diameter rods were less promising. Here it was found that an unacceptable level of attenuation occurred (up to 50%) over the length of the rod, Fig. 4.26. Furthermore the efficiency of the fluorescent layer was clearly less than ideal, as can be seen from the increase in signal strength for thicker layer of coating. For short guides, the performance of the low cost, commercially available, fluorescent green acrylic (Fig. 4.25) far exceeds all other combinations.

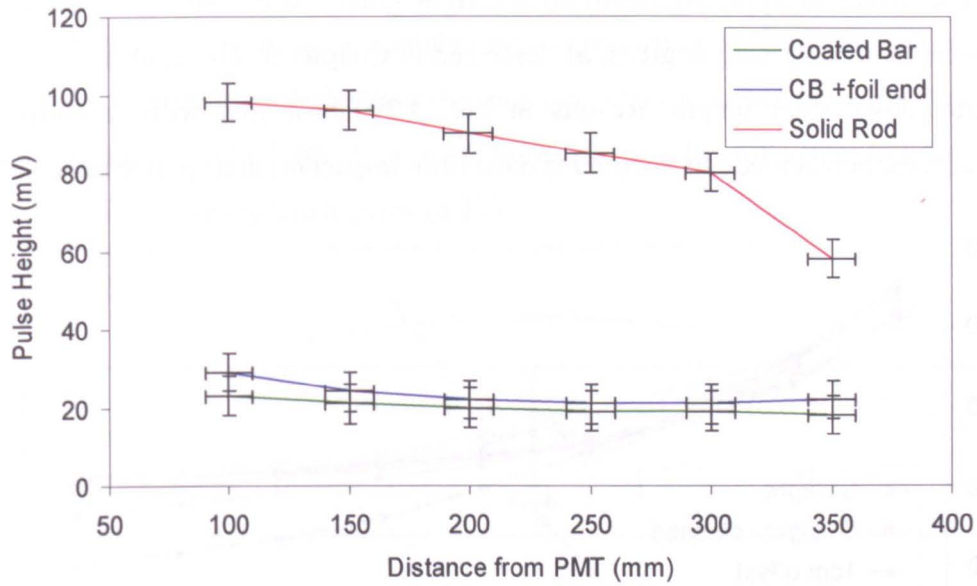


Fig. 4.25: Attenuation of light in coated light guides (tested with 450 nm LED)

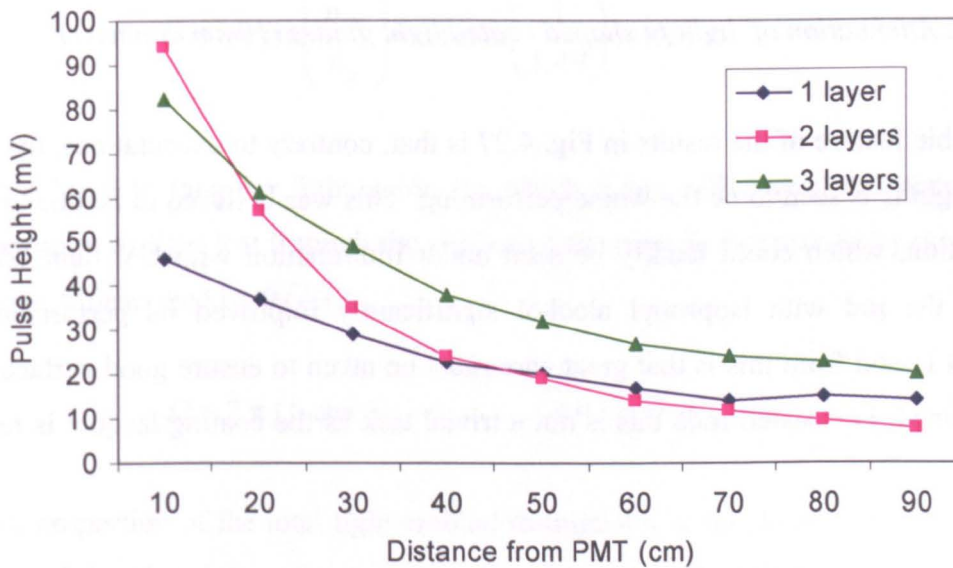


Fig. 4.26: Attenuation of light in long coated light guides (tested with 450 nm LED)

It is believed that the relatively poor performance seen in the coated guides is primarily due to surface imperfections, due to a lack of toughness in the coating material. It is also possible that the coating solvent (toluene), which is known to be somewhat aggressive, has attacked the acrylic substrate, further degrading performance.

The effect of applying bends to the light guides was also investigated. Coated guides were bent to varying degrees, as described in Chapter 5. The guides were tested for attenuation down their length. Results in Fig. 4.27 show that with carefully formed smooth curves, bends made to the guides have little impact on their performance.

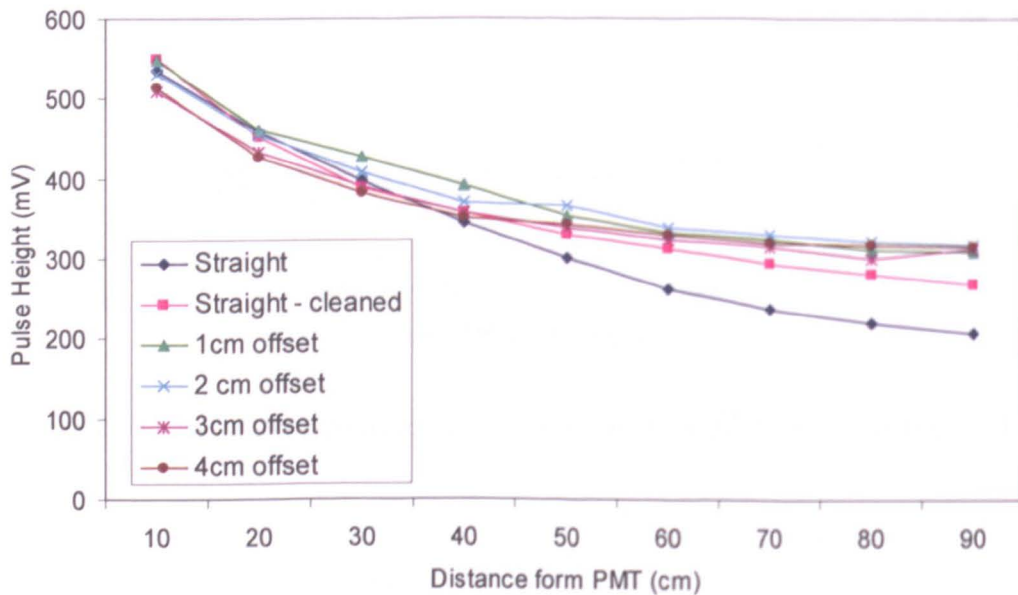


Fig. 4.27: Attenuation of light in shaped coated light guides (10mm diameter)

One notable feature of the results in Fig. 4.27 is that, contrary to expectations, the straight (unbent) guide is seen to be the worse performing. This was believed to be due to surface imperfection, which could readily be seen under illumination with UV light. Carefully cleaning the rod with isopropyl alcohol significantly improved its performance. An important lesson from this is that great care must be taken to ensure good surface quality is maintained. For coated rods this is not a trivial task as the coating lacquer is relatively soft.

## 4.8 Detector geometry

Due to the significant reduction in light output predicted from the BN:ZnS layers in comparison to the  $^6\text{LiF:ZnS}$ , it is important not only to use the light guides with the optimum fluorescent properties, but also to choose the best geometry to ensure maximum light collection and transmission to the photomultiplier tube.

If it is assumed that blue light entering the acrylic light guide, shown in Fig. 4.28, is absorbed and re-emitted isotropically, then a proportion of this light will be trapped in the acrylic by total internal reflection, the angle at which this occurs  $\theta$  is calculated from the refractive index of the light guide medium  $n_g$  (for acrylic, refractive index = 1.49) relative to that in air  $n_{\text{air}}$ , using Snell's law (4.12).

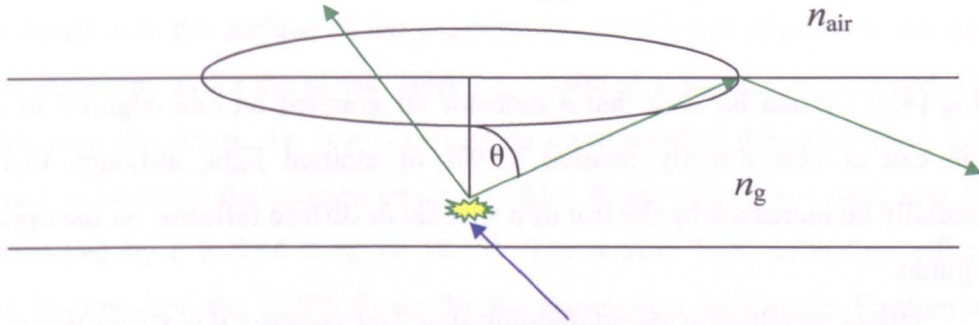


Fig. 4.28: Incoming light (blue) captured by fluorescence (green) and total internal reflection, in a planar wavelength shifting light guide.

$$\theta = \arcsin\left(\frac{n_{\text{air}}}{n_g}\right) = \arcsin\left(\frac{1}{1.49}\right) = 42^\circ \quad [4.12]$$

For a large rectangular light guide (in which many reflections will occur), in air, the proportion of light lost through the surface of the plate is determined by the solid angle of a cone  $\Omega$  described by  $\theta$  (4.13).

$$\Omega = 2\pi(1 - \cos\theta) = 0.51\pi \text{ sr} \quad [4.13]$$

As a proportion of the total light emitted through  $4\pi$  sr this is:  $0.51/4 = 0.13$ , taking both faces of the plate into account we can therefore say 26% of light will be lost, or 74% of light is trapped in the plate. For materials with a refractive index greater than  $2^{1/2}$  a proportion of light will not escape from any face of a parallelepiped, in this case the fraction of trapped  $F_t$  light can be calculated equation [4.14] [145].

$$F_t = 1 - \left(\frac{\sqrt{n^2 - 1}}{n}\right) \quad [4.14]$$

From [4.14] the proportion of light emitted from any face can be calculated as  $1-F_t$  and the fraction emitted from any one face  $F_x$  can be calculated as  $(1-F_t)/6$ . As shown in [4.15]

$$F_x = \frac{(1-F_t)}{6} = \frac{\sqrt{n^2-1}}{6n} \quad [4.15]$$

Using [4.15] it can be seen that a detector air coupled on one edge of an acrylic light guide can at best directly receive 12.9% of emitted light, although this figure can potentially be increased by the use of a specula or diffuse reflector on the opposite face of the guide.

Direct coupling of the photomultiplier will improve this figure due to a matching of refractive indexes. However where a mismatch in area occurs this is not possible without the use of alternative coupling mechanisms such as compound parabolic collectors, the most common of which is the Winston Cone [108], and fish tails; Fig. 4.29. Both of these options, while being relatively efficient, are bulky, expensive and difficult to manufacture.

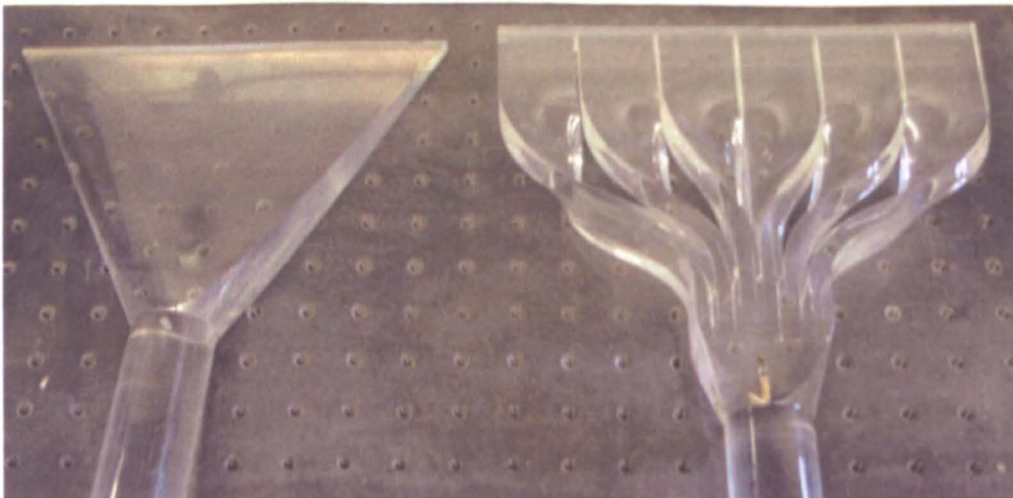


Fig. 4.29: Plain fish tail (left), and twisted fish tail light guide, for coupling large rectangular light guide / scintillating plates to a photomultiplier.

Compounded with these geometric factors are efficiency of the fluorescent compound, re-absorption of light, and losses due to impurities and surface imperfections in the acrylic.

An alternative approach would be to use a cylindrical light guide, as represented in Fig. 4.30. In the first instance it could be assumed that light emerging from the end of the cylinder would be described as in [4.13] however if the cylinder is directly coupled to a material of similar refractive index, it must be considered differently. In this geometry, light produced near the surface of the substrate ( $r_1 \ll r_2$ ) will react with the surface in much the same way as for the planar guide i.e. 12.9% of light reaching the end. However light from near the centre ( $r_1 \approx r_2$ ) cannot be considered in this way. Here it is more appropriate to consider the capture angle  $\varepsilon = 90 - \theta$ : for acrylic  $\varepsilon = 48^\circ$ , and the solid angle described by  $\varepsilon$  is  $0.66 \pi$  sr, or 16.5%. The overall light collection efficiency is therefore improved on the 12.9% figure for the rectangular light guide. Furthermore it is believed that rods can be bent and shaped much more easily readily than plates, to allow optimum use of the surface area of the photomultiplier. As such cylindrical guides are well worth considering as an option, where light collection efficiency is of paramount importance.

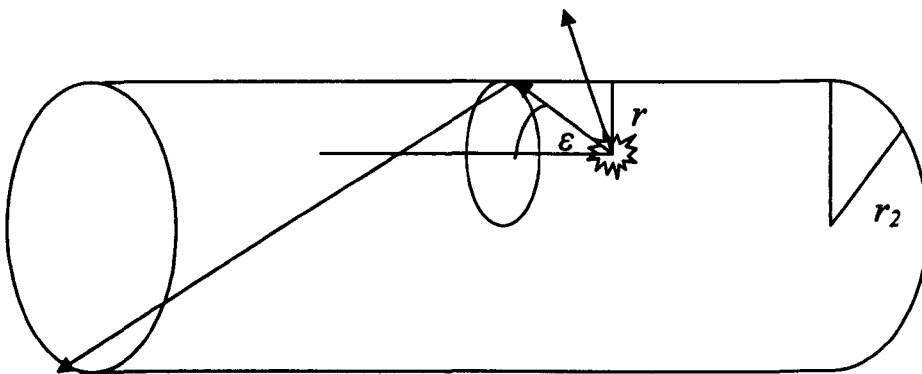


Fig. 4.30: Light trapped by a cylindrical wavelength shifting light guide.

Test carried out on the shaped light guides shown in Fig. 4.21 suggest there is little degradation in performance caused by the bending. This is consistent with Lukasz[109], who concluded that bends of up to  $180^\circ$  are achievable, if the ratio of bending radius to rod radius is at least 10:1.

## 4.9 Conclusions

Through the process of investigations described here the following decisions were made regarding the design of the new detector:

1. Hexagonal boron nitride was selected as the neutron capture compound
2. ZnS:Ag (GL47-NS1 grade) was selected as the scintillating compound
3. Solid acrylic wavelength shifting light guides are preferred over coated guides, with cylindrical rods offering the best coupling potential

Furthermore it was decided that two detectors would be constructed: One employing rectangular BBQ doped acrylic light guides, and detector housing salvaged from a previous PNL detector. The second detector was to use light guides made from commercial grade fluorescent acrylic rod, a new purpose made housing, and geometry optimised for maximum light collection. The design decisions and techniques employed in the manufacture of these detectors is examined in Chapter 5.

# Chapter 5

## Manufacture of BN based detectors

### 5.1 Introduction

Despite the background research, modelling, and laboratory testing (described in Chapters 1- 4), a number of unknowns still existed with regard to the development. Specifically, although there was confidence that a significant proportion of neutrons will be captured in the detector, and of these a number will generate a reasonable level of scintillation light, in the geometry of a large detector it is unknown how much of this light will reach the photomultipliers, and whether the signal produced can be readily and reliably distinguished from background noise. To evaluate the effect of geometry on light collection efficiency, two detectors were therefore manufactured; one based on planar light guides, the other on cylindrical rods. The main design points and manufacturing processes involved in the production of these two detectors are detailed in this chapter.

### 5.2 Selection of binders and solvents

Once BN and ZnS:Ag were selected as the preferred candidates for active ingredients in the coating layers (Chapter 4), test samples could be produced to assess physical and optical properties of the coating. As well as the above active ingredients the final constituent part of the coating “paint” is a suitable binder material. This binder must be:

- Stable for prolonged periods across a an operational temperature range from -10 to +50 °C, and in the presence of moisture,
- Non-reactive with active ingredients or substrate material,

- Suitable for use in minimal quantities to reduce the probability of interaction with the boron neutron reaction products.
- Useable over an appropriate working and setting time to allow sheets to be prepared and used in a realistic time scale
- Free from aggressive or harmful solvents, requiring special handling
- Readily stored and ideally suitable for recovery and re-working, to minimise waste

The previous Barton PNL detector [17] utilised a catalytically activated clear silicone polymer as the binder (Sylgard® 184 manufactured by Dow Corning). Other neutron screens have been produced with epoxy binders [42,53]. While both these materials have proved effective in manufacturing robust detectors, as thermosetting plastics they are messy to handle and wasteful, as excess material can neither be stored or reused. Furthermore due to their high viscosity these resins are required in a relatively high ratio of binder to active ingredients, e.g. 1:3 for the PNL detector. In such quantities it is reasonable to expect a significant proportion of the energy of the neutron reaction products (up to 25%) is being lost in the binder. Thermoplastics such as Lucite and PMMA have also been used in the past, however these are even more troublesome to manufacture as they need to be hot pressed.

Two alternative binder materials have therefore been investigated; PVA and a co-block polymer with the trade name Kraton® [110]. Some properties of these materials are shown in Table 4.9. Benefits common to both of these materials are that they set through an evaporation process (allowing recovery and recycling), that they are readily mixed with common solvents (for control of viscosity), and can be stored for extended periods (reducing wastage once a batch has been prepared).

Type	Common name	Product name	Manufacturer	Solvent	Setting time	Density gcm <sup>-3</sup>
Polyepoxide	Epoxy		numerous	-	30 min	1.6 – 2.1
Silicone polymer		Sylgard - Qsil	Dow Corning	-	30 min	1.6 – 2.0
Poly Vinyl Acetate	PVA	Builders /wood glue	B&Q etc	Water	1 hr in air	1.2 – 1.3
Styrenic Block Copolymer	SBC	KratonD SIS	Kraton®	white spirit	30 min in air	0.93

Table 5.1: Properties of binder agents (data taken from manufacturer data sheets)

Coated samples were prepared using both these binders with a ZnS/BN mixture. The Kraton<sup>®</sup> used was supplied in solid form and required dissolving in white spirit (typically 1 part Kraton to 9 parts white spirit by weight). This process was speeded up by gentle warming. PVA was supplied as a viscous liquid which could readily be diluted with water. Evaporation tests revealed that as supplied PVA contained 64% water; this was increased to 82% (leaving 18% PVA resin) to produce a viscosity similar to the Kraton. Mixtures were produced with ZnS/BN to binder (excluding solvent) ratios varying from 5:1 to 20:1 for both binders.

To test for flexibility, robustness, cracking and full encapsulation of the solids, paint samples were spread onto a Mylar substrate, to a thickness of approximately 100µm, using a small doctor blade, and were then left to dry at room temperature. Once dry the samples were examined. It was found that both binders performed well up to a powder to binder concentration of 10:1, after which de-lamination and cracking occurred. It was however felt that as the Kraton is re-soluble (where as the PVA is not) in the long term this would provide a more cost effective solution. Additionally the use of Kraton as the main binder allows PVA to be applied as an over coating, as Kraton is not soluble in water. An over coating was discovered necessary in the development of the PNL detector to prevent contamination by alpha emitting Radon daughters.

For evaluation purposes mixtures were prepared with both cubic and hexagonal BN, however for the final detectors Hexagonal BN was selected on both cost and performance grounds (Chapter 4). To produce a thoroughly homogeneous mixture a high speed hand blender was used to agitate the paint mixture for several minutes. The coatings were produced with the following formula by weight;

2 BN : 8 ZnS(Ag) : 1 Kraton : 10 White Spirit

Aluminised Mylar (100 µm thickness) was chosen as the backing for the scintillating layers due to its good mechanical and optical properties and ready availability. The relatively rigid Mylar was found to be easier to handle than thinner films.

### 5.3 Coating techniques

Both for testing and detector manufacture smooth even layers of the coating mixture are required in thicknesses from 50 to 200  $\mu\text{m}$ . For the small quantities required a Doctor blade technique [111] was chosen, as the best means for applying coatings. This method involves an apparatus which suspends a spreading blade a fixed distance above the surface to be coated. A pool of paint pored onto the surface can be evenly distributed by smoothly sliding the suspended blade across the surface. A precision vacuum bed, with automated pusher bar was used in conjunction with an adjustable doctor blade assembly, to produce test samples of a repeatable thickness and consistent quality. Fig. 5.1 shows the coating equipment with a prepared sample on the bed.



Fig. 5.1: *Vacuum bed and Doctor blade assembly, with coated sample institute*

An ultrasonic thickness gauge and precision micrometer were used to verify the thickness on test samples produced, and to determine appropriate settings for the doctor blade, see Fig 5.2. While these measurements suggest a reasonably linear relationship between doctor blade setting and finished thickness, the ultrasonic gauge appears to be less reliable as a measure, possibly due to coupling problems. For all subsequent results micrometer measurements were therefore used.

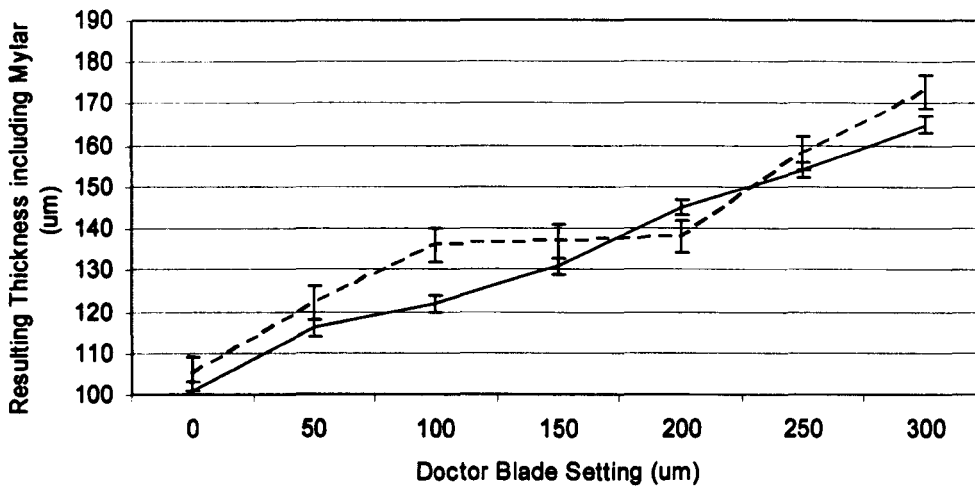


Fig. 5.2: BN "paint" - coating thickness measured against Doctor blade setting (dashed line measurements taken with ultrasonic probe, solid line micrometer measurement)

The vacuum bed was however found to be restrictively small for the manufacture of the larger coated sheets needed for the manufacture of detectors. For this stage of the work it was replaced with a toughened glass plate 1.2 m long, to which Mylar sheets were attached with adhesive masking tape.

## 5.4 Design of the two new BN/ZnS based detectors

In order to streamline the development process, it was decided that two detectors should be constructed in parallel. While both these detectors were to employ the same principles of: neutron capture, scintillation and wavelength shifting light collection, the geometrical layout of the two units was to be significantly different.

The first detector was almost exclusively manufactured from parts taken from the previous PNL  ${}^6\text{LiF}:\text{ZnS}$  development, with the notable exception of the neutron capture / scintillating layers which were replaced with the new BN:ZnS mixture. The detector uses a laminar construction, employing eight BN:ZnS layers, four large rectangular light guides, and three slabs of moderator, in very much the same configuration as that shown in Fig. 2.1 and 2.2. The light guides were air coupled to two 135 mm photomultipliers. The whole assembly was supported by a light tight box fabricated from black polypropylene. The primary advantage of this detector construction was its speed of

production and simplicity, as it required little machining and was relatively straightforward to assemble and disassemble. It also provides a direct performance comparison with the  ${}^6\text{LiF}$  detector.

The second detector was constructed using a completely different geometry, employing cylindrical rod light guides. As such this unit shares little with the design of the first detector, with the exception of the BN:ZnS mixture.

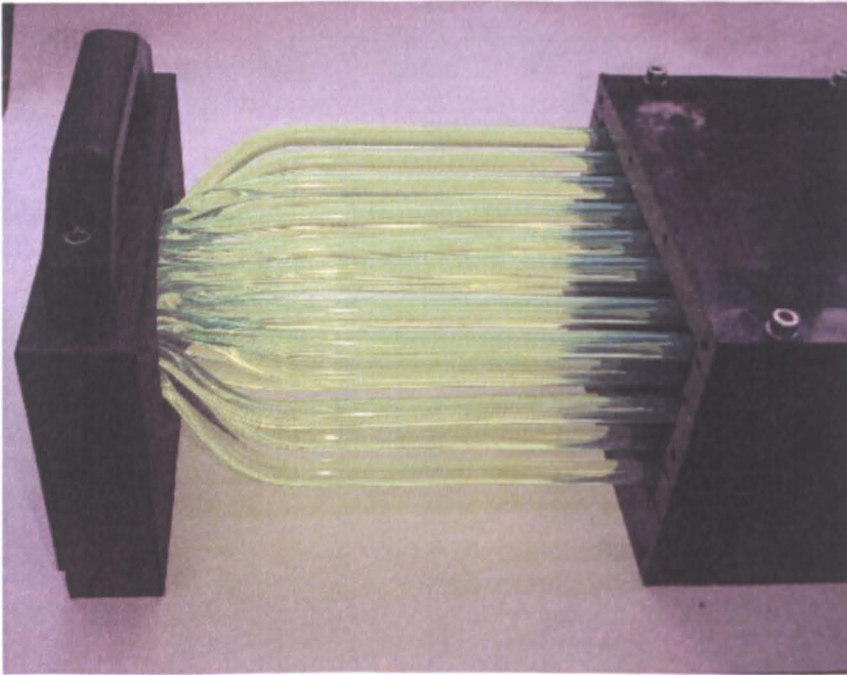


*Fig. 5.3: Rod based detector during assembly (all 24 wavelength shifting light guides partially exposed)*

There were several reasons why rods were chosen for this detector against the previously used rectangular plates; Firstly it was found through Monte Carlo analysis (section 3) that by distributing the neutron capture agent throughout the moderator, in a more homogeneous manner, sensitivity could potentially be improved. Furthermore by wrapping the scintillating layer in a tube around the rod, a 50% increase in surface area of neutron capture agent and scintillator can be achieved. Thinner layers can therefore be used, resulting in more light for each neutron capture event, and therefore improved noise rejection and gamma discrimination. It was also felt that improvements in light guide coupling could offset the significant reduction in light yield calculated for BN:ZnS, compared to  ${}^6\text{LiF:ZnS}$  (Chapter 4). Finally on commercial grounds, problem with

sourcing planar light guides of the appropriate thickness and doping made them unattractive as a component in what is intended to be a low cost system.

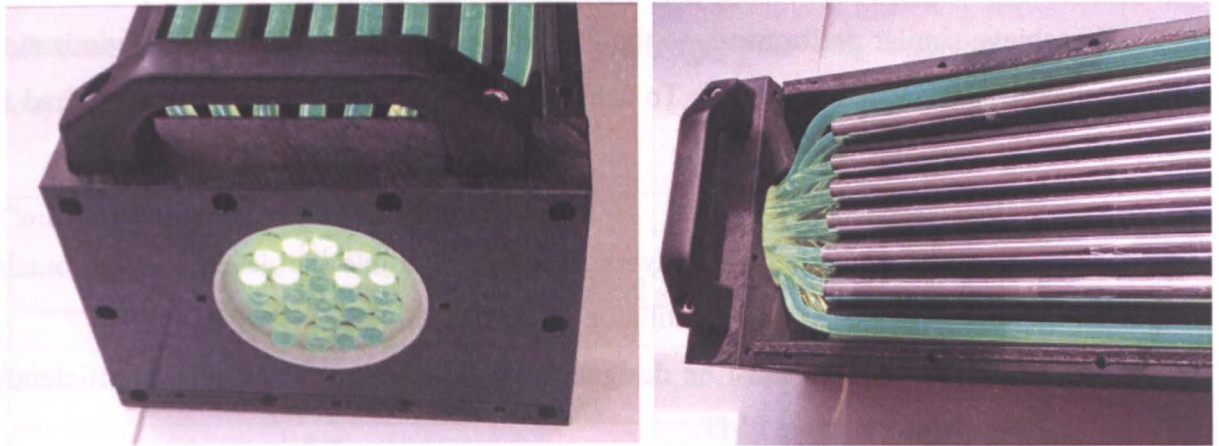


Fig. 5.4: Rod based detector during assembly (on the left the ends of the light guides can be seen illuminated by ambient light, on the right foil backed BN:ZnS tubes have been inserted over several of the rods)

Another key design decision for the rod based detector, and a deviation from the PNL detector, was the use of only one photomultiplier (PMT). The PNL detector used two 135 mm diameter PMTs mounted at opposite ends of the light guides. In this configuration spurious counts could be reduced by using a coincidence signal generated from both PMTs to trigger photon counting. This was potentially beneficial in a very low background application. However quotes for suitable 135 mm PMTs revealed a cost per tube of £960 (2010 prices). As two such tubes would represent a significant proportion of the overall cost of the detector, investigation of an alternative approach is well worthwhile.

Light guide testing (Chapter 4) revealed that light collection efficiency could be increased by replacing one tube with reflectors to send light back down the light guide. Furthermore as the light guides in the PNL detector cover less than 50% of the surface of the PMT it should be possible to significantly reduce the size of the PMT by more efficient light guide coupling. As tube noise is roughly proportional to photocathode surface area, replacing two large PMTs with one smaller one also reduces dark count by a factor of approximately 5.5. If sufficient light can be delivered to the PMT, with the use of appropriate discrimination techniques, and with a lower noise level, the necessity for two PMTs could be removed. A single 75mm tube of similar sensitivity to the 135mm

tube is available for £490 (2010 prices), representing a saving of at least £1400 over the PNL design.

To achieve similar performance to the PNL detector with only one PMT optimization of optical performance is essential. To achieve this, two factors were clearly required from the architecture of the detector.

1. To keep the scintillating layers as thin as possible the detector must contain as large a surface area of scintillator as is practical.
2. The light guides must be designed to collect and conduct light as efficiently as possible to a single PMT.

## 5.5 Optical coupling of light guides

Optical losses between the light guides and photomultiplier are potentially a significant contributor to the overall degradation of the signal generated by a neutron capture, and could therefore hamper discrimination techniques. A series of tests was carried out to assess the importance of optical coupling, using a short piece of wavelength shifting acrylic excited by a blue (450 nm) pulsed light emitting diode (LED), and a 135 mm diameter photomultiplier. A schematic of the apparatus used for this test is shown in Fig. 5.5.

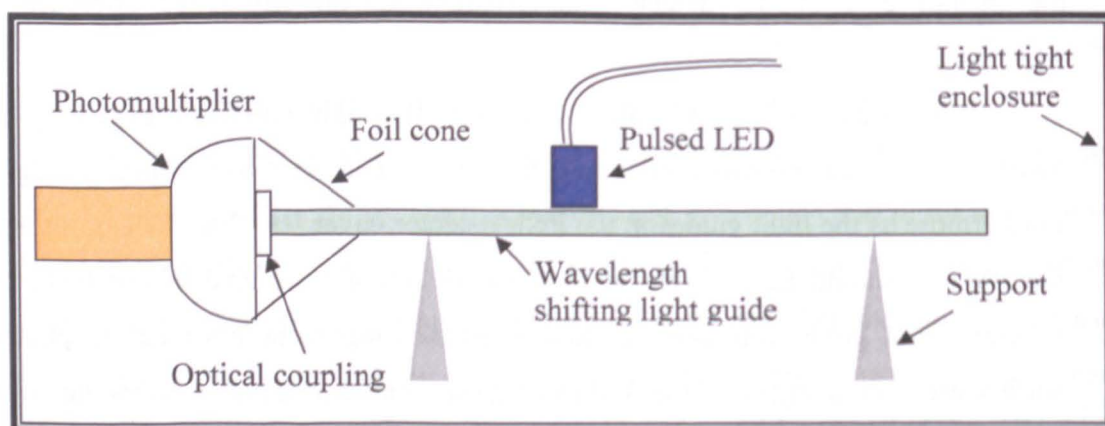


Fig. 5.5: *Optical coupling tests between light guide and photomultiplier*

Results in Table 5.2 show not only the smallest air gap having a marked effect, but also that increasing the air gap increases the losses. This is presumably due to divergence of light as it leaves the end of the light guide. Table 5.2 also shows that use of a reflective foil cone between the light guide and the photomultiplier only marginally improved coupling performance.

<b>Coupling Distance</b>	<b>Coupling medium</b>	<b>Peak signal (mV)</b>
0	Optical coupling gel	67
0	Sylgard 184 pad + Optical gel	60
0	Air	44
1	Air	37
5	Air	22
8	Air	18
1	Air + Reflective Cone	36
5	Air + Reflective Cone	30
8	Air + Reflective Cone	25

Table 5.2: *Optical coupling losses between light guide and photomultiplier*

A mismatch between the surface area of the end of the light guides and that of the photomultiplier, shown in Fig. 5.6, is a significant source of light loss in the laminar detector. Of the 103 cm<sup>2</sup> sensitive surface area of the EMI 9791 photocathode, only 34 cm<sup>2</sup> is directly in line with a light guide, leaving 30 cm<sup>2</sup> of light guide out of alignment with the photomultiplier. Although techniques exist to mitigate losses from such an interface (section 4.4) space limitations within the detector significantly limit the possibilities to improve on the air coupling used in the PNL unit. However, as in the PNL detector, a small foil backed cone was constructed to channel as much scattered light as possible into the PMT. The ends of the moderator blocks were also coated in reflective foil for the same purpose.

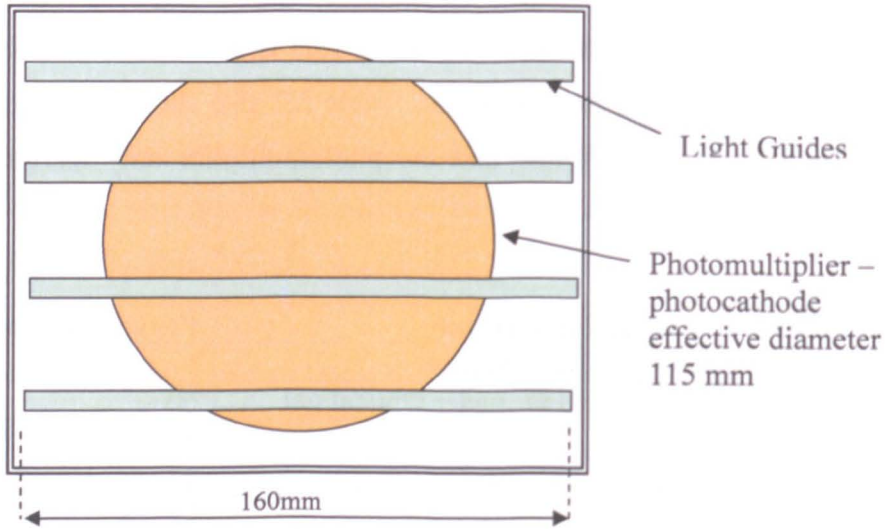


Fig. 5.6: *Size mismatch between laminar light guides and photomultiplier*

The problem of providing an efficient, close coupling between photomultiplier and light guides was readily overcome in the rod based detector by applying bends to the rods. When heated the rods could be readily manipulated to produce smooth curves suitable to channel light from a distributed matrix to a relatively small collection point. This not only improves light collection efficiency but also ensures effective use of the available surface area of the photomultiplier photocathode. As the price of a photomultiplier is roughly proportional to its diameter this can represent a significant cost saving. Solid fluorescent acrylic rods 10 mm in diameter were selected for the final design, in preference to coated rods shown in Fig. 5.7. As well as being cheap and readily available these were found to perform extremely well as a wavelength shifter. They also had excellent robustness; an essential quality as surface finish is critical to the efficiency of the light guide.



Fig. 5.7: *Bent coated light guide rods.*

To accurately form the bends in the rods four curved channels were machined into a sheet of medium density fibreboard (MDF) to act as templates; although 24 light guides were employed in the detector the layout was designed to require only four different offsets, as shown in Fig. 5.8. A hot air gun was used to heat the section of rod required for bending. The bend was then achieved by pushing the rod into the appropriate channel of the former, and letting it cool. Each rod was then polished on a buffer wheel to remove any surface blemishes.

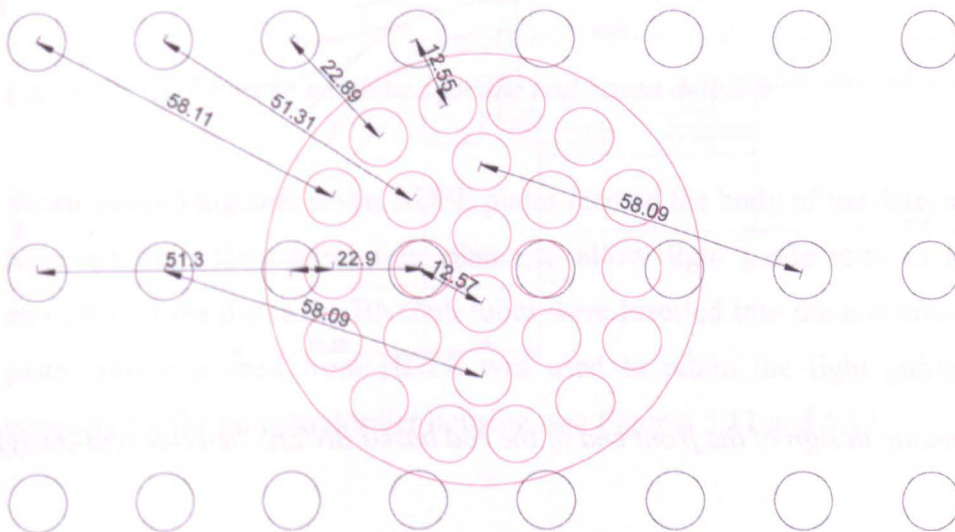


Fig. 5.8: Relative position of the light guides, in the moderator matrix (black), and at the photocathode (red), arranged to require only 4 different formers.

To provide a close optical interface between the rods and the PMT a circular dish was machined from white polyethylene, to the diameter of the PMT, see Fig. 5.11. The ends of the light guide rods were fitted to snug holes drilled in the base of the dish. The dish was then filled with a compressible optically clear silicone resin, to which the PMT could be securely coupled.

## 5.6 Rod detector mechanical assembly

A schematic drawing of the front end of the rod detector assembly is shown in Fig. 5.9. The photomultiplier (shown in blue) is housed within a turned aluminium assembly,

bolted onto the machined polyethylene structure housing the light guides and scintillating layers.

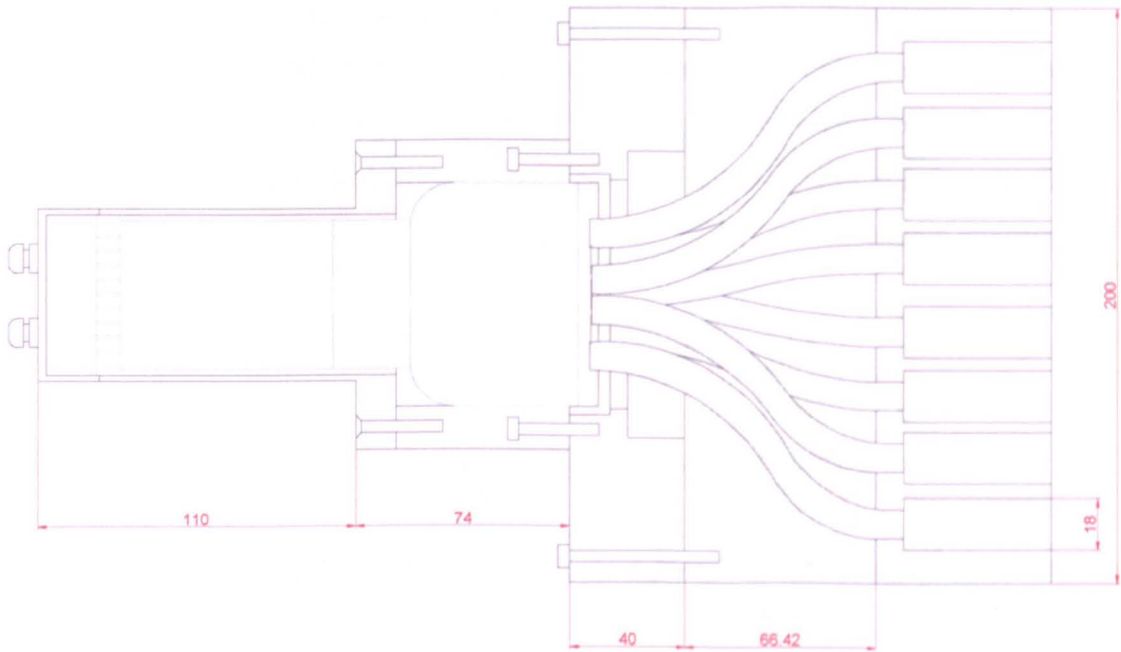


Fig. 5.9: Schematic design of the front end of the rod based BN/ZnS detector (cut-away).

The BN:ZnS layers used in this detector were produced in the same way as previously described. However when dry the coated Mylar sheets were first cut into strips, and then formed into tubes, using a cylindrical former (with the scintillating mixture facing inwards). The tubes were held together with adhesive tape, and could then be removed from the former.

High density polyethylene (HDPE) slabs were selected for the body of the detector, chosen to optimize the amount and distribution of moderator, and to reduce component count and cost. HDPE is not only cheap, easily machined and relatively stable [112], but it also has the high proportion of hydrogen ( $H_6C_3$ ) desirable in a moderator. To distribute the BN:ZnS layers and light guides within the moderator, semi-circular grooves were machined into the HDPE, as shown in Fig. 5.10.

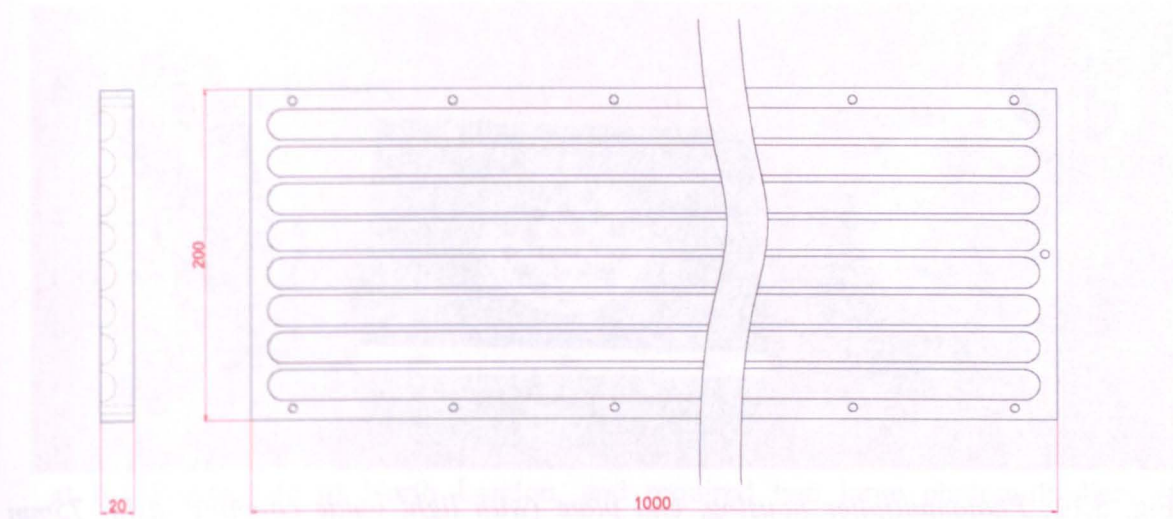


Fig. 5.10: HDPE slabs machined for the rod based detector

When stacked together seven HDPE plates formed the body of the detector. A section was removed from the central four plates to allow light guide rods to be fitted. During assembly of the plates the BN:ZnS tubes were inserted into the machined grooves. An end plate, also machined from HDPE was used to retain the light guides and provide a coupling for the photomultiplier housing, see Figures 5.11 and 5.12.

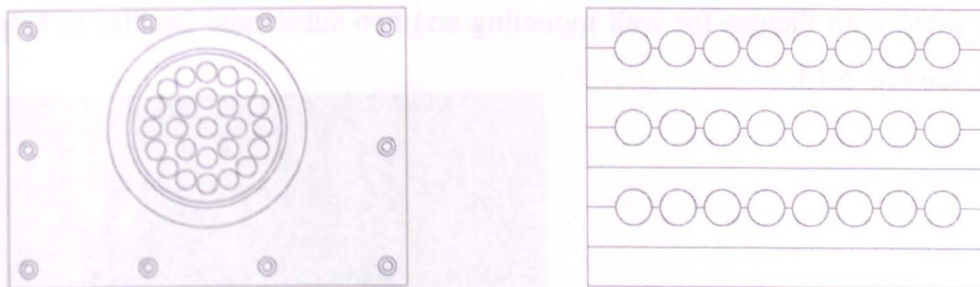


Fig. 5.11: HDPE slabs stacked together, and light guide coupling plate

In order to maintain the light tight integrity of the enclosure, all interfaces were gasketed with adhesive foam strips. All components were held together with stainless steel nuts and bolts, for strength and environmental integrity, and to allow ready access for re-work.

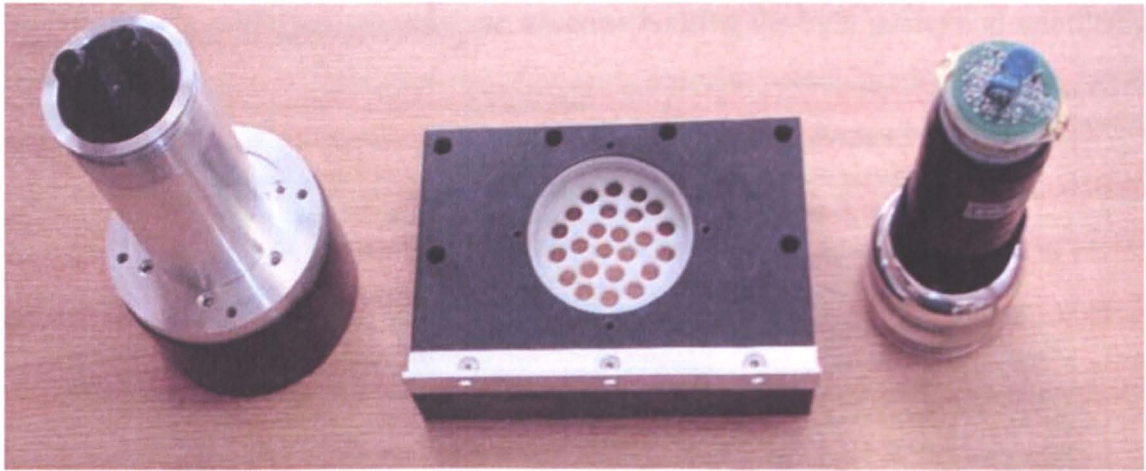


Fig. 5.12: *Photomultiplier housing, end plate (with light guide coupling dish), 75mm photomultiplier with voltage divider circuit attached*

The PMT housing, machined from aluminium, had a screw threaded collar fitted to the base. Once assembled this collar was tightened to ensure good contact between the PMT and the light guide interface. The voltage divider required to bias the PMT dynode chain was assembled from a modified printed circuit board (C638) supplied by Electron Tubes.

With an overall length of 1.25 m and a total weight of approximately 35 kg some consideration had to be given to the handling and installation requirements of the detector. As it was intended for testing in a variety of locations and orientations, the assembly was therefore fitted with flanges for wall mounting and two substantial handles to help with transport, see Fig. 5.13.

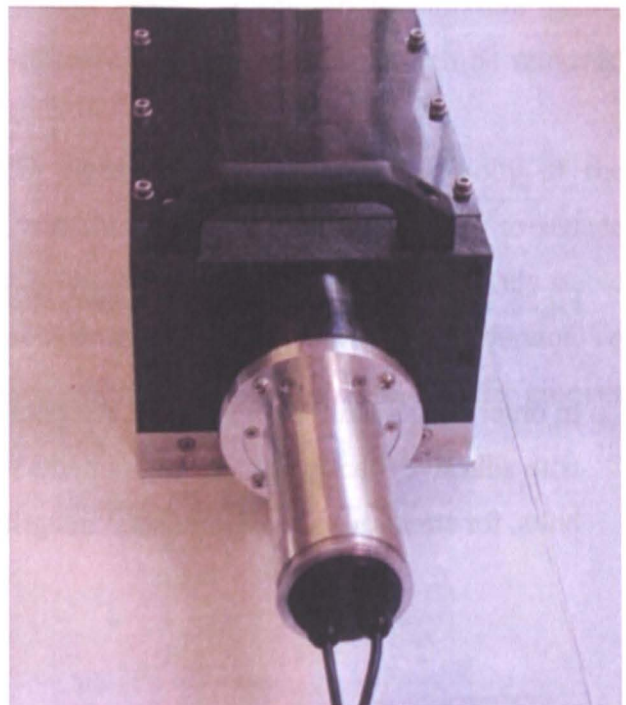


Fig. 5.13: *End view of completed rod detector assembly*

## 5.7 Conclusions

Two new large thermal neutron detectors were constructed both employing BN:ZnS in thin layers, wavelength shifting light guides, and photomultiplier tubes. The central difference between the two detectors was the geometry of the light guides, one utilising rectangular planar BBQ doped acrylic, the other using cylindrical fluorescent rods. The detector with planar light guides was closely based on a  ${}^6\text{LiF:ZnS}$  unit previous developed at the Polytechnic of North London, and required two large photomultipliers. This detector provides a simple test bed for the new neutron capture mixture, and a direct comparison to the PNL  ${}^6\text{LiF}$  detector. The rod based detector was a new design intended to function with a single smaller photomultiplier; using only commercial grade plastics and a single photomultiplier it offers significant cost savings over previous designs and with optimization of neutron sensitivity (through MCNP) and light collection efficiency (shaped light guides) it also offers the potential for improvements in performance. The successful implementation of these detectors require careful attention to signal processing and discrimination techniques, as discussed in the next chapter.

# **Chapter 6**

## **Pulse discrimination; techniques and implementation**

### **6.1 Introduction**

For most industrial applications thermal neutron detectors require a robust and reliable means of distinguishing neutrons from all other events occurring within the signal chain of the detector. This is particularly important in any application requiring both high sensitivity and a low background count rate. Due to the relative scarcity of neutrons in the normal environment and low radiated flux expected from illicit neutron sources (Chapters 1 and 3), neutron detectors developed for security systems face a demanding specification in terms of signal to noise levels, and in particular they must be capable of rejecting interference from gamma interactions. This chapter contains a discussion of the sources of noise within the ZnS:BN detector, a review of current techniques and equipment for performing neutron discrimination in similar detectors, and details the design of a stand alone system, for optimizing discrimination performance in the newly developed detectors.

## 6.2 Sources of noise within the BN:ZnS detector

Background noise can be described as any detected signal that produces no positive contribution to the measurement being taken. As such, in most circumstances, the noise acts to mask the target measurement. In this application sources of noise can be categorised as follows;

1. Neutron background
2. Gamma interference
3. Photomultiplier dark noise
4. Light leaks / Residual fluorescence

### 6.2.1 Neutron background

The first of these, neutron background, is a feature of the application, whereby naturally occurring environmental neutrons mask neutrons emitted by a target source. Although neutron screening around the detector can improve this background rate, as the detector itself has no real directionality or energy resolution, little can be done within the detector to mitigate the problem, with the possible exception of neutron showers. The main source of neutron background at or near the ground is through interaction of high energy cosmic rays, both in the atmosphere and at ground level, where they predominately interact with heavy nuclei. As these cosmic charged particles are known to often arrive as showers it is reported that neutron background can contain bursts of activity. Described as the 'Ship effect' by Kouzes [30], due to its increased prevalence in the presence of large high density objects e.g. shipping, in theory at least it can be reduced by gating out neutron events which are too close together. The US Department for Homeland Security specification for advanced spectroscopic portals (ASP) [34] requires an adjustable dead time of 0.1 – 100  $\mu$ s to counteract this effect. However a study by Heimbach [113] found no measurable phenomenon. If this is correct, introducing dead time will only reduce sensitivity.

In principal it may be possible to reduce neutron background through careful selection of materials in the vicinity of the detector, e.g. replacing the road surface with

compounds having high neutron cross section and minimal cosmic ray to n interactions. While a certain amount of conflicting work has been done attempting to characterize neutron background both through measurement and Monte Carlo modelling [114, 115], there is little or no evidence of attempts to reduce it. This is surprising given that background level has a direct correlation with the marginal sensitivity of detection systems; however as it is largely independent of detector design, attempts to manipulate the neutron background remain outside the scope of the current project.

## 6.2.2 Gamma rejection

Gamma interference is a more straightforward problem, whereby gamma rays absorbed by the detector produce a sufficiently robust signal for it to be wrongly interpreted as a neutron. This can occur by the absorption of a significant proportion of a single high energy gamma, or by multiple interactions occurring almost simultaneously, e.g. in an intense gamma field. A convenient way to express gamma sensitivity is; the proportion of incident gamma rays which produce a false neutron count, e.g.  $10^6$  gamma : 1 neutron

While immunity to gamma interference is desirable for many applications, it is particularly important for security systems. As gamma sources are much more prevalent than neutron sources (section 1.2), and as gamma background varies widely, “False Positive” gamma alarms are relatively common in portal systems; as such they are potentially dealt with less rigorously than neutron alarms.

Gamma rejection is inherent in the BN:ZnS detector to some extent. Due to the thin layers of scintillating material used only a small amount of energy can be deposited during a gamma interaction. With a density  $4.09 \text{ gcm}^{-3}$  ZnS has a reasonably short gamma attenuation length [116], which for gammas emitted by the majority of naturally occurring radioisotopes is dominated by Compton scattering. The rate at which energy is absorbed can be calculated from the mass energy attenuation coefficient of the material  $\mu_{en}/\rho$ , shown in Table 6.1. For Compton scattering this is dependent on electron density and is therefore proportional to the atomic number of the absorbing material.

Material	Atomic number	Mass attenuation coefficient $\mu/\rho$ (cm <sup>2</sup> /g)	Mass energy attenuation coefficient $\mu_{en}/\rho$ (cm <sup>2</sup> /g)
Zinc	30	$8.45 \times 10^{-2}$	$2.98 \times 10^{-2}$
Sulphur	16	$8.78 \times 10^{-2}$	$2.98 \times 10^{-2}$
ZnS		$8.61 \times 10^{-2}$	$2.98 \times 10^{-2}$

Table 6.1: *Gamma attenuation coefficients at 500 keV for ZnS. Data taken from NIST tables[116]*

For a typical layer thickness of 200 $\mu$ m, and with a ZnS content of 73%, the scintillating film will have a linear density  $t$  of ZnS =  $2 \times 10^{-2} \times 0.73 \times 4.09$  g/cm<sup>2</sup> = 0.06 g/cm<sup>2</sup>. The proportion of gamma energy absorbed by this layer  $E$  is given in equation [6.1]:

$$E = 1 - e^{-t(\mu_m/\rho)} \quad [6.1]$$

$$E = 1 - e^{-(0.06 \times 0.0298)} = 1.79 \times 10^{-3}$$

Therefore less than 0.2% of 500 keV gamma impinging on each scintillating layer is converted to fluorescent light. At a  $\gamma$  conversion efficiency of 13% (Section 4.4) this equates to an average of 43.8 photons of blue 450 nm (2.75 eV) light. For a gamma ray interacting with several layers of scintillation, or travelling at an acute angle to the surface of the layer, this could increase to several hundred photons. However this figure is still tiny when compared to a potential 2.31 MeV deposited in the scintillator in the form of charged reaction products (<sup>7</sup>Li,  $\alpha$ ) from a neutron capture in boron, which at a 8% conversion efficiency for  $\alpha$  equates to a burst of light having  $6.7 \times 10^4$  photons.

On the face of it discriminating signals several orders of magnitude different would appear to be trivial, however the figures above are for the ideal case. In the real detector there will be a significant proportion of neutron captures that result in only a small amount of the potential 2.31 MeV reaching the ZnS, with the remainder being absorbed by the BN, or binder, or escaping the surface. Attenuation of light in the ZnS:BN layer, and coupling losses to the light guide and the PMT, can also dramatically reduce the margin. Furthermore in ZnS(Ag) gamma scintillation occurs over a significantly shorter time scale than that produced by charged particles (<60 ns for a  $\gamma$  induced pulse to decay to 10% of its peak, up to 1  $\mu$ s for  $\alpha$  [46]). Fig 6.1 shows gamma

and alpha pulses recorded from a sample of ZnS(Ag), which are broadly in line with other studies [46]. Therefore a well coupled gamma event may occasionally produce a peak signal comparable in size to one generated by a heavily attenuated neutron capture. If optimum neutron sensitivity is to be achieved even the weakest neutron signals must be recognised and counted. And equally well a very high proportion of gamma must be rejected. Therefore while the benefits of inherent gamma immunity are clearly preferable, in any neutron scintillation detector it is unlikely that all potential for gamma interference can be completely removed. However where differences exist in the characteristics of the respective signals, in this case pulse decay time, signal processing can be used to further improve performance.

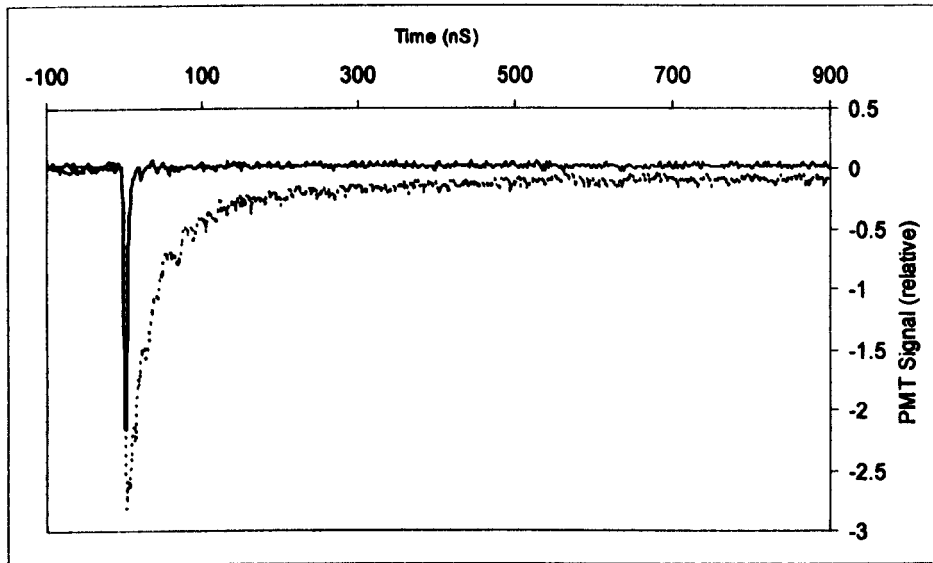


**Fig. 6.1:** *Alpha (dashed) and gamma (solid) induced pulses in ZnS(Ag), measured on a thin film scintillation detector close coupled to a photomultiplier. Gamma trace scaled up by a factor of 10*

It should be noted that, in very much the same way that papers have failed to agree on efficiency figures for ZnS, there is some confusion surrounding the decay characteristics of its emissions. A summary of research by Burk [22] concludes that ZnS:Ag excited by  $\alpha$ -particles has a complex decay following a quadratic hyperbolic law. Measurements made by Barton [97] produced similar findings with a good fit to the following equation for the period  $t > 0.5 \mu\text{s}$  :

$$I(t) = \frac{1}{(a+t)^\gamma} \quad [6.2]$$

Where  $\alpha = 1.1 \mu\text{s}$  and  $\gamma = 1.4$ . The decay has a slow component in excess of  $100 \mu\text{s}$ . For the fast component, below  $0.5 \mu\text{s}$ , Barton described the decay as exponential with a  $70\text{ns}$  time constant. This is certainly compatible with the trace shown in Fig. 6.1. Reliable data for gamma interactions in ZnS is however less available. Koontz [39] reported that a similar decay time to  $\alpha$  events was observed. However Legler [123] reported a  $20\text{ns}$  decay time for  $\gamma$  scintillation compared to  $200 \text{ ns}$  for  $\alpha$ . This disparity is possibly due to difficulties in coupling sufficient gamma energy into a thin layer of ZnS, to take accurate measurements. Furthermore the properties of ZnS (discussed in Chapter 4) vary widely dependent on the type and quantity of doping materials employed. In laboratory trials it was impossible to distinguish gamma events from photomultiplier background noise, by shape, as both appeared to be limited by the rise and fall time of the photomultiplier. For the purposes of this detector it is therefore reasonable to assume gamma fluorescence is only measurably present over a short period  $< 20 \text{ ns}$ . Whether this is due to a fast decay time, or the small amount of energy deposited, during gamma interactions, is not clear. However in either case techniques employing pulse shape can be used to improve immunity to gamma interference.

### 6.2.3 Photomultiplier dark noise

The term photomultiplier dark noise refers to all sources of spurious signals, generated within a photomultiplier, in the absence of, or in addition to, those produced by incoming light. The mechanisms by which these signals are generated range from spontaneous thermionic emissions, and after-pulses producing signals equivalent to single photons, through radioactive contamination, to cosmic ray interactions which generate particularly large pulses; see Fig 6.2. Dark noise is a complex area of research in its own right. Although it is described in depth by Wright [118,119], and others [120,121], some aspects such as after-pulses, and cosmic ray induced events [122] appear to be still not fully understood.

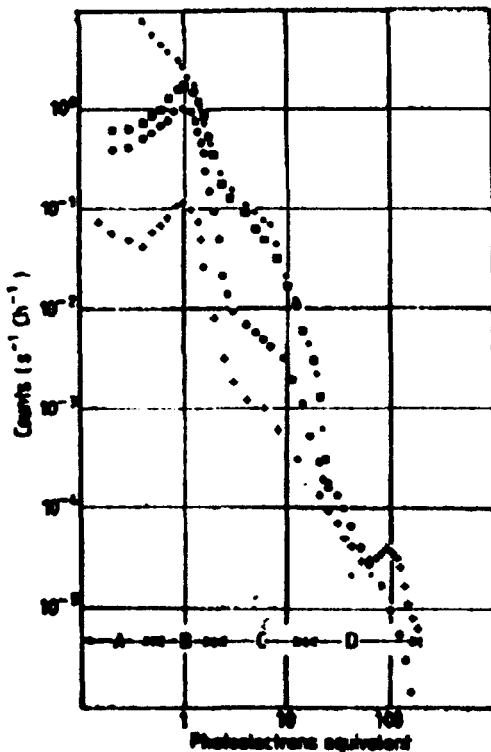


Fig. 6.2: *Background pulse height distributions for four photomultipliers at 20°C. The lower trace has a quartz window and is free from radioactive contaminant but shows a well resolved cosmic ray peak at 80 photoelectrons equivalent [118]*

The level of noise generated in a particular tube is influenced by several factors in its manufacture including; Photocathode composition, window material and thickness, operating voltage and temperature. It is also remarkably variable for photomultipliers of an apparently identical design (Fig. 6.2).

As thermionic emissions from the photocathode are the primary source of low level (single photon) noise pulses, reducing the area of the photocathode has a direct relationship to reductions in noise level; e.g. a typical 75 mm tube has a dark count of  $300 \text{ s}^{-1}$ , where as 130 mm tubes have dark count in excess of  $1000 \text{ s}^{-1}$ .

With regard to signal discrimination, while the low level signals are a problem for photon counting, the bigger problems are presented by higher intensity pulses produced by contamination and cosmic ray interactions. While these are characterised as rapidly decaying impulses (at the limit of the tube performance) it is believed that they produce delayed pulses up to  $100 \mu\text{s}$  after the initial event, due to fluorescence in the faceplate and excitation of the photocathode material. The timing of these after-pulses is similar to those

generated by ionisation of impurities following an impulse of light. Together they represent a source of noise which could potentially be most difficult to screen out.

#### **6.2.4 Residual fluorescence and light leaks**

Due to the long decay time of the characteristic ZnS emission (which has a complex decay with components of up to  $10\mu\text{s}$ ), potential over-counting caused by residual fluorescence in the ZnS must be taken into account when selecting parameters for discrimination circuits. While it is relatively straight-forward to introduce a dead time after an event, in high count-rate situations this can have a detrimental effect on sensitivity. For high count rate applications it may therefore be necessary to select a faster scintillator such as a grade of ZnS:Ag more heavily killed (with Ni) [72], or possibly ZnO. For low count rate applications such as security systems this however is not an issue. It should be noted that, due to very long decay in fluorescence in ZnS, it was standard practice to assemble experiments in dark room conditions, and where possible, to leave detectors for 24 hours after assembly before measurements were taken.

Any source of light leaks into the detector will raise the background noise level and therefore contribute to false counts. While this can be prevented by careful application of gaskets to joints etc., testing for light tightness is an important aspect of the setup and evaluation of the detector.

Other sources of noise such as microphonics, magnetic and electrical interference can best be reduced by careful design, i.e. screening cans for the electronics, Mu-metal foil around the photomultipliers, and anti-vibration damping etc. However the possibility of such interference must also be taken into account during testing.

An interesting observation made on the laminar detector was an increase in count rate, corresponding to the body of the detector being rubbed with a cloth (during cleaning). It is believed that this effect was in some way due by static build up in the plastic, although the precise mechanism by which it occurred is unknown. If this was found to be a recurrent problem, in field use, methods could be applied to prevent static build up, such anti-static coating.

### 6.3 Neutron gamma discrimination techniques

Pulse shape discrimination; whereby fast gamma pulses are distinguished from neutron pulses having longer decay time, are commonly employed in liquid organic scintillators, and to some extent plastic organics [22,23]. Developed by Gatti [135], it is based on the principal that, for many scintillating materials, the rate of decay of scintillation light varies according to the nature of absorbed radiation. It is particularly common in organic scintillators [88,90,95], but has also been reported in CsI [97] and ZnS [123]. The mechanism by which delayed fluorescent occurs is not fully understood, although it is believed to be due to the creation of long lived triplet states [22]. It is however known to be dependent on the rate at which energy is absorbed along the ionising track through the scintillating material  $dE/dx$ . Heavy charged particles (generated by thermal neutron capture) lose energy more rapidly than more penetrating  $\gamma$  radiation, see Fig. 6.3.

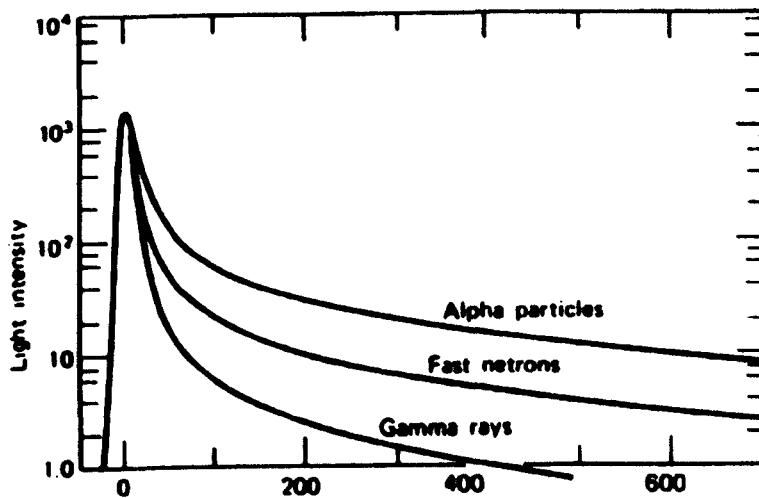


Fig. 6.3: *The time dependence of scintillation pulses in stilbene when excited by radiations of different types [136]*

Gatti's technique for pulse discrimination assumes that the response of a scintillator to two types of signal, such as alpha and gamma rays, was given by the number of photoelectrons in successive intervals of time,  $\alpha_i$  and  $\gamma_i$ . The signals are normalised by incoming energy, to be of equal pulse height, so that

$$\sum_i \alpha_i = \sum_i \gamma_i = N$$

where  $N$  is the total number of photoelectrons. It was proved that the optimum linear filter to provide discrimination of these signal was one that weighted the successive time intervals according to [6.3]

$$P_i = \frac{\alpha_i - \gamma_i}{\alpha_i + \gamma_i} \quad [6.3]$$

With a differentiating filter, whose time constant is selected to optimise this weighting, Barton [97] was able to achieved good neutron discrimination for CsI scintillators. The technique is relatively simple to implement with readily available analogue electronics modules, and is particularly effective on small detectors with good light collection. In some circumstances ZnS, with its long fluorescence decay time is well suited to application of this method, and has been reported to reduce background rate by at least a factor of 100 [117]. Even through a short wavelength shifting light guide it is possible that sufficient signal is produced to implement a simple pulse shape discrimination; Fig. 6.4 shows the pulse train for an  $\alpha$  source recorded on the light guide test rig.

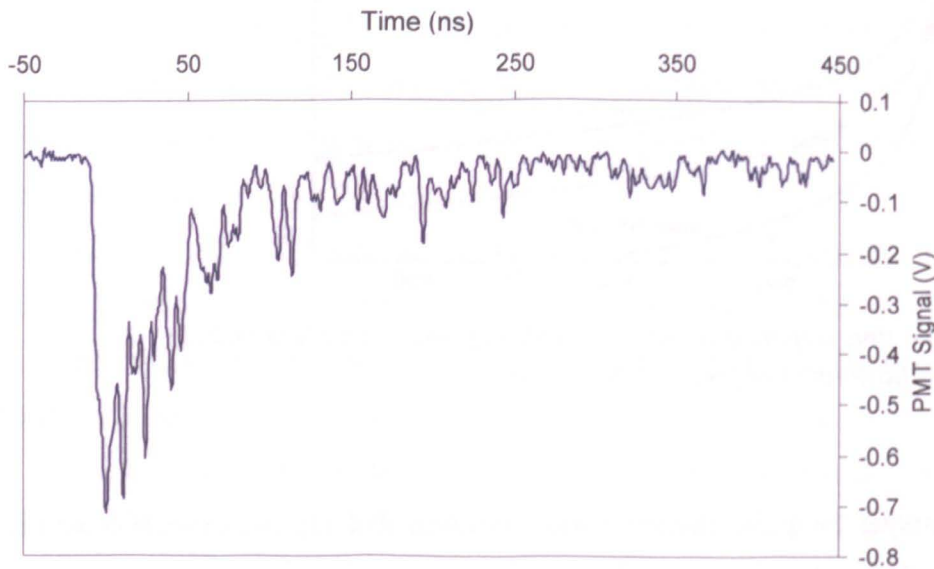


Fig. 6.4: Signal pulse train produced by ZnS(Ag) on 400 mm light guide with  $^{241}\text{Am}$   $\alpha$  source

However within the large BN:ZnS detector, self absorption in the scintillating layers, and inefficiencies in the coupling and transmission of light, from the point of scintillation to the photomultiplier, result in a greatly reduced signal, often amounting to

taken from the BN:ZnS rod detector irradiated by a  $^{252}\text{Cf}$  source. The delayed pulses seen here have a significant variation in size, possibly by as much as a factor of 10. It has been postulated that this is due to the delayed fluorescence in the ZnS releasing photons in bursts, although no evidence can be found for this in previous work. Alternatively these pulses all represent single discrete photons; the single electron response distribution of a high gain photon counting photomultiplier is well reported as having a baud distribution [131], depending chiefly on the gain of the first dynode stage, which produced a variation in pulse height of a factor of 5 or more. In some cases pulses occurring close together, cause pile-up (this appears to be the case for the final large pulse in Fig. 6.5). Regardless of the precise cause of the pulse distribution, the disjointed nature of this trace means that pulse discrimination based on standard techniques is likely to be ineffective for this application.

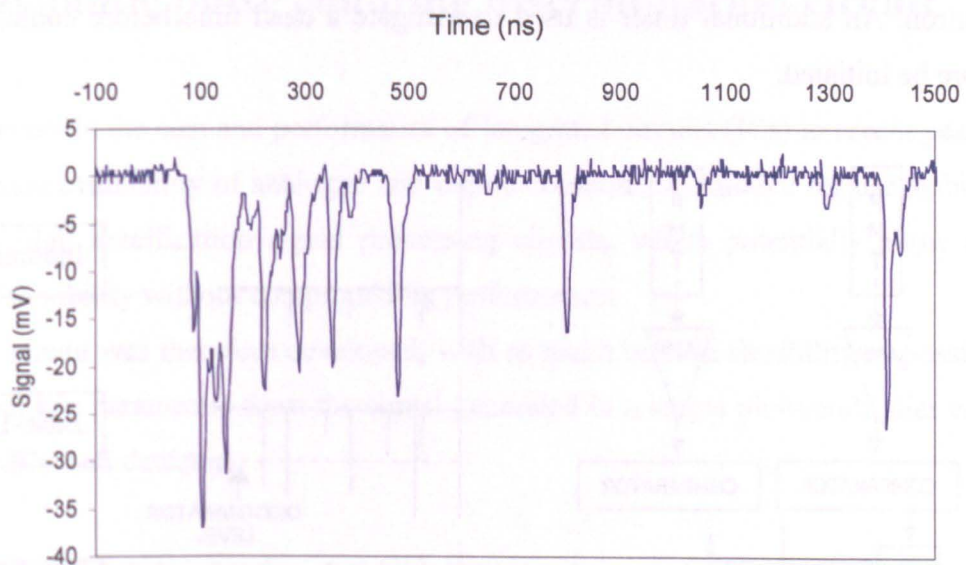


Fig. 6.5: Neutron signal pulse train produced by large BN:ZnS(Ag) detector irradiated by a  $^{252}\text{Cf}$  reference source

## 6.4 Photon counting discrimination

For the LiF:ZnS detector developed by Barton et al a novel approach was selected for neutron discrimination, to overcome the lack of signal strength. Their technique, described in detail by Davidson [47] and McMillan [48], employed two methods to counteract the two main sources of noise in the detector: dual PMT in coincidence to remove random noise from sources such as the PMTs, and a pulse counting method to remove unwanted external gamma interference, Fig. 6.6. Here incoming signals are differentiated to produce a train of pulses, which can be readily counted. The two PMTs in coincidence trigger a timer, and counts are then summed for both PMTs. If a preset level is exceeded, within the a fixed time period, a signal is generated to identify a neutron. An additional timer is used to instigate a dead time before counting can once more be initiated.

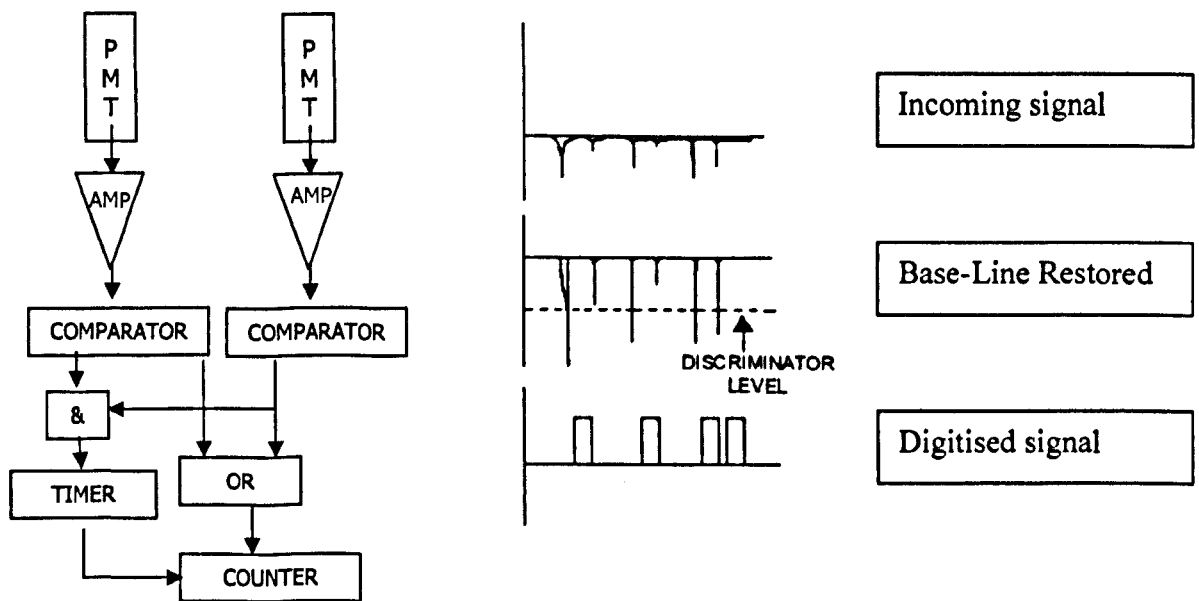


Fig. 6.6: Simplified schematic, and neutron signal pulse train as found in LiF:ZnS detector

Although the above technique has proved to be effective the count threshold required must be set very low (3-4 photons) to achieve adequate sensitivity. Also a certain amount of post processing is required to filter out anomalous signals. Although this is partly due

to the small incoming signal it suggests neutron signatures are being lost, possibly due to processing delays and losses in the analogue front end, which effectively discards some information i.e. the initial large pulse created by the build up of photons in the first 100 ns is currently disregarded. This portion of the signal can represent as much as 50% of the total light collected [123].

Additionally the PNL circuit is implemented in analogue and solid state TTL digital electronics, much of which has been superseded and is now obsolete. Also adjustments to threshold and timing parameters requires disassembly and in some cases component changes. It was therefore decided that a new circuit be developed, to enable streamlined testing and optimization both in the lab and field.

## **6.5 Dynamic pulse counting discrimination circuit**

Improvements in the cost and performance of integrated circuits (ICs) in recent years, has led to a wide availability of analogue and digital components suitable for use as building blocks in high specification signal processing circuits, which potentially allow a high degree of flexibility without compromising performance.

A circuit was therefore developed, with as much built in flexibility as possible, to extract two key parameters from the signal generated in a single photomultiplier coupled to a large BN:ZnS detector:

- Peak signal height for the initial fast pulse, shaped to match initial 10ns exponential decay for ZnS(Ag).
- Pulse count for subsequent small (single photon) pulses, over a selectable time period.

To achieve this the circuit requires the following three discrete stages:

1. Analogue front end: Fast, low noise, surface mount operational amplifiers and comparators with configurable thresholds to provide a robust signal interface.
2. Digital logic: High speed, low power discrete digital logic gates to implement timing and counting of pulse trains.

3. Microcontroller: Programmable embedded processor to control data acquisition and provide interface for remote analysis and storage of data.

### 6.5.1 Analogue front end

This is in many ways the most critical part of the circuit [124]. It is required to capture incoming events with amplitudes varying from a few mV to several Volts, and rise times of several nanoseconds, without losing data or adding noise or interference. It must be inherently robust and reliable across the full range of possible input levels.

The incoming signal, produced by a photomultiplier tube anode, taking dynode biasing from a conventional voltage divider network [126,127,128], is capacitively coupled to the discriminating circuit.

The block diagram in Fig. 6.7 show how the input signal is buffered, amplified, and then split; to provide a low gain trigger level on the initial large pulse, a high gain path, for single photon counting, and a low gain, pulse shaping route, to a peak capture circuit. Two variable discriminator thresholds are implemented, on separate signal paths:

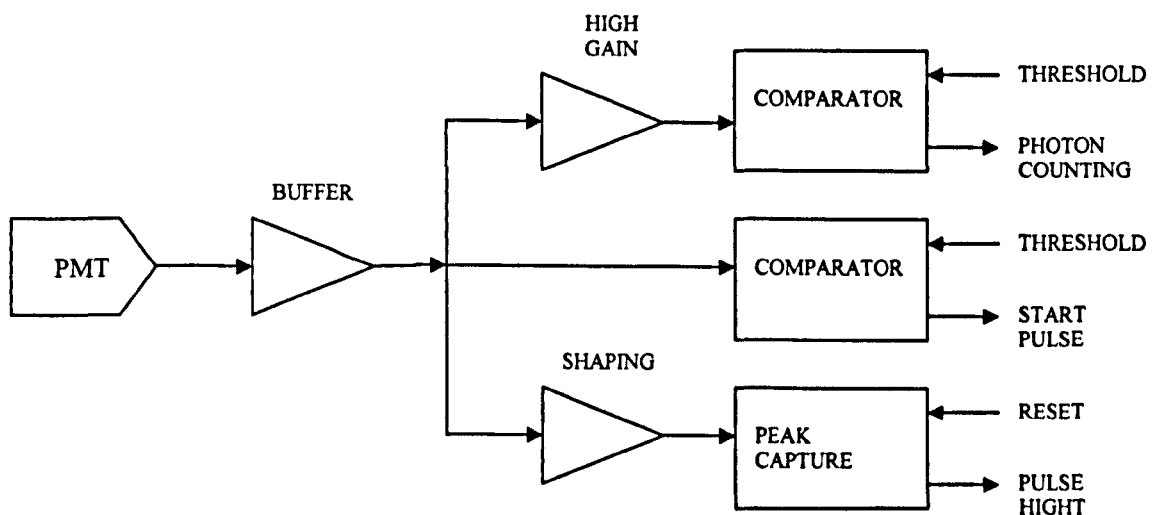


Fig. 6.7: Analogue signal block diagram for the new discriminator circuit

A number of operational amplifiers (op-amps) and comparators were “bread-board” tested, before final selections were made. The components chosen for implementation of the circuit are shown in Table 6.2.

Component	Type	Manufacture	Performance	Comments
LMH6732	Op-amp	National Semiconductor	$<2700\text{V } \mu\text{s}^{-1}$ $2.5 \text{ nV}/\sqrt{\text{Hz}}$ noise	Variable - high gain bandwidth
AD8057 - 58	Op-amp	Analogue Devices	$1000 \text{ V}\mu\text{s}^{-1}$ $7 \text{ nV}/\sqrt{\text{Hz}}$ noise	Fast, low power, low cost
ADCMP601	Comparator	Analogue Devices	3.5 ns rise time	Programmable hysteresis

Table 6.2: Key analogue components of the photon counting discriminator circuit

The final analogue circuit is shown in Fig. 6.8, along with the dual digital potentiometer (AD5252) use to provide selectable threshold levels to the comparators, and digital logic gates required to implement pulse counting.

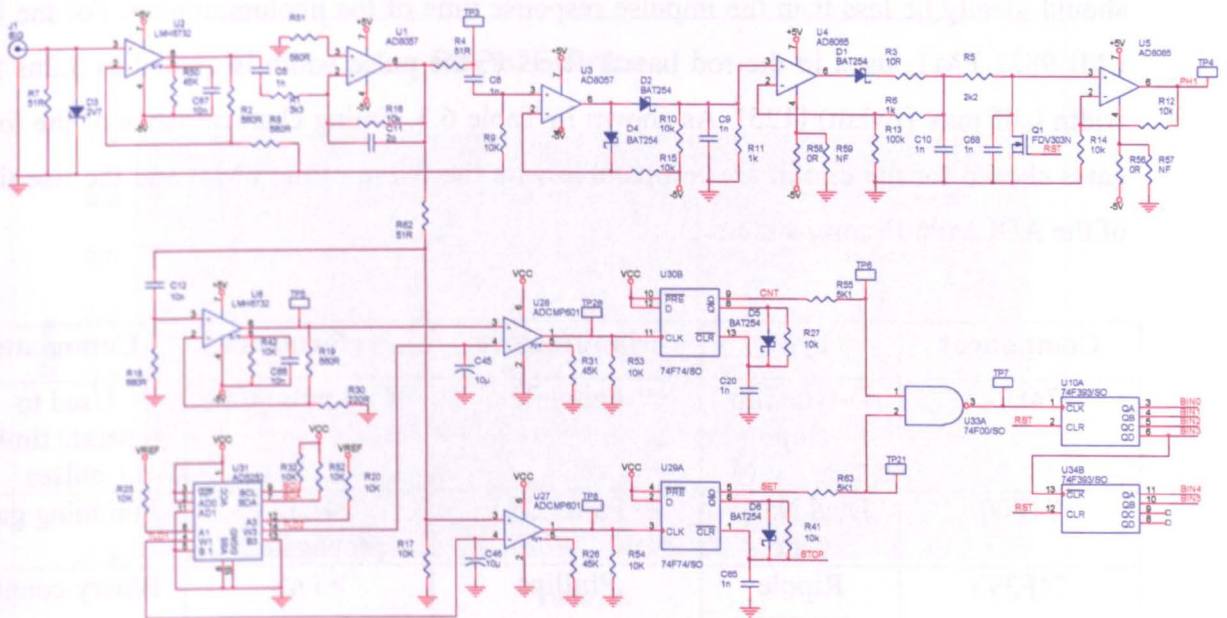


Fig. 6.8: Analogue / digital circuit diagram for discriminator development

### 6.5.2 Discrete logic for fast pulse counting

The purpose of this part of the circuit is to count photons in the incoming pulse train, following on from the large initial event. Start of the counting period is triggered by the initial peak, and ended on a reset signal from the microcontroller. A flow chart is shown in Fig. 6.9.

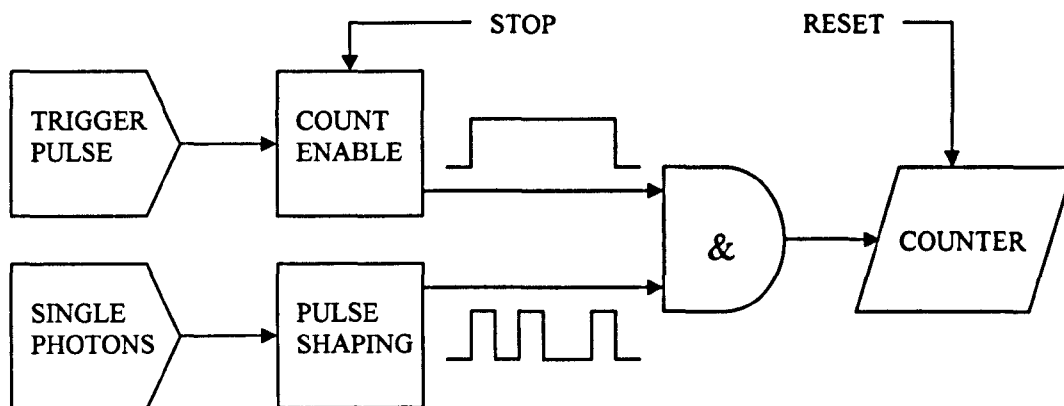


Fig. 6.9: Photon counting logic - flow chart

To ensure as many photons as possible are counted, the inherent delay in the logic ICs should ideally be less than the impulse response time of the photomultiplier. For the fast EMI 9821 PMT, used in the rod based detector, the pulse width is quoted as 3.2ns full width half max (fwhm) [125]. As shown in Table 6.3, timing characteristics of the logic gates chosen for the circuit are comparable with the fwhm of the PMT, and the rise time of the ADCMP601 comparators.

Component	Type	Manufacture	Performance	Comments
74F74	D-type flip flop	Fairchild	>4 nS pulse time	Used to generate timing pulses
74F00	Dual Nand Gate	Fairchild	<4 nS propagation	Summing gate
74F393	Ripple counter	Phillips	>5 nS	Binary counter

Table 6.3: Key logic components to the photon counting discriminator

### 6.5.3 Circuit modelling and prototyping

Pspice is a general purpose, analogue and mixed mode, component level, circuit modeling tool used to verify electronic design and predict behaviour. It is a PC based implementation of SPICE (Simulation Program for Integrated Circuit Emphasis), written at the University of California, Berkley in 1975 [129], and is supported within the Orcad printed circuit board (PCB) development suit supplied by Cadence [130]. It is highly

suites to the simulation of analogue events providing both time domain and frequency analysis.

To assess the predicted performance of the critical analogue and digital front end circuits, a Pspice model was constructed using integrated circuit (IC) models supplied by the component manufacturers (Table 6.2 and 6.3). Figure 6.10 shows waveforms produced by the model. In this figure a small photomultiplier input signal (pink) can be seen amplified (light blue) and filtered to generate a pulse train (dark blue), this triggers a monostable (maroon) which enables integration of the pulse count (yellow). The modelling allowed verification of the analogue design, and help in the selection of passive components (resistors and capacitors) to provide appropriate filtering and gain for stable operation.

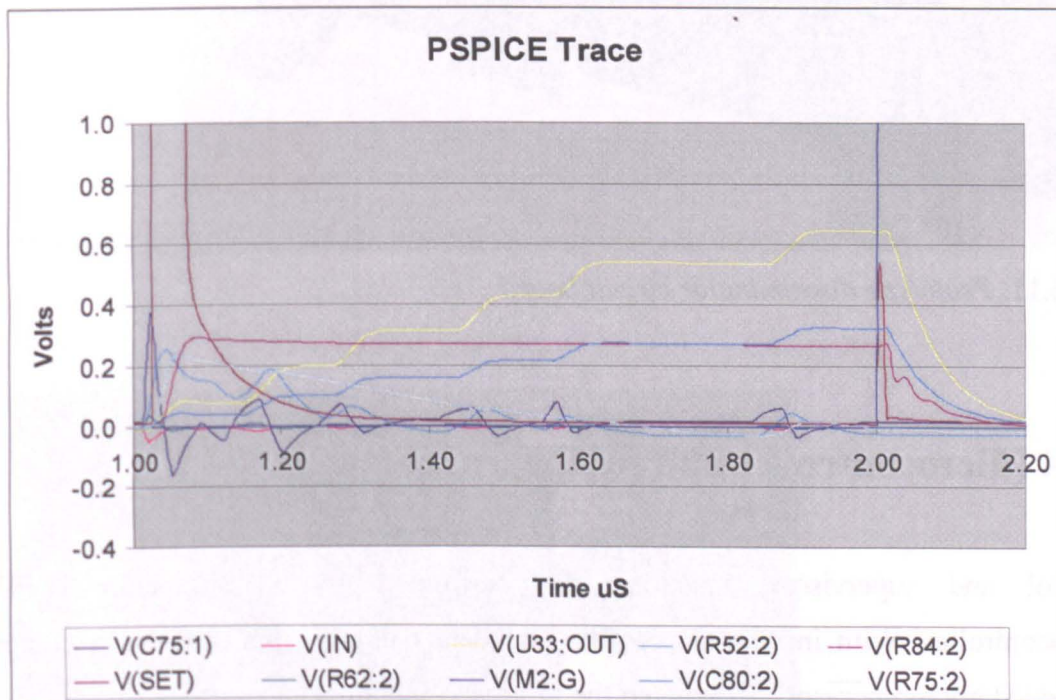


Fig. 6.10: PSPICE output trace for typical neutron signal; input signal (pink), amplified (light blue), filtered (black), integrated pulse count (yellow)

Once a robust working model was established, a prototype unit was manufactured on a dual sided printed circuit board (PCB) to implement the analogue, digital logic and control electronics, see Fig. 6.11. The circuit was tested with a simulated input signal generated by a Philips PM5786B waveform generator. It was found that, while at lower frequencies the circuit behaved as intended, at high frequencies (<100ns pulses) ringing occurred. By disconnecting the digital signal path the source of the interference was

identified as feedback, probably through supply lines, although air coupling could not be discounted. A second circuit was designed with the utmost attention to providing a robust earth plane, and thorough supply decoupling to ensure a minimum of ringing and cross talk. All the analogue components were located on an area of the PCB remote from digital electronics, and within a copper screening can to prevent interference commonly caused by the sharp edges of the logic pulses, see Fig. 6.13.

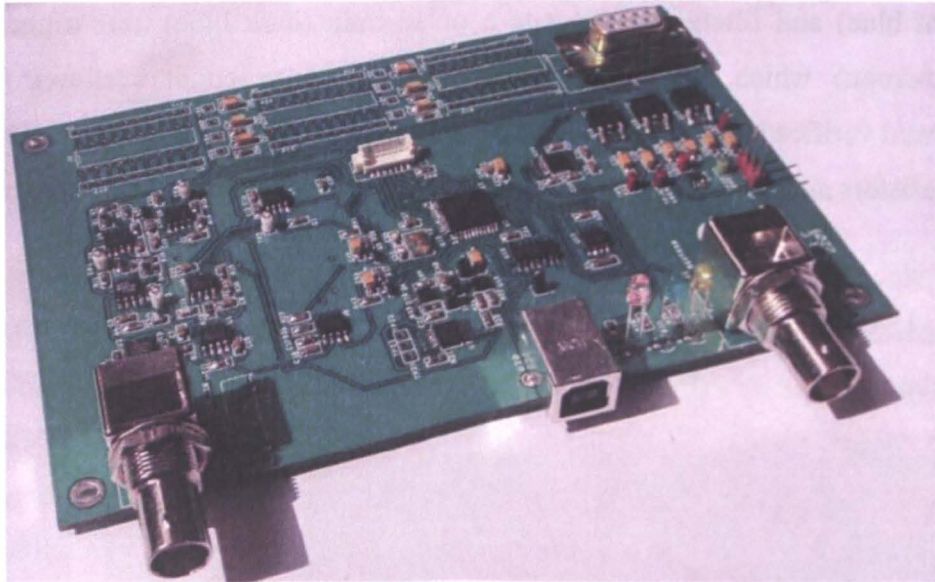


Fig. 6.11: *Prototype discriminator circuit board*

### 6.5.4 Microcontroller and peripheral components

Control and supervisory functions are performed by a Microchip 18F4550 microcontroller. With integrated program and data memory, this provides a complete embedded microprocessor, to carry out the following functions:

1. Timing of pulse acquisition and photon counting
2. Data collection and storage
3. Setup and monitoring of thresholds and PMT bias voltage and other levels through on board analogue to digital converters
4. USB serial interface
5. Drive indicators and output signals

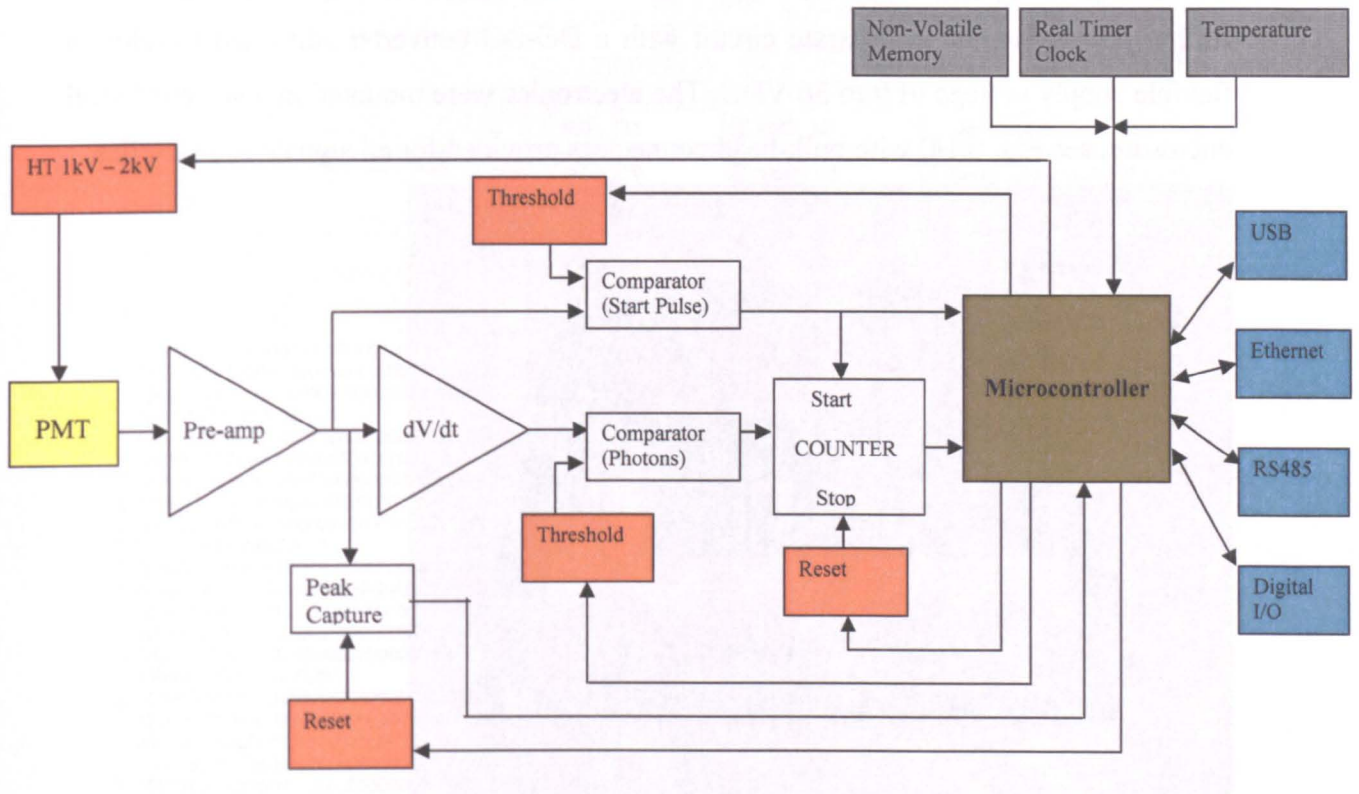


Fig. 6.12: Discriminator circuit; Microcontroller functions and interfaces

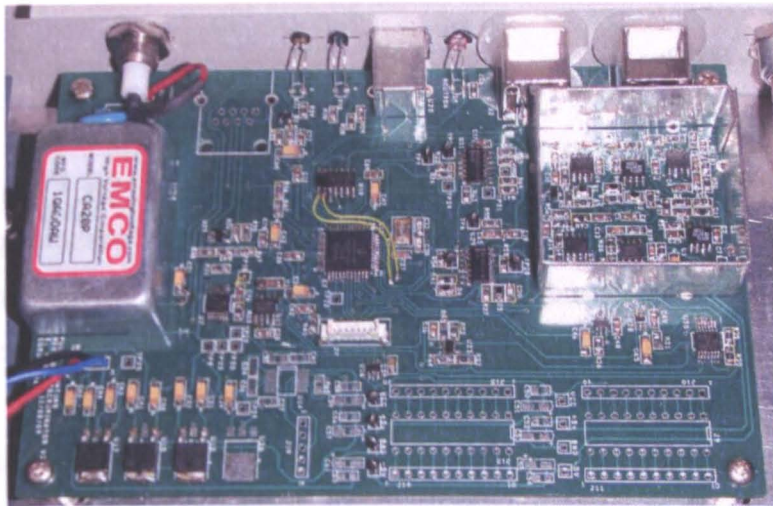


Fig. 6.13: Main discriminator PCB; analogue circuit inside screening can on right (lid removed), microcontroller and digital circuitry centre, power supplies left, prototyping area bottom right

A real time clock, ambient temperature monitor, Ethernet interface and modular high voltage PMT supply were also provided on the PCB, along with a prototyping area for further developments. A separate circuit with a DC-DC converter was used to allow a flexible supply voltage of 9 to 36 VDC. The electronics were mounted in a screened steel enclosure, see Fig. 6.14, with bulk-head connectors provided for all signals and supplies.

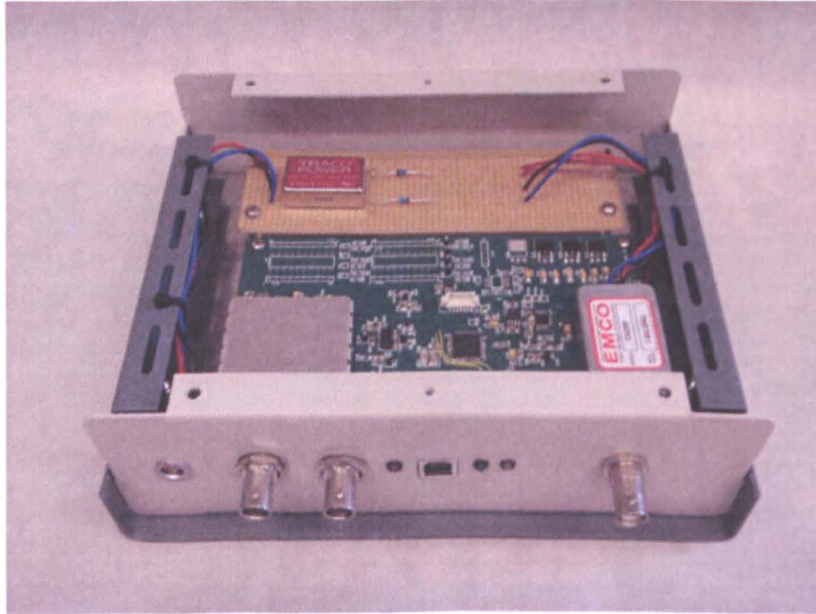


Fig. 6.14: *Discriminator electronic assembly*

## 6.6 Analysis software

Software was written in C++ to drive the discriminator circuit from a remote PC over either a USB or Ethernet link. This includes: set-up of all timing variables, thresholds etc; data acquisition; data storage; analysis and display. Figure 6.15 shows a screen dump during data acquisition. Incoming data is displayed on the left of the screen, data collected over a period of time is on the bottom right, set-up parameters are on the top right

For each pulse large enough to trigger the circuit, the key parameters of pulse height and after pulse count are captured by the microcontroller. These values are collated and transmitted to a remote PC on request, e.g. once per second.

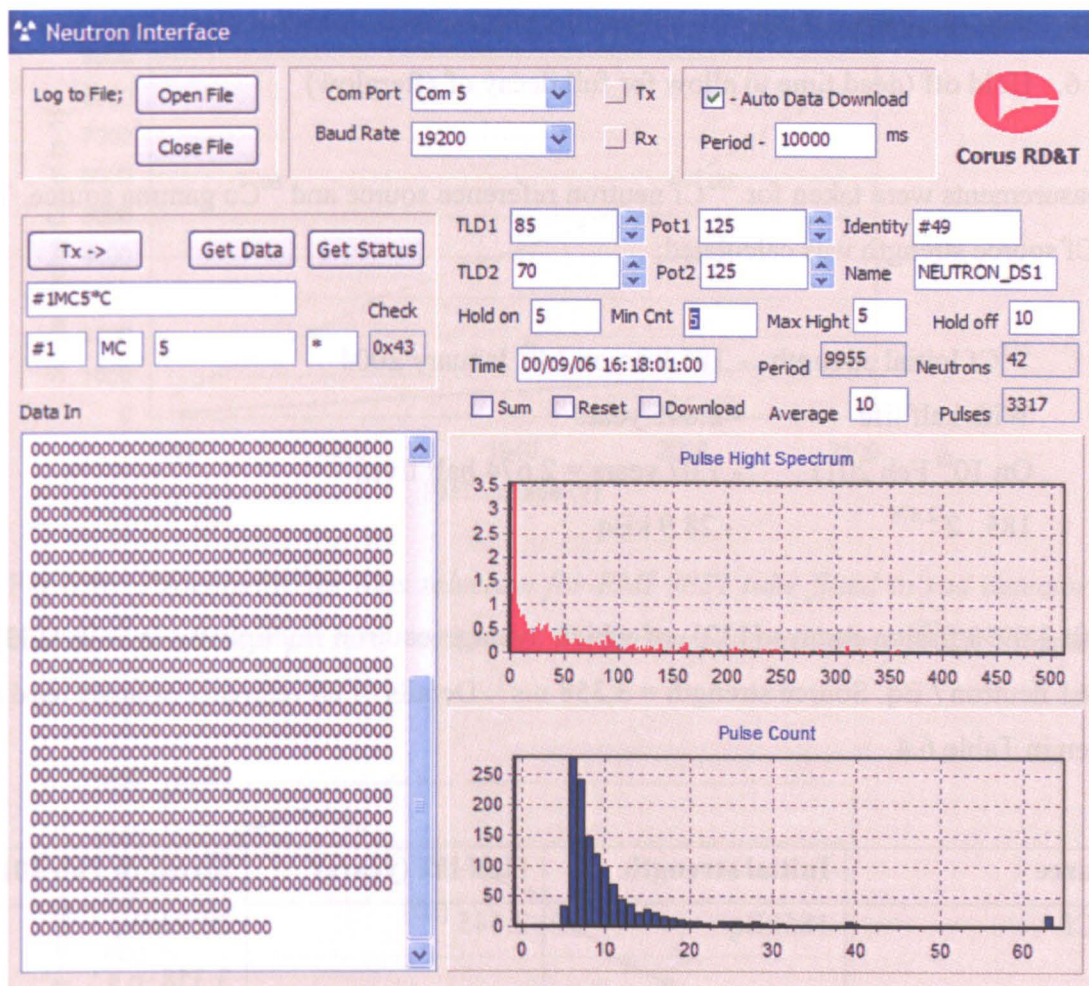


Fig. 6.15: Neutron detector interface software – live screen dump.

## 6.7 Setup and optimization of photon counting discriminator

The process of testing and evaluation of the discriminator circuit was problematic due to the complexity of the pulse discrimination technique, and the number of parameters involved. During initial testing the following variables were systematically adjusted to optimize performance;

1. PMT high voltage
2. Discriminator threshold for the start pulse.
3. Discriminator threshold for after pulses (single photons).
4. Pulse counting period.

5. Pulse count threshold.
6. Hold off (dead time to allow for full decay of afterglow)

Measurements were taken for  $^{252}\text{Cf}$  neutron reference source and  $^{60}\text{Co}$  gamma source. The  $^{252}\text{Cf}$  source strength was calculated:

$^{252}\text{Cf}$  Initial strength - 185 kBq on 14<sup>th</sup> January 2004  
 With half life - 2.645 years  
 On 10<sup>th</sup> Feb 2011 - 7.07 years = 2.674 half lives  
 $185 \cdot 2^{-2.674}$  - 28.9 kBq

With 3.09% fission decays [132], of which average neutron multiplicity is 3.76 [133] = 11.61 neutron / Bq. Source strength = 3,358 n.s<sup>-1</sup>. Details of all reference sources used are given in Table 6.4.

Source	Initial strength	Half life (years)	Strength Feb 2011
$^{252}\text{Cf}$	185kBq	2.645 [132]	28.9 kBq 3,358 n.s <sup>-1</sup>
$^{60}\text{Co}$	48MBq	5.27 [134]	119 kBq
$^{137}\text{Cs}$	370kBq	30.2 [134]	147 kBq

Table 6.4: Reference sources used for setup and evaluation

Selecting an appropriate high voltage supply level of the photomultiplier is normally achieved by plotting count against voltage, and selecting a value just above the start of the plateau region. However, for the tube used here (EMI 9821) no clear plateaux can be observed, see Fig. 6.16. Ideally this tube would have been replaced, however the long lead time for procurement of a replacement tube, made this impossible. Therefore a compromise mid-voltage of 1950 V was selected.

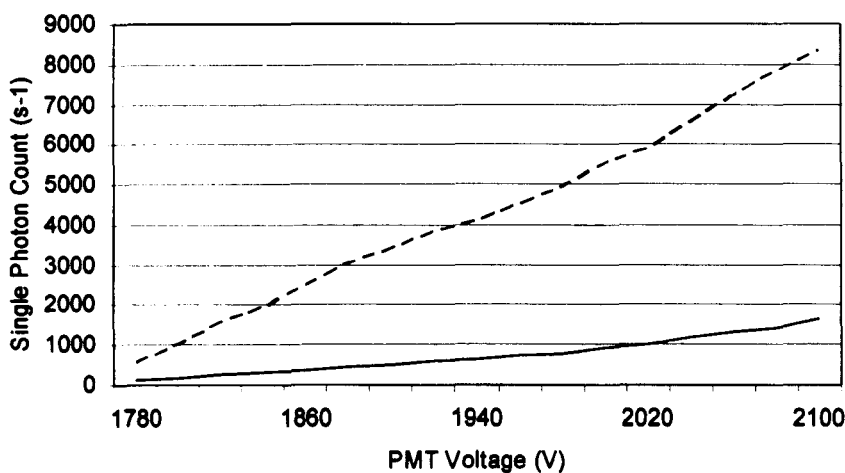


Fig 6.16: *Photomultiplier bias selection for EMI 9821 tube fitted to rod detector; Dark count (no scintillator present)– solid line, Foreground (scintillator +  $^{252}\text{Cf}$ ) – dashed line*

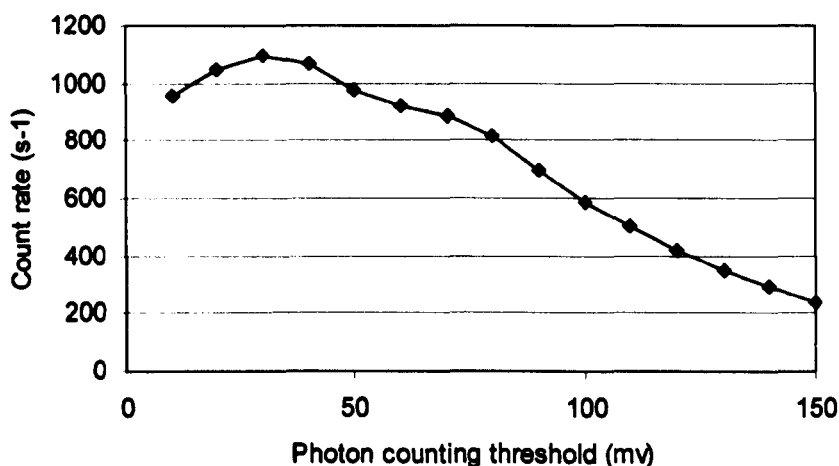


Fig. 6.17: *Rod based detector photon counting threshold optimisation;  $^{252}\text{Cf}$  source*

Figure 6.17 shows total pulses counted plotted against threshold level, for the reference neutron sources. The peak count rate starts to fall off above 40mV suggesting this is a suitable photon counting level. Figures 6.18 and 6.19 show the effect of changing the minimum number of photons required to trigger a neutron event; for a start pulse threshold above 60mV a minimum photon count level of 14 reduces the gamma induced measurement to a minimum level less than  $0.5 \text{ n.s}^{-1}$ , which is undoubtedly caused by neutron background.

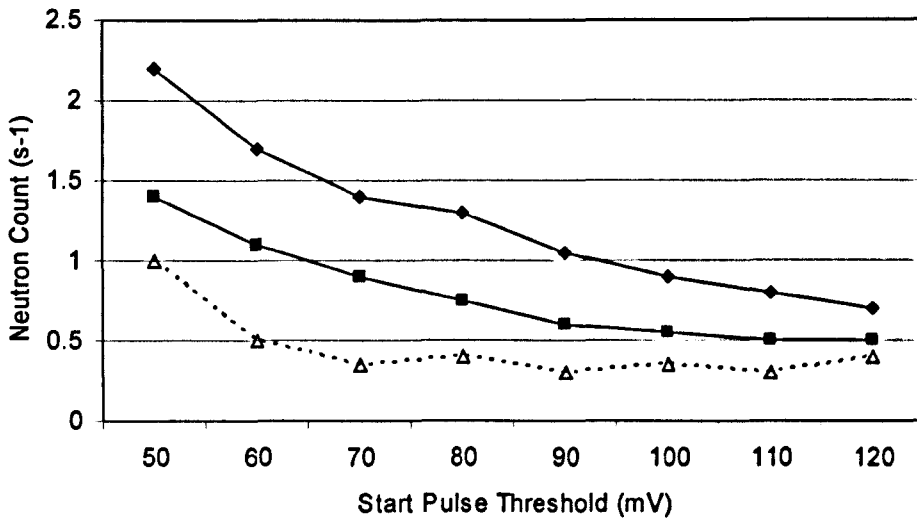


Fig. 6.18: Rod based detector, photon counting optimisation  $^{60}\text{Co}$  source; 10 count threshold – diamonds, 12 count threshold – squares, 14 count threshold – triangles

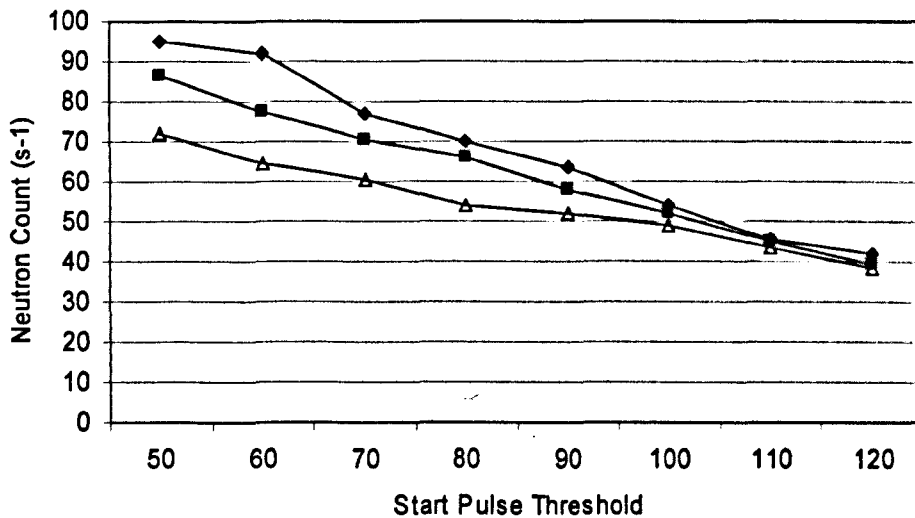


Fig. 6.19: Rod based detector, photon counting optimisation  $^{252}\text{Cf}$  source; 10 count threshold – diamonds, 12 count threshold – squares, 14 count threshold – triangles

Realistic setup parameters for the rod detector, optimizing neutron sensitivity and gamma immunity, are given in Table 6.5. The count period was based on the typical decay characteristics of ZnS(Ag) (see Chapter 4). The hold off period (dead time) was

determined experimentally using the  $^{252}\text{Cf}$  source. The count rate, plotted against hold-off time, is shown in Fig. 6.20.

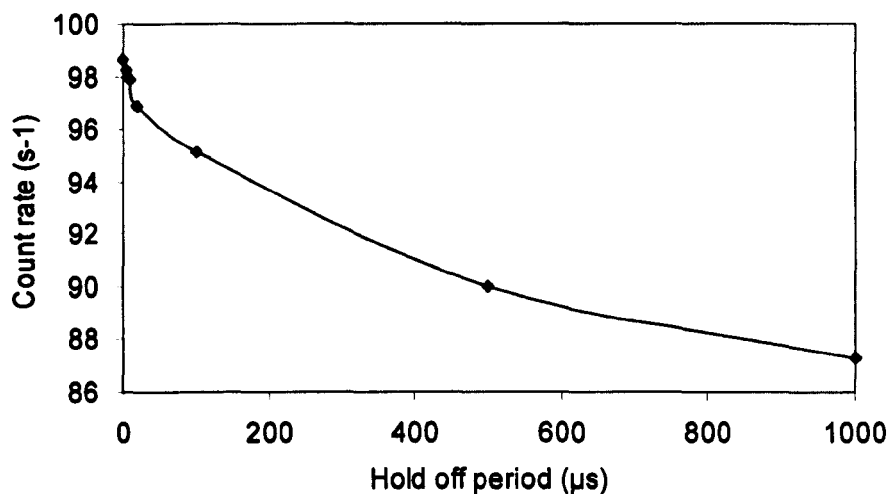


Fig. 6.20: Rod based detector, dead time optimisation  $^{252}\text{Cf}$  source at 100mm

PMT Supply (V)	Start Threshold (mV)	Single photon Threshold (mV)	Min. photon count	Count Period ( $\mu\text{s}$ )	Hold off Period ( $\mu\text{s}$ )
1950	60	100	14	10	50

Table 6.5: Optimum setup parameters for rod based BN:ZnS detector

## 6.8 Dynamic photon counting algorithms

The newly developed electronics and software platform permitted extensive experimentation to be carried out, with techniques for improved discrimination. It is believed that this is particularly important for the successful implementation of a detector with only one photomultiplier (by comparison to the PNL detector, where two photomultipliers were used in coincidence to reduce background rate).

In particular various methods were investigated to use the size of the initial pulse to modify the photon counting technique (previously described in section 6.4). The most straightforward technique involved the use of dual discriminator levels; one for initial event triggering, and another for subsequent photon counting. The counting period is

triggered when a pulse exceeds a high threshold, representing several simultaneous photons. A more sophisticated method uses fast peak capture, whereby the start pulse is shaped (with a 100 ns time constant) and its peak value is captured and measured. The size of this start peak, which represents at least 30% of the light captured in the PMT [97] during the scintillation event, can be used to control the subsequent photon counting, as follows:

1. Application of a flexible period for photon counting, determined by the size of the initial pulse (i.e. larger start events are followed by longer pulse trains).
2. Dynamic count threshold (i.e. higher number of photons following large start pulse).
3. Variable hold off; to minimize dead time and reduce double counting.

As the rising edge of the start pulse is used to enable photon counting, this occurs while the start pulse is being captured and analysed.. Here pulses only have to exceed a lower threshold, representative of single photon events [131]. Termination of the count period and assessment of count threshold are then dynamically applied as discussed above.

The two forms of background noise are rejected in the following way;

1. Gamma rejection: Due to the scintillating thin layers, only a small amount of gamma radiation will be absorbed by the ZnS. This results in fast decaying weak signals. A relatively small start pulse triggers a short counting period. The random nature of the gamma signals means that insufficient pulses will normally be observed in this period.
2. Photomultiplier noise: This can be in several forms, either small random signals, as above, or large discharge type events. The former are rejected in the same way as gamma. Large events trigger a longer counting period, with an associated high count threshold with should not be reached by the relatively short after glow from these one-off events.

Results from the assessment of these discrimination techniques are detailed in Chapter 7, alongside comparisons of performance against bench mark detectors.

## 6.9 Conclusions

Techniques have been investigated for neutron discrimination, using the slow fluorescent decay characteristic of ZnS(Ag) following an alpha absorption. A custom made circuit has been developed to collect data from a single photomultiplier coupled to a large laminar neutron scintillation detector. The circuit has been optimized for use with heavily attenuated signals from BN:ZnS and large lossy light guides. As a test bed for new discrimination techniques, a high degree of flexibility has been incorporated into its design; such as adjustable set-points, thresholds and other control parameters. The circuit had been assembled into a robust, stand-alone module suitable for extended testing in various locations. Further details of testing and analysis of detector performance, employing the new discriminator circuit, are given in Chapter 7.

An additional piece of work has been initiated, to miniaturise the discrimination circuitry, enabling it to occupy a purpose made module mounted directly on the base of the photomultiplier. A prototype of this assembly is shown in Fig. 6.21. Although yet to be completed, this unit will offer the robustness, compactness and low installation cost required for installation of multiple detectors on large scale installations.

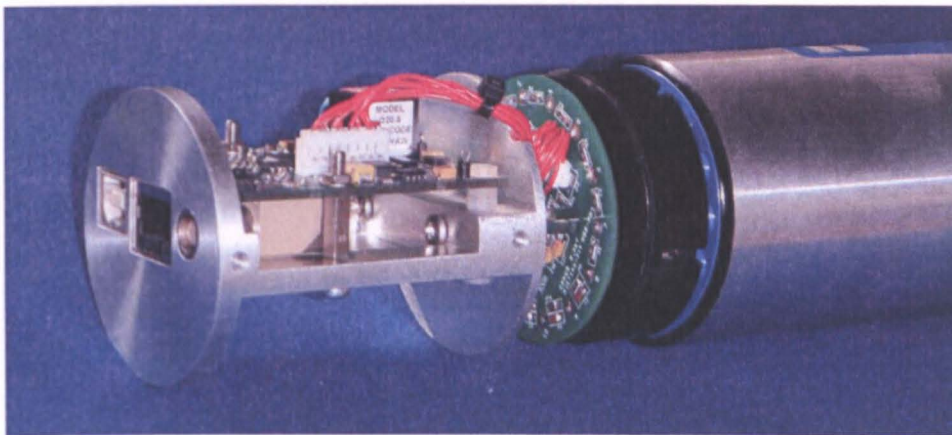


Fig 6.21: *Photomultiplier mounted discriminator module*

# Chapter 7

## Testing and evaluation of BN based detectors

### 7.1 Introduction

This chapter details the setup, testing and evaluation of the two boron nitride thermal neutron detectors described in Chapter 5, alongside the  ${}^6\text{LiF:ZnS}$  and  ${}^3\text{He}$  detectors described in Chapter 2. Testing primarily employed a small  ${}^{252}\text{Cf}$  reference source, but also involved the use of larger gamma sources to establish figures for gamma immunity. While the size of the detectors precluded thorough environmental testing, due to limitations of available facilities, a limited study of likely environmental performance has also been made.

As the two BN:ZnS neutron detectors utilised different photomultiplier arrangements, two PMTs on the laminar detector and one on the rod based design, it was necessary to evaluate them using dedicated electronics modules: the laminar detector employing a circuit based on the pulse counting discriminator developed for the PNL detector (described in Chapter 2), the rod based detector having a circuit which measured pulse height along side photon counting (detailed in Chapter 6). When comparing the two detectors it is therefore impossible to attribute performance differences to limited aspects of the detector design, such as light guide geometry; conclusions can only be drawn about the detector as a whole, including signal processing electronics.

## 7.2 BN detector optimization

As the pulse discrimination technique is essential to the reliable and robust operation of the composite scintillation detectors, further laboratory testing was undertaken on the rod based boron nitride unit, to evaluate alternative algorithms. The basic detector settings were made as listed in Table 6.5. The following three discrimination techniques were then tested;

1. Basic photon counting discrimination as described in section 6.4 (see Fig. 7.1)
2. Basic photon counting discrimination with the addition of a peak height threshold (see Fig. 7.2)
3. Dynamic photon counting discrimination (see Fig. 7.3)

Test were carried out using the sources described in Table 6.4; initial with no source present (i.e. background), with the  $^{137}\text{Cs}$  on the face of the detector, and with  $^{252}\text{Cf}$  at 2 m. In each scenario data was collected over 500 s to reduce statistical variability to an acceptable level. Where count rate is the measured parameter, the main contribution to error is from statistical variation. As these are discrete events, occurring in a fixed time period, their distribution will follow a Poisson law, the standard deviation of which is equal to the square root of the count rate over the whole period. A typical count rate of 2 per second (or 1000 over the count period) will have a variance of 3%. For clarity this error has not been shown on most graphs. Other sources of error, primarily from environmental factors such as laboratory furniture and fluctuations in background radiation levels, were minimized where possible by carrying out measurements sequentially on a single day.

The results shown in Figures 7.1 to 7.3 illustrate the effect of photon counting threshold on the neutron count rate (for  $^{252}\text{Cf}$ ), and background noise (specifically gamma interference); by comparing the separation between background and foreground traces it can be seen that, for the rod based detector (with a single photomultiplier tube), photon counting alone is less satisfactory for rejecting gamma noise than techniques which also employ pulse height.

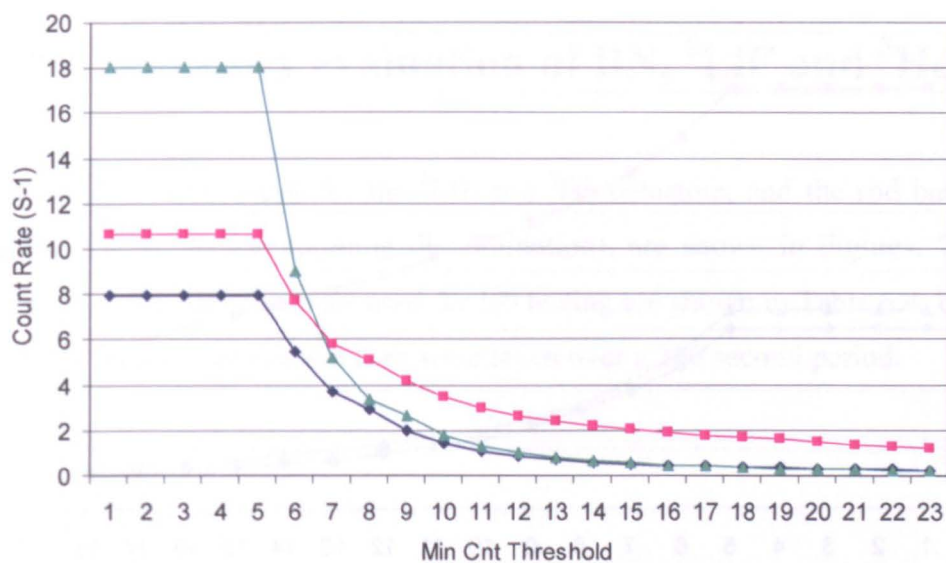


Fig. 7.1: BN Rod detector with simple photon counting discrimination;  $^{252}\text{Cf}$  source - squares,  $^{137}\text{Cs}$  - triangles, Background - diamonds

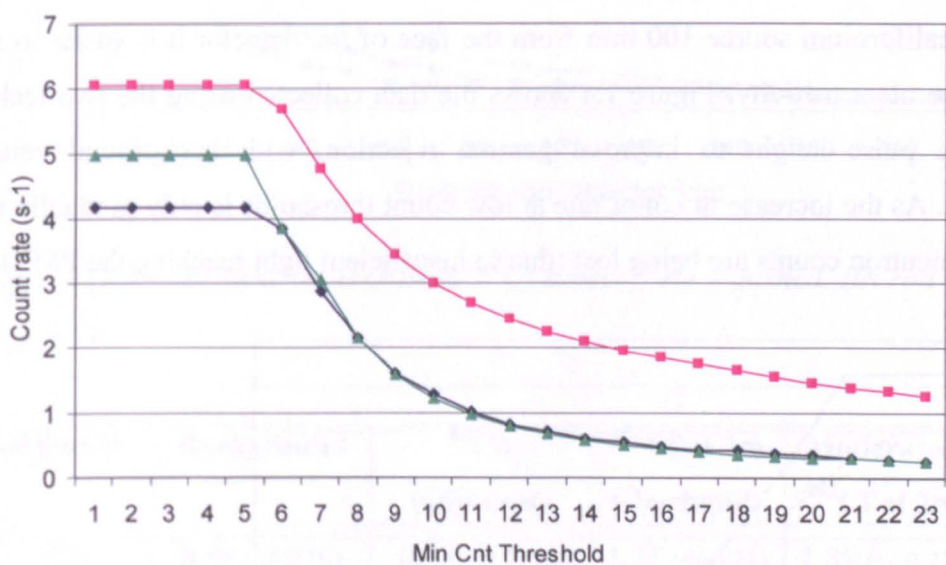


Fig. 7.2: BN Rod detector with photon counting discrimination + pulse height threshold;  $^{252}\text{Cf}$  source - squares,  $^{137}\text{Cs}$  - triangles, Background - diamonds

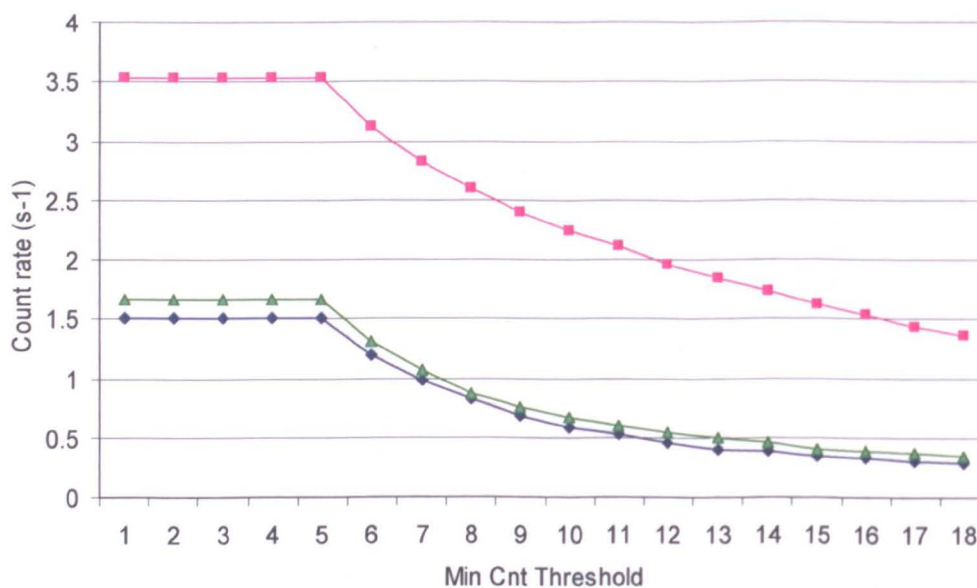


Fig. 7.3: BN Rod detector with combined dynamic photon counting discrimination;  $^{252}\text{Cf}$  source - squares,  $^{137}\text{Cs}$  - triangles, Background - diamonds

With the californium source 100 mm from the face of the detector it is easier to make a comparison of sensitivity. Figure 7.4 shows the data collected using the two techniques which use pulse height to improve gamma rejection, with background count rate subtracted. As the increase in count rate at low count thresholds is only gradually rolling-off, some neutron counts are being lost (due to insufficient light reaching the PMT).

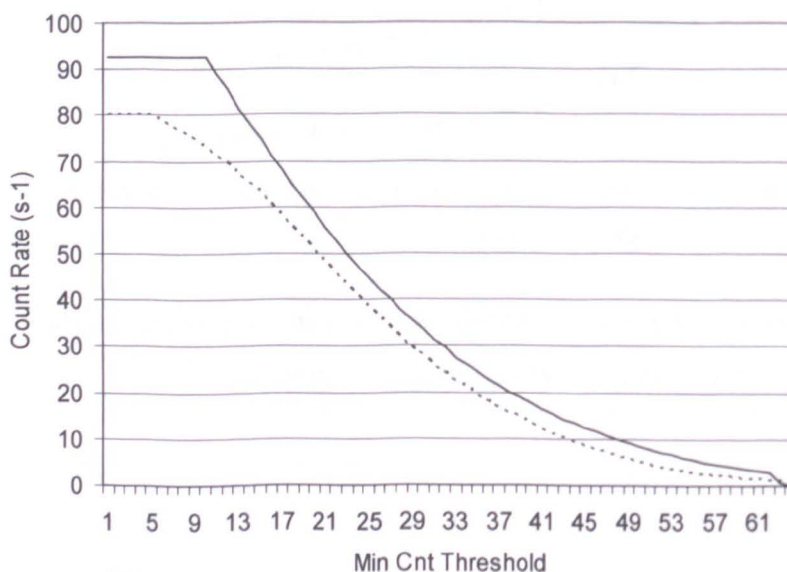


Fig. 7.4: BN Rod detector with dynamic photon counting discrimination (solid) and pulse height threshold (dashed), for  $^{252}\text{Cf}$  source at 100 mm (background subtracted)

### 7.3 Laboratory evaluation of BN, ${}^6\text{LiF}$ and ${}^3\text{He}$ detectors

Comparative test results for the  ${}^6\text{LiF}$  and  ${}^3\text{He}$  detectors, and the rod based BN detector (using simple photon counting discrimination), are shown in Figures. 7.5 and 7.7, and Table 7.1. Details of sources used for lab testing are shown in Table 6.4. Unless otherwise stated measurements shown here were taken over a 300 second period.

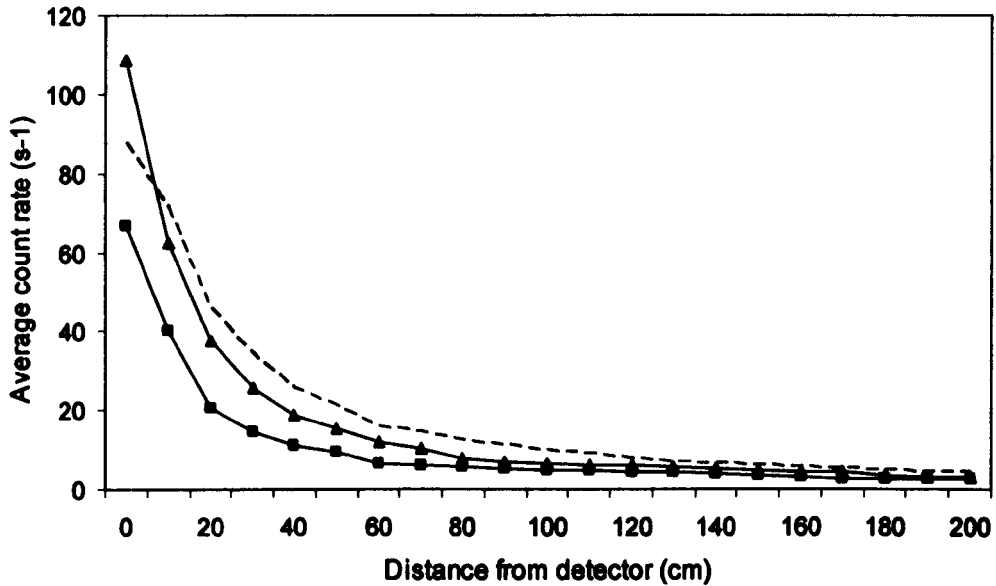


Fig. 7.5: Detector neutron sensitivity  ${}^{252}\text{Cf}$  source;  ${}^3\text{He}$  – dashed, BN rod – triangles,  ${}^6\text{LiF}$  – squares

Detector	Background	${}^{60}\text{Co}$ (adjacent)	${}^{252}\text{Cf}$ at 2m (-backgnd)	Moderated ${}^{252}\text{Cf}$ at 2m	MCNP model
${}^3\text{He}$	0.44 (+/-0.10)	0.48 (+/-0.10)	1.75 (+/-0.21)	1.89 (+/-0.21)	2.51 (+/-0.06)
BN Laminar	0.05 (+/-0.03)	0.08 (+/-0.03)	0.24 (+/-0.09)	0.20 (+/-0.09)	-
BN Rod 100 $\mu\text{m}$	0.57(+/-0.13)	0.65 (+/-0.13)	1.80 (+/-0.21)	1.81 (+/-0.21)	3.49 (+/-0.07)
BN Rod 200 $\mu\text{m}$	0.62 (+/-0.13)	0.62 (+/-0.13)	1.92 (+/-0.22)	1.75 (+/-0.21)	-

Table 7.1; Count rates ( $\text{s}^{-1}$ ) for laboratory background, an adjacent 119 kBq  ${}^{60}\text{Co}$  source and a 30 kBq  ${}^{252}\text{Cf}$  source at 2 m, with the source naked and moderated by 44 mm polypropylene

Direct comparison between the BN and  $^3\text{He}$  based detector (described in Chapter 2) show a comparable level of sensitivity has been achieved. Discrepancy between the MCNP data and experimental results shown in Table 7.1 are believed to be due to a combination of less than optimum efficiency within the detectors (as discussed in Chapter 3), and inaccuracies in the model due to unknowns regarding composition of building materials etc.

The problems associated with laboratory testing can clearly be seen from Fig. 7.6; where a number of neutron tracks are plotted, from an MCNP model of the laboratory environment in which the above testing was carried out. The model clearly shows the moderating influence of material in the immediate surrounding environment. Although this potential source of error is mitigated, for comparative measurements, by placing source and detectors in the same location; for each set of measurement it cannot be completely removed. Furthermore, this extensive source scattering limits useful comparison of results with third party reports and standards. For consistent measurements, open field testing is therefore preferred.

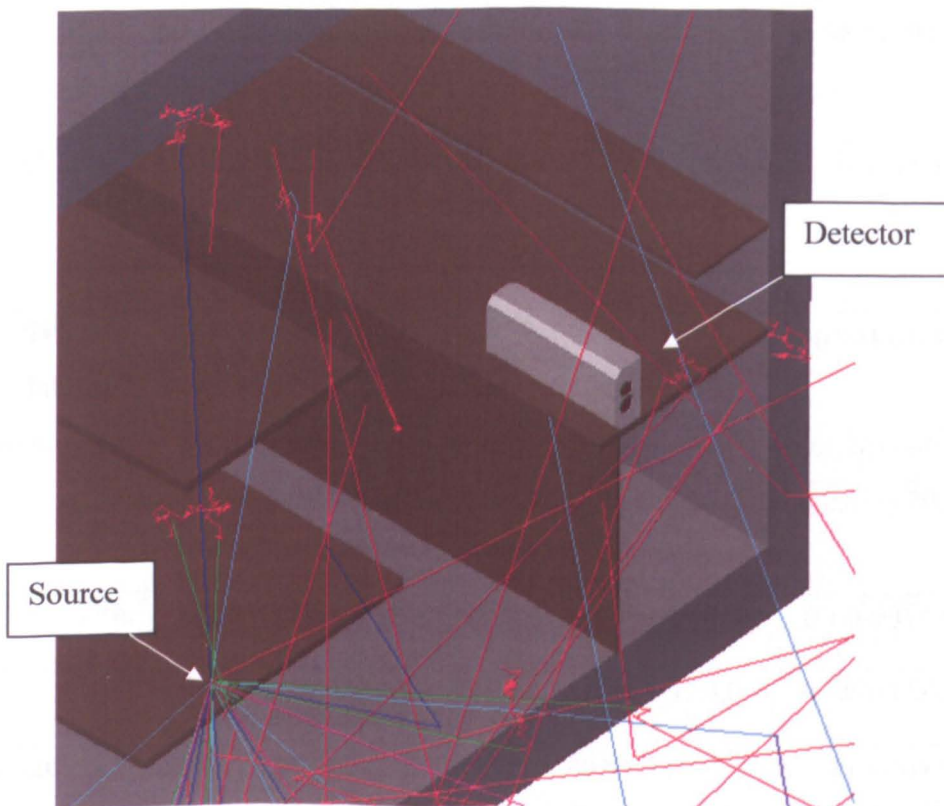


Fig. 7.6: MCNP model of  $^3\text{He}$  detector /  $^{252}\text{Cf}$  source in laboratory environment, showing heavy scattering of neutrons in the floor walls and benches (thermalized neutrons – red)

Uniformity of response, down the length of the BN – rod based detector and bench mark detectors, was tested using the  $^{252}\text{Cf}$  reference source at a distance of 100 mm from the centre line of the detectors front face. Results from these tests are shown in Fig. 7.7 show that while the  $^3\text{He}$  based detectors has the most even response, the BN detector remains within approximately 25% of peak sensitivity along its sensitive area.

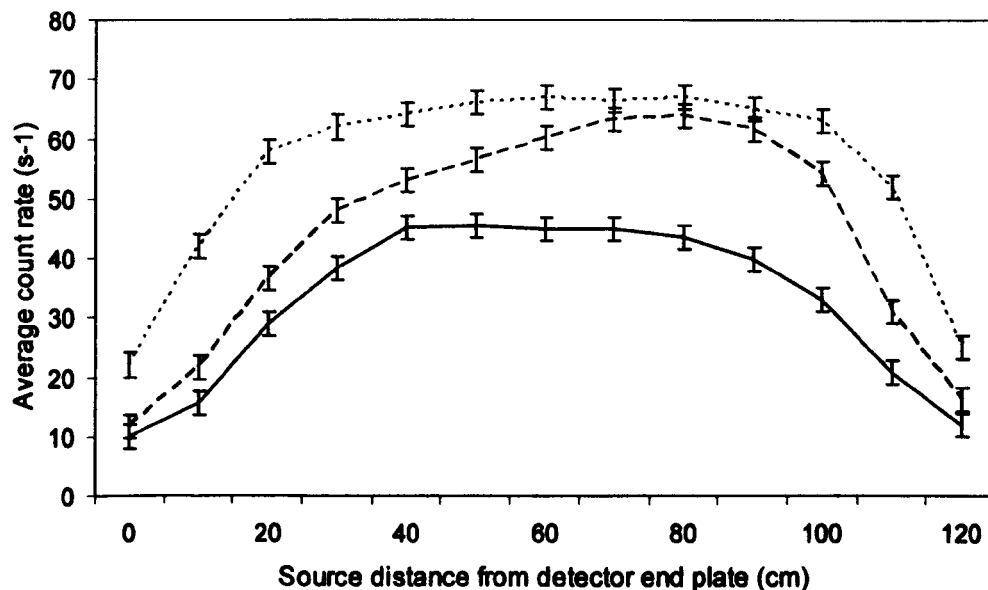


Fig. 7.7: Detector positional sensitivity  $^{252}\text{Cf}$  source at 100 mm;  $^3\text{He}$  – fine dashed, BN rod – dashed,  $^6\text{LiF}$  – solid

## 7.4 Field testing

While it was intended to carry out more extensive field testing on the boron based detectors developed here, this has not so far been possible. Due to involvement in external testing programmes, for the laminar detector at Home Office Scientific Development Branch, and the rod based detector, by the United States Department for Homeland Security, Domestic Nuclear Detection Office (DNDO), access to the detectors for further in house testing has not been possible. The opportunity to take part in third party testing is however most welcome, and will play a significant role in establishing this technology as a realistic alternative to existing products.

Prior to transport of the detector to the DNDO Nevada test site, the equipment was thoroughly tested and re-evaluated. As a result of this the discrimination parameters were further optimised for sensitivity and gamma rejection, as follows;

Threshold1 – 75 mV, Threshold2 - 55 mV, HT – 1950 V, Hold on – 1  $\mu$ s,  
 Hold off – 5  $\mu$ s, Min. Count – 10, Min. height – 5.

Initial test results from the Nevada trials, produced on delivery of the detector (and required to gain acceptance into the trials), are shown in Table 7.2.

Source	Total Count in 300s	Average count rate ( $s^{-1}$ )	Average count rate with background subtracted ( $s^{-1}$ )
Background	2774	9.2	-
$^{252}\text{Cf}$	8766	29.2	20.0 (+/-0.6)
$^{137}\text{Cs}$	2791	9.3	0.1 (+/-0.3)
$^{252}\text{Cf} + ^{137}\text{Cs}$	8744	29.1	19.9 (+/-0.6)
Detector left running for 2hr before measurements were repeated			
Background	2775	9.3	-
$^{252}\text{Cf}$	8468	28.2	18.9 (+/-0.6)
$^{137}\text{Cs}$	2737	9.1	-0.2 (+/-0.3)

Table 7.2; Initial test results from Nevada DNDO testing using 333kBq  $^{137}\text{Cs}$  source and a 65,000  $ns^{-1}$   $^{252}\text{Cf}$  source at 4m distance, with sources and detector 1.5m from the ground

Without taking into account neutrons scattered by the ground or the air, the neutron flux at the detector can be calculated using (7.1)

$$\begin{aligned}
 \text{Neutron flux} &= \frac{\text{Isotopic emission}}{4 \pi \cdot \text{distance}^2} && (7.1) \\
 &= \frac{65,000}{4 \times 3.14 \times 400^2} \\
 &= 0.032 \text{ cm}^{-2}\text{s}^{-1}
 \end{aligned}$$

With an active surface area of approximately 2,000 cm<sup>2</sup>, the intrinsic efficiency of the detector can be calculated using (7.2)

$$\begin{aligned}\text{Intrinsic efficiency \%} &= \frac{\text{Net count rate} \times 100}{\text{Surface area} \times \text{neutron flux}} && (7.2) \\ &= \frac{19.4 \times 100}{2,000 \times 0.032} \\ &= 30.31 \%\end{aligned}$$

While this efficiency figure is high compared to the typical 10 – 15% intrinsic efficiency for a moderated <sup>3</sup>He detector, and at the top end of performance predicted for the laminar BN detectors (Chapter 3), it can be assumed that a significant proportion of the neutrons detected here are partially moderated neutrons, having been scattered largely from the ground, thus significantly raising the apparent efficiency. A comparison with MCNP data, generated using a simplified model of the test site, predicts an efficiency of 34.5% (which is in line with the discrepancy seen on other MCNP models). As an indication of the proportion of neutrons that will have been detected directly from the source, the same model was run with the ground removed; in this case 25.2% of neutrons are captured. This suggests approximately 27% neutrons are detected as a result of scattering en route to the detector, and 63% are directly detected. Applying this factor to the measured efficiency leaves an intrinsic efficiency of 19.1%. This seems to be a realistic figure, well in line with expectations and significantly better than other comparable technology (i.e. <sup>3</sup>He based detectors).

## **7.5 Environmental testing**

Due to the large size of the prototype detectors, and limitations of available environmental test chambers it was not possible to test complete systems over an extended temperature range. However it was possible to test coatings described in Chapter 4, using a Fisons temperature controlled chamber. Samples of the reflective Mylar sheet (200 mm x

50 mm), coated with a 100  $\mu\text{m}$  layer of the BN:ZnS:Kraton mixture, were subjected to temperatures from  $-20^{\circ}\text{C}$  to  $100^{\circ}\text{C}$ . Conclusions from these test were as follows:

- Below  $60^{\circ}\text{C}$  the coated layers appeared to remain unaffected by the heat; retaining shape and stiffness, and developing no loss of surface finish.
- Above  $80^{\circ}\text{C}$  the substrate was found to soften slightly, but the coating remained stable and intact.
- At  $100^{\circ}\text{C}$  (the operational limit of the chamber) the Mylar had noticeably softened further; bending to a  $45^{\circ}$  angle, under its own weight, when held horizontally, the integrity of the coating however remained good.
- On cooling down the samples were found to be physically unaffected by the test, returning to their original shape.

While further testing of completed equipment would be recommended, the above results suggest the coating techniques developed here are suitably robust to be employed in commercial systems.

## 7.6 Conclusion

It has been shown that an assembly employing a composite scintillating mixture of boron nitride and zinc sulphide, in conjunction with wavelength shifting light guides and photon counting electronics, can be used as a sensitive thermal neutron detector. This detector has been shown to be relatively insensitive to gamma radiation interference, and cost effective to manufacture in large sizes, and as such is eminently suitable for security portal applications. It has also been shown that these detectors can achieve sensitivity to fission neutrons at least comparable to, if not in excess of, similar sized  $^3\text{He}$  based detectors.

# Chapter 8

## Conclusions and recommendations

At present,  $^3\text{He}$  based proportional counters represent the only proven, commercially available, thermal neutron detectors, suitable for use in security portals, as well as numerous industrial applications, where high sensitivity and immunity to gamma radiation interference are essential requirements. However a finite limit to  $^3\text{He}$  supplies has led to dramatic increases in detector costs, and serious concerns about its long term availability. Furthermore due to increasing performance requirement, for security systems in particular,  $^3\text{He}$  based detectors are no longer cost effective or strategically reliable as the detector of choice in such systems.

The search for an alternative to  $^3\text{He}$  has led to the re-evaluation of technology developed by Barton et al [17] in 1991, for use in low background multiplicity experiments. Employing several thin layers of a  $^6\text{LiF:ZnS(Ag)}$  mixture, coupled to large wavelength shifting light guides, these detectors are only limited in size by the mechanical and optical constraints of the light guides. They are inherently insensitive to gamma radiation and are relatively simple to manufacture. However isotopically enriched lithium is by no means cheap or readily available. Therefore while this technology seemed eminently suitable for large scale security applications, it was proposed the technique might be modified for use with an alternative low cost capture compound.

Hexagonal boron nitride, manufactured for use in the cosmetics industry, was found to be an excellent substitute for  $^6\text{LiF}$  in the laminar scintillation detector. Providing a high thermal neutron cross section, even in its naturally occurring isotopic mix, its fine particle size and good mixing properties allow it to be combined with the scintillating powder to good effect, and with improvements made to light collection efficiency and pulse discrimination electronics it was possible to produce a neutron detector comparable in performance to the Barton detector and to similar sized  $^3\text{He}$  based devices.

However comparing performance of neutron detectors is not straight-forward, particularly when the incoming neutrons have a broad energy range, as is the case with fission neutrons emitted by a source at two meters or more. Aside from environmental

factors such as thermalization, neutron scattering and cosmic induced background, the shape and distribution of moderator within the detector has a major impact on efficiency. For gaseous proportional detectors, where the sensitive area is towards the centre of the moderator, it is impossible to design a detector with uniform sensitivity to the full potential incoming neutron energy range. However where the sensitive material is distributed throughout the moderator, as with the newly developed BN:ZnS system, it is possible to maintain sensitivity right through from thermal energies to neutrons of several MeV. While this undoubtedly increases sensitivity to moderated sources it also necessarily increases sensitivity to environmental background neutrons; as such the implications of using these detectors in security portals needs to be thoroughly assessed.

Independent, third party testing is essential to develop confidence in any new technology, particularly where devices are to be used in critical applications such as security systems. It is hoped that in the near future, the detectors developed here can be entered into a testing programme of this nature.

In laboratory and field testing the new detectors have been found to have intrinsic efficiency at least comparable to moderated  $^3\text{He}$  detectors (i.e. 10-15% for fission neutrons). Monte Carlo analysis predicted this is still well below the theoretical limit of performance for this technology. It is therefore believed that further optimization of; coating production, light collection, pulse discrimination etc. could lead to significant improvements in detector sensitivity.

Streamlining the manufacturing process is an important and difficult step in moving from a prototype to a commercial product. Developing cost effective techniques for production of uniform coatings, machined parts, and complex assemblies requires commercial and manufacturing expertise, which would ideally be provided by collaboration with an established organisation. It is hoped that such a partnership can be formed for the ultimate commercialization of this project.

Many applications require detectors of a specific size, shape and sensitivity; from toroidal thermal neutron detectors in industrial moisture gauges, to hand held security scanners. In theory the composite scintillating detector developed here is well suited to scaling both in terms of size and energy sensitivity as required by these application. It is therefore envisaged that projects will be undertaken to design and develop a range of detectors using this technology, for applications in the science, industrial and security sectors.

# References

1. J.H. Lazarus: *Guidelines for the use of radioiodine in the management of hyperthyroidism*: J R College Physicians London 1995.
2. R. Burghall: *Improved detection of radiation in scrap*. ECSC Final Report R583. June 2003.
3. IAEA: *Illicit Trafficking Database – ITDB Factsheet* Sep 2009.
4. Government Accountability Office (GAO): *U.S. and International Assistance Efforts to Control Sealed Radioactive Sources Need Strengthening*, GAO-03-638 August 2003.
5. R. Mustonen: *Potential Sources of Contamination in Inhabited Areas*. STUK – Radiation and Nuclear Safety Authority, Helsinki, August 2009.
6. A. Grotto: *Diffusing the threat of radiological weapons*. Centre for American Progress. July 2005
7. D. Hart: *UK nuclear medicine survey 2003-2004*. Nuclear Med Communication; 26: 937-94. 2005.
8. L.S. Zuckier: *Sensitivity of personal homeland security radiation detectors to medical radio nuclides . . .* RSNA 2004, Chicago , November 2004 .
9. D.A. Shea: *The advanced spectroscopic portal program; background . . .* Congressional research services. RL34750, Dec 2010.
10. D. Sanger: “*Nuclear detection effort halted . . .*” : New York Times, 29<sup>th</sup> July 2011.
11. J. Schweppe: *Homeland security Instrumentation for radiation detection at sea ports – PNNL SA 43032*, Nov 2007.
12. W. Gary: *A Primer on the Detection of Nuclear and Radiological Weapons*. Centre for Technology and National Security Policy National Defence University. May 2005.
13. G. Molnar: *Handbook of Prompt Gamma Activation Analysis: with Neutron Beams*- Springer ISBN-10:1402013043, Dec. 2004.
14. C. Lim: *On-line bulk elemental analysis in the resource industries using neutron - gamma techniques*. Journal of Radio Analytical and Nuclear Chemistry, 264 (No.1), 2005
15. S. Prussin: *Nuclear car wash status report - UCRL-TR-214636*: August 2005.
16. “*DOE begins rationing helium-3*” Physics Today, June 2010.
17. J. Barton: *A Novel Neutron Multiplicity Detector Employing ZnS : LiF - J Phys G:Nuc 17 p1885-1891*, Aug.1991.
18. A. Klett: *Plutonium Detection With A New Fission Neutron Survey Meter*- IEEE Transactions on nuclear science, Vol. 46, No. 4, Aug 1999.
19. G. Marshall: *Weight and counting efficiency optimization in a moderated neutron detection system - Nuc. Inst. & Meth. In Phys. (A 417) p332-341*, April 1998.
20. J. Ely: *Lithium Loaded Glass Fiber Neutron Detector Tests – PNNL report 18988*, November 12, 2009.

21. G. Knoll: *Radiation Detection and Measurement* (third edition), John Wiley & Sons. ISBN 0-471-07338-5 2000.
22. J. Birks: *The Theory and Practice of Scintillation Counters*, Macmillan 1964.
23. J. Turner: *Atoms, radiation, and radiation protection*- John Wiley & Sons, Inc. Academic Press,1995.
24. R. Runkle: *Securing special nuclear material. Advances in neutron detection.* . Journal of applied physics 108, 111101, Dec. 2010.
25. J. Briesmeister: *MCNP A General Monte Carlo N-Particle Transport Code Version 4B*: LA-12625-M, LANL 1997.
26. D. Gromushkin: *On thermal neutron concentration near ground level* – Proceedings 31<sup>st</sup> ICRC, Lodz 2009.
27. M. Florek: *Natural Neutron Fluence Rates* . . .Radiation Protection Dosimetry Vol. 67 1996.
28. M. Frank: *A Monte Carlo model of sea-level neutron background* . . . Journ. Radio. & Nuc. Chem. Vol. 249, 2001.
29. L. Forman: *Distinguishing spontaneous fission neutrons from cosmic ray background*. Brookhaven Labs – Presentation to SPIE 2004.
30. R. Kouzes: *Passive neutron detection for interdiction of nuclear materials at borders* – Nuc. Inst. & Meth. In Phys. 2008.
31. R. Kouzes: *The 3He Supply Problem* – PNNL-18388 – April 2009.
32. AEA: Technical / Functional specification for border radiation monitoring equipment – IAEA Tec. Doc. August 2004.
33. BS IEC 62244:2006 : *Radiation protection instrumentation – Installed radiation monitors at national borders*. July 2006.
34. US Department of Homeland Security: *Performance Specification for Advanced Spectroscopic Portal*. DNDO-PS-100220 - Oct 2005.
35. Crystran, Lithium Fluoride Product data sheet – [www.Crystran.co.uk/lithium-fluoride-lif.htm](http://www.Crystran.co.uk/lithium-fluoride-lif.htm), downloaded June 2011.
36. Applied scintillation Technologies - *Neutron Detection (ND) Screens* – Markets & Applications. [www.appscintech.com](http://www.appscintech.com), June 2011.
37. A. Stephen: *Modelling of composite neutron scintillators* – Radiation Protection Dosimetry, Vol. 116. 2005.
38. J. Brenizer: *Performance and Characteristics of scintillators for use in an electronic neutron imaging system* – Rev. Sci. Inst. Sep. 1997.
39. P. Koontz: *ZnS(Ag) phosphor mixtures for neutron scintillation counting*: University of California, Los Alamos Lab – W-7405-ENG.36, May 1954.
40. M. Matsubayashi: *Development of scintillator for a high-frame-rate neutron radiography*, Nuc. Inst. & Meth. In Phys. A 529, 2004.
41. W. Selove: *Fluorescent-wave-shifters and scintillators for calorimeters* - Nuc. Inst. & Meth. In Phys. Volume 161, Issue 2, May 1979.
42. M. Crow : *Shifting scintillator prototype large pixel fibre detector for the POWGEN3 powder diffractometer*: Nuc. Inst. & Meth. In Phys. 529, p287-292, 2004.
43. P. Klansen: *Application of wavelength shifter techniques to position measurement counter*: Nuc. Inst. & Meth. In Phys.185, 1981.

44. S. Henning: *An aerogel Cerenkov counter for AFS experiment*: IOP Science Phys. Scr. 23 703, 1981.
45. B. Leverington: *Light Guide Design for Phase 1 GlueX Sensor Module R & D Ver. 1.3* (GlueX-doc-651-v0), May 2006.
46. L. Wright: *Pulse shape discriminators for scintillators containing ZnS(Ag)*: UKAEA Harwell – HL65/3913, Aug 1965.
47. P. Davidson: *A new discrimination principle for slow neutron counting*: Rutherford Lab. RL-77-106/A, Oct 1977.
48. J. McMillan: *PhD Thesis* – University of Leeds, 1991.
49. N. Ensslin: *Passive Neutron Multiplicity Counting* : Los Alamos National Laboratory, LA-UR-07-142, 2007.
50. R. Martin: *Production, Distribution, and Applications of Californium-252 Neutron Sources*. Applied Radiation and Isotopes 53, 1999.
51. E. Holden: *report BNL-NCS-36379*. Brookhaven National Laboratory, 1985.
52. K. Van ripper: *Sabrina Manual* . Los Alamos National Lab. LA-UR-93-3696, 1993.
53. D Hutchinson: *Position sensitive neutron scintillation detectors*: Oak Ridge TN37831, 1999.
54. R.G. Williams: *Compendium of Material Composition Data for Radiation Transport Modeling* PNNL, April 2006.
55. C. Lundstebt: *Modeling solid state boron carbide low energy neutron detectors*. Nuc. Inst. & Meth. In Phys. A562, Jan 2006.
56. A. Lintereur: *Boron lined neutron detector testing* : PNNL report, Nov 2009.
57. J.S. Coursey: *Atomic Weights and Isotopic Compositions for All Elements*. National Institute of Standards and Technology. [www.nist.gov/pml/data/comp.cfm](http://www.nist.gov/pml/data/comp.cfm), Aug. 2009.
58. Scintillation Products; *Organic Scintillation Materials and Detectors* – 07/11 -Saint Gobain Crystals, [www.detectors.saint-gobain.com](http://www.detectors.saint-gobain.com). April 2009.
59. EJ-254 *Boron loaded plastic scintillator– data sheet* - Eljen Technology. April 2009.
60. E. Gatti: *Boron layer scintillation neutron detectors* – Laboratory CISE Milan, 1952.
61. R. Engels: *Boron Nitride, a neutron scintillator with deficiencies*. Nuclear Science Symposium IEEE, 2005.
62. J. Kirkbride : *Borazole and Boron Nitride Scintillators* : J chem. Phys 15, 1947.
63. BORONEIGE® # 301: *BORON NITRIDE POWDER* ,ESK Gmbh. [WWW.esk.com](http://WWW.esk.com) Jan. 2008.
64. D. Lelonis: *Boron Nitride Powder A Review*, Ceramic Technology International, 1994
65. H. Bethe, J. Ashkin: *Experimental Nuclear Physics*, New York, p253, 1953.
66. H. Bragg and R. Kleeman: *Philosophical Magazine* 10, p358, 1905.
67. H. Cember: *Introduction to Health Physics*, 3rd ed., McGraw-Hill, p132, 1996.
68. J.F. Ziegler, J. P. Biersack and M. D. Ziegler *SRIM: The Stopping and Range of Ions in Matter*. ISBN 0-9654207-1-X. 2008.
69. C. Bingham: *Alpha particles*, [www.AccessScience.com](http://www.AccessScience.com) McGraw-Hill, 2008
70. *Physical properties of common inorganic scintillators* – Saint Gobain Crystals ref. 42507. [www.detectors.saint-gobain.com](http://www.detectors.saint-gobain.com). April 2009.

71. Saint Gobain: *Brilliance Technical Brief*, [www.detectors.saint-gobain.com](http://www.detectors.saint-gobain.com). April 2009.
72. J. Barton: *Zinc sulphide scintillator with faster decay*. Journal of physics E: scientific instruments volume 10, 1977.
73. P. Lecoq: *Inorganic scintillators for detector systems*, Springer, 2006.
74. W.J. Yen M.J.Weber: *Inorganic Phosphors: Compositions, preparation and optical properties* CRC press, 2004.
75. A. Piotr: *Physical Processes in Inorganic Scintillators*, CRC-Press, July 1997.
76. J.S. Neil: *Comparative investigation of the performance of ZnO-based scintillators for use as  $\alpha$ -particle detectors*, Nuc. Inst. & Meth. In Phys. A. Vol. 568, issue 2, p803-809, Dec. 2006.
77. J. Charles Cooper: *Evaluation of ZnO(Ga) coatings as alpha particle transducers within a neutron generator*, Nuc. Inst. & Meth. In Phys. 2001.
78. Ca<sub>2</sub>F(Eu) - *Calcium Fluoride Scintillation material data sheet* – Saint Gobain Crystals. 3105 -01-05, 2001.
79. I. Holl: *Measurement of light yield in common inorganic scintillators* IEEE Transactions on Nuclear Science, Vol. 35, No. 1, February 1988.
80. B.Shul'gin: *Scintillation detectors with CaF<sub>2</sub>-Eu single crystals*, Translated from Atomnaya Energiya, Vol. 75, No. 1, p28-33, July 1993.
81. Kenichiro Yasuda: *Properties of a YAP powder scintillator as alpha-ray detector*. Applied Radiation and Isotopes 52, p365-368, 2000.
82. R. Swank: *Characteristics of Scintillators*, Annual review of nuclear science, Vol. 4: p111-140, Dec. 1954.
83. K. Bayarto: *The Quest for the Ideal Scintillator for Hybrid Phototubes*, IEEE Transaction on Nuclear Science, Vol.55, Issue 3, p1333-1337, June 2008.
84. Thorn EMI: *Photomultipliers and accessories- handbook*. Thorn EMI Electron tubes Ltd. 1993.
85. Phosphor Technologies Ltd: *product data sheets*. [www.phosphortechnologies.com](http://www.phosphortechnologies.com), downloaded March 2010.
86. Amcrys-h: *Organic Molecular Single Crystals : selection guide*. [www.Amcrys-h.com](http://www.Amcrys-h.com). March 2010.
87. SPI-Chem™ : *Y<sub>2</sub>SiO<sub>5</sub> P-47 datasheet*. [www.2spi.com/catalog/scintill/p47.shtml](http://www.2spi.com/catalog/scintill/p47.shtml). March 2010.
88. A.Quaranta: *Scintillation mechanism and efficiency of ternary scintillator thin films*, IEEE Transac. On Nuc. Sci. 49, 5, 2002
89. I. H. Campbell: *Efficient plastic scintillators utilizing phosphorescent dopants*, Applied Phys. Letters. 90, 012117, 2007
90. B.V. Grinyov: *Scintillation Material for Detection of  $\alpha$  -,  $p$ - Radiation Based on Polymer-Dispersed  $p$ -Terphenyl* IEEE Transac. On Nuc. Sci. 42 4, 1995.
91. H. Geissel: *Energy loss and straggling of alpha particles in thin homogeneous NE-111 scintillator foils*. Nuc. Inst. & Meth. In Phys.144, p456 1977.
92. K. Etting: *A thin film scintillator detector for light ions in low energy nuclear physics*. Nuc. Inst. & Meth. In Phys. 148, p299 1978.
93. M. Kirm: *Thin films of HfO<sub>2</sub> and ZrO<sub>2</sub> as potential scintillators*. Nuc. Inst. & Meth. In Phys. 537 p251 2005.
94. A. Quaranta: *Polymide based scintillating films*, IEEE Transac. On Nuc. Sci. 48, 2, 2001.

95. I.M. Hee-Jung: *Scintillators for alpha and neutron radiation synthesized by room temperature sol-gel processing*. Journal of Sol-Gel science and technology. Vol 32, No 1-3, p117-123, 2004.
96. G. Knoll: *Light Collection in scintillation detector composites*. Nuc. Science. IEE Transactions. Vol. 35. 1988.
97. J. Barton: *Decay characteristics of inorganic scintillators* : J.Phys. E:Sci. Inst. Vol.11, 1978.
98. Tyrrell : *Phosphors and scintillators in radiation imaging* : Nuc. Inst. & Meth. In Phys. 546 2005.
99. Dobrzynski, K. Blinowski: *Neutrons and Solid State Physics*: Ellis Horwood Limited. ISBN 0-13-617192-3, 1994.
100. J. Uher: *Efficiency of Composite BN Neutron detectors* : Applied Phys Letters 90, 2007.
101. M. Bourdinaud: *Low Cost Scintillators and wave length shifters* : Physica Scripta, Vol 23, 1981.
102. P. Klasen : *Application of wavelength shifting techniques to position measuring counters*: Nuc. Inst. & Meth. In Phys. Vol. 185, issues 1-3, p67-74, June 1981.
103. Saint Gobain Crystals: *BC-482 and BC-484 wavelength Shifting Bars* : data sheet [www.detectors.saint-gobain.com](http://www.detectors.saint-gobain.com). 2005.
104. Rohm Haas: *Plexiglas data sheet - GS2025*. [www.rohkhaas.com](http://www.rohkhaas.com), April 2009
105. Eljen Technology: *EJ-280 technical data sheet*. [www.eljentechnology.com](http://www.eljentechnology.com). Downloaded Jan 2009.
106. BWF Profiles: *Product catalogue*. BWF Kunststoffe GmbH & Co. KG – lagerkataloge – [www. Bwf-group.de](http://www.Bwf-group.de) 2010.
107. W. Viehmann: *Thin film wavelength shifter coatings for fluorescent radiation converters* : Nuc. Inst. & Meth. In Phys. 167, 1979.
108. W. Welford & R. Winston: *The optics of non-imaging concentrators*. Academic Press, 1978.
109. A. Lukasz: *Study of flexible liquid light guides*: Nuc. Inst. & Meth. In Phys. Vol. 337, Issues 2-3, p628-631, Jan.1994.
110. Kraton® : *111 – Polymer – data document* . [www.kraton.com/products](http://www.kraton.com/products), Jan. 2010.
111. H. Yang: *Large Scale Colloidal Self-Assembly by Doctor Blade Coating* - American Chemical Society, Langmuir, 26 pp13173–13182, July 22 2010.
112. Exxon Mobil HDPE HMA 014: *High density polyethylene resin – data sheet*. [www.exxonmobilchemical.ides.com](http://www.exxonmobilchemical.ides.com). 2009.
113. C. Heimbach: *Cosmic coincidences: Investigation of neutron background suppression*. Journal of research institute of standards, Vol.112 no 2, March 2007.
114. L. Forman: *Distinguishing spontaneous fission neutrons from cosmic-ray background*. SPIE 49<sup>th</sup> meeting, August 2004.
115. M. Frank: *A Monte Carlo model of sea level neutron background: Directionality, spectra, and Intensity*. Journal of radiochemical and nuclear chemistry, Vol. 249 p145-151, 2001.
116. J.H. Hubbell: *X-ray mass attenuation coefficients*. NIST physics reference data, NISTIR 5632 [www.nist.gov](http://www.nist.gov). 1996.
117. L. Wraight: *Pulse shape discrimination for scintillators containing ZnS(Ag)*: Harwell AERE-M833. August 1965.

118. A.G. Wright: *An investigation of photomultiplier background* : EMI Electron Tubes Reprint R/P075. 1979.
119. A.G. Wright: *Sources of noise in photomultipliers*. EMI Electron Tubes Reprint. R/P068. 1977.
120. P.B. Coates: *Photomultiplier noise statistics*. J.Phys.D: Appl. Phys. Vol. 5, 1972.
121. A.G. Gregory: *Cosmic ray induced photomultiplier noise*. Astronomical Society of Australia, Proceedings, vol. 3, Sept. 1976, p. 38, 39. 1976.
122. R. Clay: *Photomultiplier noise associated with cosmic rays*. J.Phys. A: Math. Gen. Vol. 10 1977.
123. E. Legler: *Pulse shape discrimination for  $^6\text{LiF}(\text{ZnS})$  scintillation counters*: Review of Scientific Instruments, Vol 36, Aug 1965.
124. A.G. Wright: *Design of photomultiplier circuits* . EMI Electron tubes Reprint R/P065. 1975.
125. Electron tubes: *Photomultiplier handbook*. Published- Electron Tubes Ltd. 20001.
126. Hamamatsu: *Photomultipliers – Basics and applications*. Third edition 2006.
127. Saint Gobain Crystals: *Bases, voltage dividers and preamplifiers*. 4001-4(11-03). 2003.
128. Electron Tubes: *Photomultiplier voltage dividers* – EMI Electron tubes R/P085, 1982.
129. J. Van der Spiegel: *PSPICE A brief primer*. University of Pennsylvania Department of Electrical and Systems Engineering 2006.
130. Cadence PSPICE A/D & PSPICE: *Advanced analysis – Tech brief*. 21202. Jan 2010
131. C. Garrard: *Practical photon counting* – Electron tubes R/P069. 1977.
132. D. Hicks: *Spontaneous-Fission Neutrons of Californium-252 and Curium-244*. Physical Review 98 (5).1955.
133. D. Hicks: *Multiplicity of Neutrons from the Spontaneous Fission of Californium-252*. Physical Review 97 (2): 1955.
134. G. Kaye, T. Laby: *Tables of physical and chemical constants – 14<sup>th</sup> edition*. ISBN: 0 582 46326 2. Longman 1973.
135. E. Gatti, F de Martini: *A new linear method of discrimination between elementary particles in scintillation counters*. Atomic Energy Coizj, Belgrade: Nuclear Electronics. 1961.
136. M. Karlsson: *Absolute efficiency calibration of an NE-213 liquid scintillator using a  $^{252}\text{Cf}$  source*. Dept. Nuclear Physics. Lund University Sweden 1997.
137. R. Seymour, M. Bliss: *A tubeless portable radiation search tool (PRST) for special nuclear materials*. IAEA int. conf. on security of materials. Stockholm 2001.
138. S. Fetter, R. Mozley: *Detecting nuclear warheads. Appendix A, Emission and absorption of radiation*. Science and global security. Vol. 1, 1990.
139. S. Fetter, V. Frolov: *Detecting nuclear warheads. Appendix B, Fissile materials and weapons design*. Science and global security. Vol. 1, 1990
140. S. Fetter, F. von Hippel: *The black see experiment – US and soviet reports from cooperative verification experiment*. Occasional report 1989.
141. Nuclear Threat Initiative: *A tutorial on nuclear weapons; design and materials*. www.NTI.org. 2006.
142. A. Peurrung, P. Reeder: *Location of neutron sources using moderator free directional neutron detectors*. IEEE transactions on nuclear science. Vol. 44. June 1997.

143. Article titled: *'Red Mercury' is Lithium-6, say Russian Weaponsmiths*. *Nucleonics Week*, p. 10, 22 July 1993.
144. C. Klinck:  *$\alpha$ -decay of  $^{241}\text{Am}$ . Theory - A lecture course on radioactivity*. University of Technology Kaiserslautern. <http://87.139.25.178:81/eng/theory.htm>. November 2010.
145. J. Keal: *Design principles of fluorescence radiation converters*. *Nuc. Inst. & Meth. In Phys.* 87, 1970.
146. M. Calvo: *Optical Waveguides From Theory to Applied Technologies*. CRC Press ISBN-10: 1574446983, Jan. 2007.

# Appendix A

## Neutron Sensitivity Calculations

The average distance of a vehicle from a detector -  $Avd$  in meters is calculated by integrating tangential speed over sampling period

$$\begin{aligned} \text{period} &:= 2 \text{ s} & \text{speed} &:= \frac{8}{3.6} & \text{distance} &:= 2.5 \text{ m} \\ \text{Intd} &:= \int_{-\left(\frac{\text{period}}{2}\right)+0.05}^{\left(\frac{\text{period}}{2}\right)+0.05} \sqrt{\text{distance}^2 + (\text{speed} \cdot t)^2} dt \\ \text{Ave}_i &:= \frac{\text{Intd}}{\text{period}} \\ \text{Ave} &= 2.8 \end{aligned}$$

The average distance of a vehicle from a detector whose height is distributed -  $Ave$  meters calculated by integrating  $Avd$  over a vertical displacement from  $a$  to  $b$ ;

$$\begin{aligned} a_0 &:= 0.5 & b_0 &:= 1.5 & i &:= 0..1 \\ a_1 &:= 2.5 & b_1 &:= 3.5 \\ \text{Ave}_i &:= \frac{\int_{a_i}^{b_i} \sqrt{\text{Ave}^2 + x^2} dx}{b_i - a_i} \\ \text{Ave} &= \begin{pmatrix} 2.986 \\ 4.108 \end{pmatrix} \end{aligned}$$

The proportion of a sphere radius  $Ave_i$  filled by detectors of effective neutron cross section  $500 \text{ cm}^2$ , can then be calculated.

$$\begin{aligned} \text{Res}_i &:= (100 \text{Ave}_i)^2 \cdot 4 \cdot \pi \\ \text{Res} &= \begin{pmatrix} 1.12 \times 10^6 \\ 2.121 \times 10^6 \end{pmatrix} \end{aligned}$$

$$\begin{aligned} \text{Sen}_{n_i} &:= \frac{500}{\text{Res}_i} \\ \text{Sen}_n &= \begin{pmatrix} 4.463 \times 10^{-4} \\ 2.357 \times 10^{-4} \end{pmatrix} \end{aligned}$$

For a source producing 20,000 counts at distance  $Ave_i$ , the count rate produced in the above detectors and the combined detectors, can be calculated.

$$\text{Cntn}_i := 20000 \text{period} \text{Sen}_{n_i}$$

The average distance of a vehicle  $Avd$  in meters from a detector set back by  $distance$  m, at a velocity of  $x$  kmh over  $period$  seconds. The period is offset by 0.05s for worst case.

$$Cntn = \begin{pmatrix} 17.853 \\ 9.429 \end{pmatrix}$$

$$SumA := Cntn_0 + Cntn_1$$

$$SumA = 27.282$$

Incorporating a typical background count rate of 1.0 neutrons/s

$$nbg := 1.0 \cdot period$$

$$nfg1 := Cntn_0 + nbg$$

$$nfg2 := Cntn_1 + nbg$$

$$nfgs := (Cntn_0 + Cntn_1) + 2nbg$$

$$nbg = 2 \quad nfg1 = 19.853$$

$$nfg2 = 11.429 \quad nfgs = 31.282$$

Using the average count rates calculated above, the associated poisson distributions can be produced for the following situations:  $a_k$  – single detector background,  $b_k$  – double detector background,  $c_k$  – single detector foreground,  $d_k$  – double detector foreground,

$$a_k := qpois(target_k, nbg)$$

$$b_k := qpois(target_k, nbg \cdot 2)$$

$$c_k := qpois(target_k, nfg1)$$

$$d_k := qpois(target_k, nfgs)$$

$a_k =$	$b_k =$	$c_k =$	$d_k =$	
0	0	6	13	99.9%
0	0	8	16	
0	0	10	19	99%
0	2	14	24	
2	4	20	31	
4	7	26	39	Mean
6	9	31	45	
8	11	35	50	
9	13	38	54	0.1%
10	15	42	58	0.01%
12	17	44	61	0.00%

## **Statistical Neutron Sensitivity**

From the above figures it can be seen that based on statistical analysis the threshold needed to achieve 0.1% false positive is 8 counts, based on a 2 count average background level, or 11 counts for a 4 count average background. For two detectors this level gives a false negative rate of better than 99.9%. However in a dynamic system, to achieve a 0.1% false alarms per vehicle it is necessary for the probability per test to be up to 10 times less than this ( 0.01%) to cover the multiple test carried out as a vehicle passes through the system.

Over the 2 sec period the counts produced by a 4 uCi  $^{252}\text{Cf}$  source passing the detectors was calculated as an average of 20 counts for 1 detector and 31 counts for two detectors combined (assuming no shielding). Both of these options comfortably exceed the required sensitivity to achieve 99% probability of false negative alarms.

These calculations only take into account fast neutrons, i.e. those experiencing little scattering. In operation it has been observed that actual count rates from a fast neutron source are higher than predicted here due to neutron scattering particularly in the ground.

## Appendix B

### MCNPX input file for Tata Redeem <sup>3</sup>He based detector

Redeem 2x He3 Detector in moderator natural environment

```

1 2 -5.354E-4 3 -4 -30 IMP:n=1 $ He3 detector
2 2 -5.354E-4 3 -4 -32 IMP:n=1 $ He3 detector
10 3 -7.874 (2 -5 30 -31) #1 IMP:n=1 $ detector can
11 3 -7.874 (2 -5 32 -33) #2 IMP:n=1 $ detector can
20 1 -1.0 1 -6 7 -8 20 -21 -22 -23 24 25 IMP:n=1 $ Moderator
21 3 -7.874 41 -51 52 -53 55 -58 IMP:n=1 $ stanchion back
22 3 -7.874 41 -51 53 -54 55 -56 IMP:n=1 $ stanchion side
23 3 -7.874 41 -51 53 -54 57 -58 IMP:n=1 $ stanchion side
30 4 -2.3 40 -41 42 -43 44 -45 IMP:n=1 $ Ground
40 3 -7.874 90 -91 IMP:n=1 $ source holder
50 10 -1.205E-3 -1000 #1 #2 #10 #11 #20 #21
    #22 #23 #30 #40 IMP:n=1 $ Air
100 0 1000 IMP:n=0 $ Nothing

1 py 0 $ Base of moderator
2 py 5 $ Base of detector
3 py 5.05 $ Base of gass
4 py 104.95 $ Top of gass
5 py 105 $ Top of detector
6 py 110 $ Top of moderator
7 px 0 $ Front of moderator
8 px 12 $ back of moderator
20 pz -12 $ left side of moderator
21 pz 12 $ Right side of moderator
22 p 1 0 -1 21.5 $ moderator champher
23 p 1 0 1 21.5 $ moderator champher
24 c/y 7 -3.2 3 $ moderator cut out
25 c/y 7 3.2 3 $ moderator cut out
30 c/y 7 -3.2 2.48 $ Detector1 gass
31 c/y 7 -3.2 2.5 $ Detector1 tube
32 c/y 7 3.2 2.48 $ Detector2 gass
33 c/y 7 3.2 2.5 $ Detector2 tube
40 py -200 $ Ground
41 py -100 $ Ground
42 px -200 $ Ground
43 px 300 $ Ground
44 pz -200 $ Ground
45 pz 200 $ Ground
51 py 400 $ top of stanchion
52 px -7 $ back of stanchion
53 px -5 $ front of stanchion
54 px 15 $ web of stanchion
55 pz -17 $ side of stanchion
56 pz -15 $ side of stanchion
57 pz 45 $ side of stanchion
58 pz 47 $ side of stanchion
90 s 230 50 0 1 $ source holder
91 s 230 50 0 1.2 $ source holder
1000 so 1000 $ Rest of Unvers

m1 6000.60c 0.3333 1001.60c 0.6666 $ Polyethylene
mt1 poly.01t $ Poly thermal

```

```

m2 2003.60c 1 $ He3
m3 14000.60c 0.01 24000.50c 0.19 25055.60c 0.02 $ Stainless Steel
    26000.55c 0.68 28000.50c 0.10
m4 1001.60c 0.31 8016.60c 0.50 13027 0.01 11023.60c 0.01 $ Concrete
    14000.60c 0.15 20000.60c 0.02
m10 006000.60c -0.0001266242 $ Air; rho = 0.00120484 g/cc
    7014.60c -0.762280494675 7015.60c -0.0028001953254
    008016.60c -0.23470328576 008017.60c -0.000089400020638
mode n $ neutron only mode
c isotropic point source emitting fission neutrons
  sdef pos=230 50 0 par=1 erg=d1 $ monodirectionally +ve x direction
  sp1 -3 1.025 2.926 $ watt fission for Cf-252
spontaneous
c
F4:N 1
nps 2000000 $ 10000 particles
print 10 30 40 50 100 126 130 140 160 161 162
ptrac write=all file=asc $ particle track

```



```

25 px 17 $ LIF 8
1000 so 500 $ Rest of Univers

m1 8000.60c 0.3333 1001.60c 0.6666 $ Polyethylene 0.94 g/cc
mt1 poly.01t
m2 001001.60c -0.0805259 001002.60c -0.0000120807 $ perspex 1.19 g/cc
008016.60c -0.319492 008017.60c -0.000121453
006000.60c -0.599848
mt2 poly.01t
m3 3006.60c -0.229 3007.60c -0.012 9019.60c -0.758 $ Li-6F 2.54 g/cc
m10 006000.60c -0.0001266242 $ Air 1.205E-3 g/cc
7014.60c -0.762280494675 7015.60c -0.0028001953254
008016.60c -0.23470328576 008017.60c -0.000089400020638
mode n $ neutron only mode
c plane source size of detector uniformly emitting fission neutrons 1000 cm^2
sdef pos=0 0 0 x=0 y=d1 z=d2 par=1 erg=d3 vec=1 0 0 dir=1 $ monodirectionally in
the +ve x direction
si1 0 100 $ sampling range xmin to xmax
sp1 0 1 $ weighting for x sampling: here constant
si2 0 50 $ sampling range zmin to zmax
sp2 0 1 $ weighting for y sampling: here constant
sp3 -3 1.025 2.926 $ watt fission with parameters for Cf-252
spontaneous
c
F4:N 1
nps 100000 $ 10000 particles
print 10 30 40 50 100 126 130 140 160 161 162
c ptrac write=all file=asc $ particle track

```

# Appendix D: Prototype pulse discrimination circuit diagram

